Single-Site, Noninvasive, Blood Pressure Measurements at the Ear using Ballistocardiogram (BCG), and Photoplethysmogram (PPG), and a Low-Power, Reflectance-Mode PPG SoC

by

Eric S. Winokur

M.S. (ECE), Lehigh University (2008)
B.S. (ECE), Lehigh University (2006)

Submitted to the
Department of Electrical Engineering and Computer Science
in partial fulfillment of the requirements for the degree of

Doctor of Philosophy

at the

MASSACHUSETTS INSTITUTE OF TECHNOLOGY

June 2014

Author .....
Department of Electrical Engineering and Computer Science
April 7, 2014

Certified by .....
Charles G. Sodini
Lebel Professor of Electrical Engineering
Department of Electrical Engineering and Computer Science
Thesis Supervisor

Accepted by .....
Professor Leslie A. Kolodziejski
Chairman, Committee on Graduate Students
Department of Electrical Engineering and Computer Science

Single-Site, Noninvasive, Blood Pressure Measurements at the Ear using Ballistocardiogram (BCG), and Photoplethysmogram (PPG), and a Low-Power, Reflectance-Mode PPG SoC

by

Eric S. Winokur

Submitted to the Department of Electrical Engineering and Computer Science
on April 7, 2014, in partial fulfillment of the
requirements for the degree of
Doctor of Philosophy

Abstract

This work presents a wearable congestive heart failure (CHF) monitor at the ear that uses the ballistocardiogram (BCG), electrocardiogram (ECG), and photoplethysmogram (PPG) to extract mean blood pressure up the Carotid Artery.

Being a natural anchoring point, the ear is demonstrated as a viable location for the integrated sensing of physiological signals. The BCG is obtained with an accelerometer, the ECG is taken in a single lead configuration, with one electrode at the mastoid and one on the back of the neck, and the PPG is measured by reflecting light off of the mastoid region above Reid's baseline. When the BCG and PPG are used together, a time delay of the blood pulse wave can be obtained, known as the pulse transit time (PTT), from a single site of measurement.

The ear-worn device is wirelessly connected to a computer for real-time data recording. A clinical test involving hemodynamic maneuvers is performed on 15 subjects. The results demonstrate a linear relationship between mean blood pressure and $ln(\frac{1}{PTT})$. Using amplitude information from the BCG signal allows for improving the accuracy of the PTT-to-BP algorithm without additional sensors.

While the clinical device uses commercial components, a custom integrated circuit for reflectance-mode PPG is designed with the goal of removing static and time-varying interferers while minimizing power consumption and device size. The chip nominally consumes $425\mu W$ and only requires LEDs and photodiodes to operate, replacing 7 chips and a MATLAB program compared to the discrete version. The circuit architecture leverages analog and digital techniques to remove up to $100\mu A$ of static interferers and attenuate time-varying interferers by $87dB$.

Thesis Supervisor: Charles G. Sodini

Title: Lebel Professor of Electrical Engineering

Department of Electrical Engineering and Computer Science

To my mother and brother, and in memory of my father

Acknowledgments

My time at MIT would not have been enjoyable without the fantastic people I was surrounded by everyday. First and foremost, I would like to sincerely thank my advisor, Professor Charlie Sodini. His knack for knowing when and how to push graduate students to achieve their best work is uncanny. Whether we were hanging out at Red Sox games, in Hong Kong, at Christmas parties, or in lab meetings, things were always interesting. Words cannot say how lucky I was to have him as an advisor.

Next, I would like to thank the students with whom I worked with. David He was my partner in crime for much of my tenure here, and I enjoyed working closely with him. I would also like to thank Marcus Yip for designing the ADC of my chip. Marcus, Daniel Kumar, Bruno Do Valle and Michael Georgas were also extremely helpful answering questions during my tapeout. I would also like to thank the other Sodini / Lee students for their friendship, guidance, and political conversations (Grant).

Professor Thomas Heldt has been a trove of physiological information, and has always been available to answer questions, no matter his travel schedule. Tom O'Dwyer and Michael Coln from Analog Devices generously offered their time and technical advice to help with my chip design and packaging.

The clinical tests would not be possible without nurse Catherine Ricciardi, who made sure that all of our tests were done thoroughly and properly. Her charm and wit made the long hours in the clinic pass by significantly faster. I would also like to thank the brave souls who volunteered for the clinical tests. Without their time and hemodynamic responses, this thesis would not be complete.

I would also like to thank Professor Harry Lee and Professor Collin Stultz for serving as committee members for my thesis. Their guidance has been instrumental to the project's direction.

Over the past 4.5 years, I was very lucky to live with kind, thoughtful and respectful roommates. Matt, Kyle, Drew, Ben, and Emilio all helped to keep me sane and pry me away from my work when I needed it the most. Thank you so much for living with my eccentricities.

Finally, I would like to thank my parents and brother for raising me in a household where I was told to follow my dreams, and that anything was possible. Even though my father is no longer with us, I know that he would be proud of my accomplishments. My brother, whom I have looked up to (literally and figuratively) throughout my entire life, has taught me many lessons. From throwing a baseball, to driving a stick-shift, he has always been there. Thank you all so much.

This project's funding is made possible by the MIT Medical Electronic Device Realization Center (MEDRC) and the MIT Center for Integrated Circuits and Systems (CICS). Chip fabrication was kindly donated through TSMC's University Shuttle Program.

Contents

List of Figures

List of Tables

Abbreviations and Acronyms

ADC	Analog-to-digital converter
AgCl	Silver chloride
aVF	Augmented vector foot
aVL	Augmented vector left
aVR	Augmented vector right
BCG	Ballistocardiogram
BP	Blood pressure
BW	Bandwidth
CBFV	Cerebral blood flow velocity
CDS	Correlated double sampling
CHF	Congestive heart failure
CO	Cardiac output
COPD	Chronic obstructive pulmonary disease
CRC	Clinical Research Center
CS	Chip select
DAC	Digital-to-analog converter
DC	Direct current
DRE	Dynamic range enhancement
ECG	Electrocardiogram
EMD	Electromechanical delay
ENOB	Effective number of bits

FDA	Food and Drug Administration
FET	Field effect transistor
FFT	Fast Fourier transform
FIR	Finite impulse response
Hb	Hemoglobin
HbO_2	Oxy-hemoglobin
HR	Heart rate
IA	Instrumentation amplifier
IC	Integrated circuit
ICG	Impedance cardiography
IR	Infrared
LA	Left arm
LDO	Low dropout
LED	Light emitting diode
LL	Left leg
LSB	Least significant bit
LVET	Left ventricular ejection time
MAP	Mean arterial pressure
MCU	Microcontroller unit
MEMS	Micro-electo-mechanical system
MIT	Massachusetts Institute of Technology
mmHg	Millimeters of mercury
MSB	Most significant bit
NFET	N-type field effect transistor
NMOS	N-type metal oxide semiconductor
OCF	Optical coupling factor
OOK	On-off keying
Op-Amp	Operational amplifier
PAT	Pulse arrival time
PCB	Printed circuit board

PD	Photodiode
PEP	Pre-ejection period
PID	Proportional-integral-derivative
PMOS	P-type metal oxide semiconductor
PPG	Photoplethysmogram
PTT	Pulse transit time
PWV	Pulse wave velocity
R/W	Read / write
RA	Right arm
RJI	R-to-J interval
RMS	Root mean squared
RoR	Ratio of ratios
SaO_2	Arterial oxygen saturation
SNDR	Signal-to-noise plus distortion ratio
SNR	Signal-to-noise ratio
SoC	System on chip
SpO_2	Peripheral oxygen saturation
SV	Stroke volume
TIA	Transimpedance amplifier
TPR	Total peripheral resistance
UART	Universal asynchronous receiver / transmitter
USB	Universal serial bus

Chapter 1

Introduction

1.1 Congestive Heart Failure Monitoring

Congestive heart failure (CHF) occurs when the heart is unable to pump enough blood to meet the metabolic oxygen demand of the body [1]. Symptoms include shortness of breath (dyspnea), buildup of excess fluid in the body (edema), fatigue, and increased heart rate, among others [2]. Currently, an estimated 5.1 million Americans $\geq$ 20 years of age have heart failure, and by 2030, that number is expected to rise to $>$ 8 million [3]. This work, combined with the work done by my lab partner David He [4], focuses on the continuous and wearable measurement of blood pressure (BP), heart rate (HR), stroke volume (SV) and pre-ejection period (PEP), all of which are useful indicators for heart failure disease management.

High blood pressure (hypertension) causes the heart to work harder as a pump, which is why 75% of all CHF cases have antecedent hypertension [3]. Patients diagnosed with CHF often monitor their blood pressure at home to ensure they are not unduly increasing the work load on their heart. Hypertension can exacerbate symptoms from CHF, leading to hospitalization until their condition has re-stabilized. Medications such as diuretics, beta-blockers, and vasodilators, as well as a low sodium diet are used to maintain low blood pressure in CHF patients [5].

The PEP, which is the electromechanical delay of the heart, is also affected by CHF. When the heart muscle weakens, it takes longer to generate the internal force

necessary to push blood into the aorta, thus, the PEP elongates [6]. This extra time delay also affects SV, which requires strong heart muscle to push out a lot of blood per beat. To compensate for a decrease in SV, the heart rate increases to maintain a constant flow of blood to the body. To improve the PEP and SV, doctors may prescribe a digitalis to increase the heart muscle strength, also known as contractility [7].

Monitoring hemodynamic parameters such as BP, SV, HR, and PEP can help physicians intervene before a CHF patient requires hospitalization [8] [9]. Therefore, a non-invasive, and wearable prototype for proof-of-concept CHF monitoring is proposed in this thesis.

1.2 CHF Monitoring on the Body

This work presents a wearable CHF monitor at the ear (Figure 1-1). The ear has been chosen for both mechanical and physiological reasons. Mechanically, the mastoid region behind the ear is rigid, which reduces motion artifacts compared to other areas such as the finger or wrist. The ear location is also discreet as a small device can be hidden by the ear or hair. The ear is also a natural anchor that has been exploited for many years, as is evidenced by hearing aids and BlueTooth headsets [10].

Physiologically, several measurements can be obtained from the site around the ear. These include a mechanical signal (the ballistocardiogram, BCG), an electrical signal (the electrocardiogram, ECG), and an optical signal (the photoplethysmogram, PPG). These signals allow the measurement of mean blood pressure, heart rate, stroke volume, pre-ejection period and blood oxygenation.

Although the work presented in this thesis is from the ear, other sites may be even better suited for CHF monitoring. For example, the blood pressure measurement obtained from the ear is a measurement up the carotid artery, which is different than the pressure taken by a physician at the arm. Other possible sites for discreet, continuous CHF monitoring could be a strap around the upper arm, or sensors embedded into

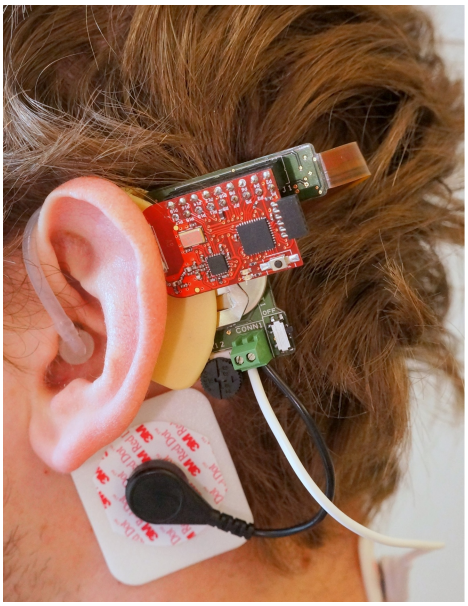

Figure 1-1: The site behind the ear proposed as a wearable CHF monitor

the elastic band of underwear. All three sites, including the ear are usually in the same vertical orientation relative to heart level, which reduces the need for continuous hydrostatic calibrations for cuffless blood pressure calculations [11]

1.3 Aims of Thesis Work

The research presented in this thesis has the following five aims:

- To achieve PPG measurements at the head with an ear-worn device in a clinical setting.
- To investigate the relationship between pulse transit time (PTT) and blood pressure up the carotid artery using the head PPG and head BCG from a single site of measurement.
- To explore the use of heart rate and stroke volume measurements from the wearable device to improve the accuracy of the PTT to BP algorithm.
- To create an algorithm which can remove time-varying and static interferers from a PPG signal chain in a low power manner.

- To create a PPG system on chip (SoC) which includes algorithms for time-varying and static interferer removal while optimizing power consumption and minimizing the total area required for a PPG front end.

1.4 Thesis Organization

This thesis is organized into the following chapters:

- Chapter 2 introduces the physiologic origins of the BCG, ECG, and PPG. Measurement modalities ranging from historical apparatus to modern methods are examined. Basic visual comparisons of the head BCG, ECG and PPG are shown compared to traditional waveforms. A theoretical derivation of how two PPGs can be used to calculate blood oxygenation is explained. Finally, three different timing intervals, the RJ interval, PTT, and pulse arrival time (PAT), and their clinical relevance are introduced.

- Chapter 3 describes the classification of blood pressure values and several methods to obtain blood pressure non-invasively. The relationship between PTT and blood pressure is derived using fluid dynamics. Accuracy improvements for this relationship using signals available from the wearable CHF monitor are also discussed.

- Chapter 4 describes the clinical prototype of the wearable CHF monitor that measures the BCG, ECG and PPG. The device's hardware, firmware and software are discussed. A clinical test is conducted at MIT using the wearable heart monitor and reference measurement equipment. The data allows the characterization of the head PPG morphology across different subjects. Using the data, the devices measurements of PTT up the carotid artery are evaluated. Algorithm improvements using BCG at the ear and PPG at the finger are also explored.

- Chapter 5 presents a static interferer removal architecture for the PPG SoC. This architecture allows for an increase in dynamic range while maintaining a

low-voltage and high gain of the front end. A time-varying interferer removal algorithm is also derived. Fundamental and harmonic frequencies from office lighting are shown to be rejected. Both architectures are compared to previous works.

- Chapter 6 presents a low-power PPG SoC with static and time-varying interferer removal. The goal of the PPG SoC is to directly replace the discrete PPG circuit components in the wearable CHF monitor while consuming significantly less power and area. This goal is realized with a novel system architecture which leverages both analog and digital techniques. The low power circuit design of each circuit block, the electrical characterization, and PPG measurement results are discussed.

- Finally, Chapter 7 concludes the work with a summary of contributions and items for future work.

Chapter 2

Physiological Signals at the Ear

This chapter begins with describing the three physiological signals measured by the wearable CHF monitor. The first signal is mechanical and called the ballistocardiogram (BCG). The second is an electrical signal called the electrocardiogram (ECG) and the third is an optical signal called the photoplethysmogram (PPG). Each signal is described in detail, and traditional measurement methods are compared to those used by the wearable CHF monitor. Three timing intervals, the RJ interval (RJI), pulse transit time (PTT), and pulse arrival time (PAT), which are obtained through combining information from the BCG, ECG, and PPG are also introduced. Finally, their clinical relevance is explained.

2.1 The Head Ballistocardiogram (BCG)

2.1.1 Traditional BCG

The ballistocardiogram (BCG) is a mechanical signal manifested by the acceleration of blood around the vasculature [12]. The phenomena is an application of Newton's second and third laws. Newton's second law: $F = ma$, where F is the force exerted on the body by the blood, m is the mass of blood, and a is the acceleration of the blood inside the arterial tree, and Newton's third law: as the blood accelerates in different directions, this will cause an equal and opposite reactionary force by the

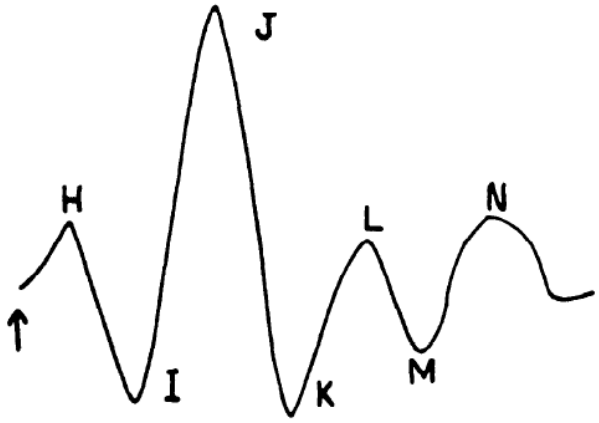

Figure 2-1: The traditional BCG waveform as annotated by Starr [12]. The principal peak, labelled as the J-wave, has been shown to correlate to stroke volume, and has strong time correlations to the pre-ejection period of the heart [4].

body, which can be measured.

The traditional BCG consists of several peaks and valleys, labelled as the H through N waves, as shown in figure 2-1. I-J acceleration is usually on the order of 10mG and occurs in about 50ms, which means that the body is only displaced about 250μm.

$$D = (J_{amp} - I_{amp}) \cdot 9.8(\frac{m}{s^2}) \cdot (J_{time} - I_{time})^2(s)^2 = Displacement \qquad (2.1)$$

Traditionally, the BCG was observed by having subjects lie down on a low-friction bed. The periodic movements by the BCG would cause displacement of the bed, which could then be recorded. The clinical significance of the BCG was first discussed by Starr in 1939, and then expounded further by several groups through the 1950's [12] [13]. It was noted that the amplitude of the J-wave of the BCG corresponded to the stroke volume of the subject, which is the amount of blood expelled by the heart per beat. Prolongation, or delay of the J-wave compared to the R-wave of the ECG was also observed in subjects with myocardial disease and heart failure.

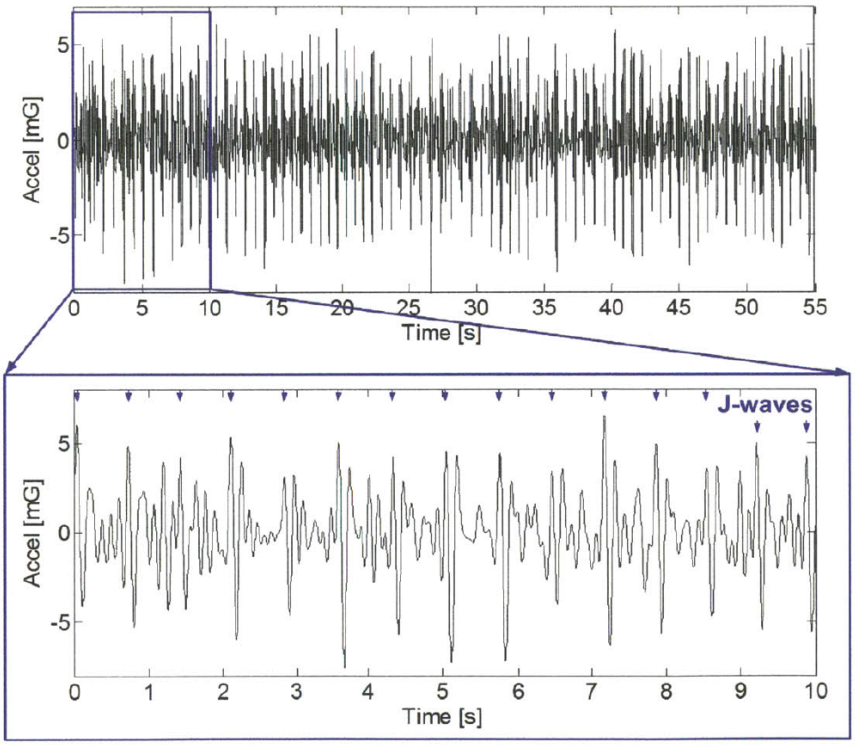

Figure 2-2: The head BCG measured by a y-axis (headward-footward) accelerometer in the standing posture. The J-waves are annotated. (figure from [4]).

2.1.2 Head BCG

The BCG can be observed at the head, and measured through multiple methods, as shown by He [4]. During clinical testing of the CHF monitor, the head BCG was measured through the use of a MEMS tri-axial accelerometer (Bosch BMA180). Figure 2-2 shows the BCG measured at the head with the accelerometer. The J-waves are clearly evident as the principal peak of the BCG, however the waveform is too noisy to discern many of the other traditional waves. To further analyze the BCG, ensemble averaging can be used to show the H, I, K and L waves, as shown in figure 2-3. This is done by time aligning each J-wave and then averaging the beats [4]. As mentioned previously, the head BCG has peak-to-peak acceleration on the order of 10 mG, which places noise requirements on the accelerometer to be less than 1mG RMS.

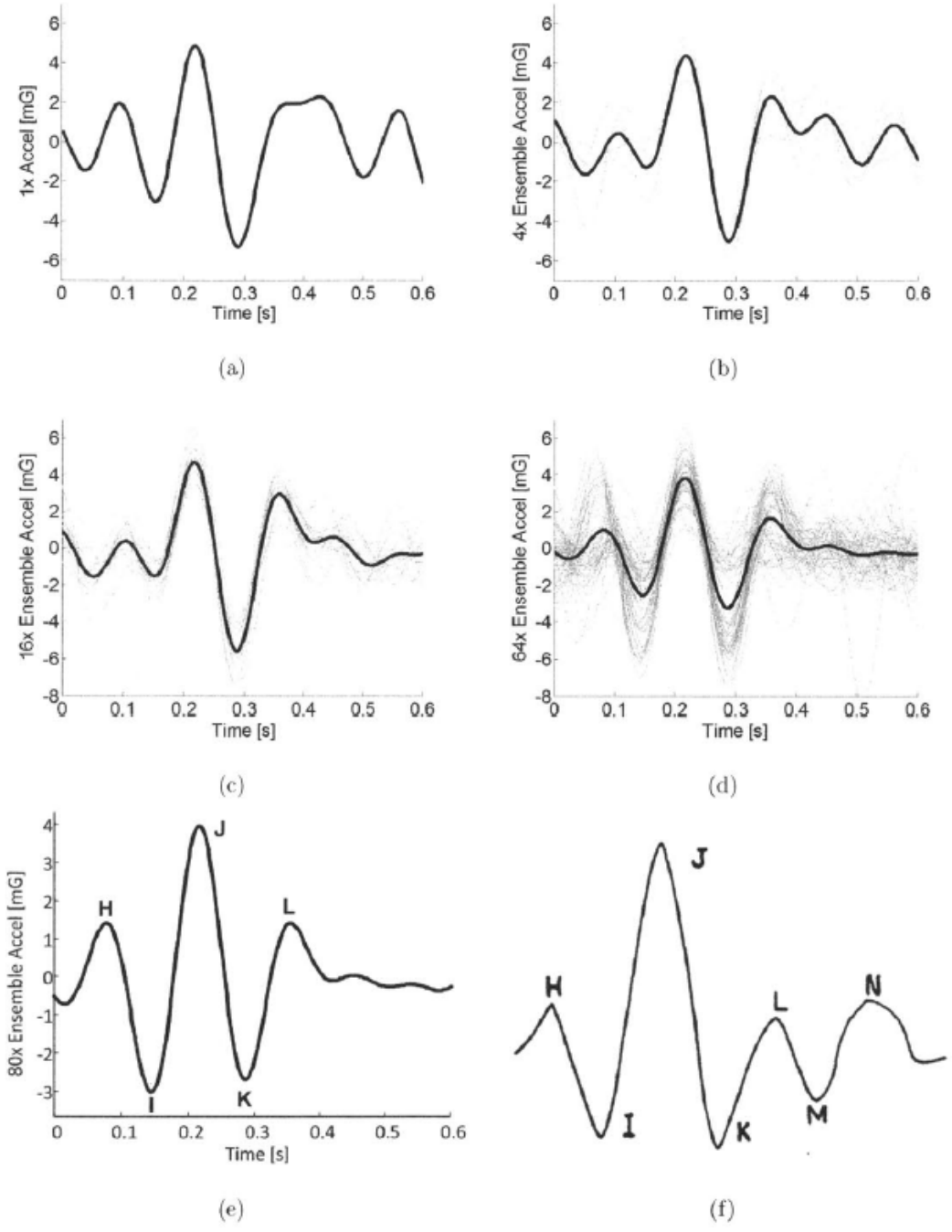

Figure 2-3: a) The head BCG from the first beat, and the ensemble head BCG's from b) the first 4 beats, c) the first 16 beats, d) the first 64 beats, e) the first 80 beats, and f) the traditional BCG [12]. The subjects average beat-to-beat interval is 0.73s (figure from [4]).

2.2 The Electrocardiogram (ECG)

2.2.1 Traditional ECG

The electrocardiogram (ECG) is a non-invasive measurement of the surface electrical activity of the heart. Traditionally, the ECG is measured with 2 - 10 electrodes placed on the chest. Measuring the potential difference between 2 electrodes, or 2 sets of electrodes, can show electrical activity in different regions of the heart. If a patient has an abnormal heart rhythm, the ECG is often one of the first tests utilized to try and assess the type of abnormality, and where it is located. Figure 2-4 shows the anatomy of the heart.

Modern ECG signals are measured using gel electrodes made with silver chloride (AgCl) for its low half-cell potential. The signals are typically around 1mV in amplitude with a clinical bandwidth of 0.5 - 150 Hz [15]. A drawing of a normal ECG is shown in Figure 2-5 with the P, Q, R, S, and T waves annotated. The P waves correspond to atrial depolarization, while the Q, R and S waves corresponds to ventricular depolarization. The T wave represents ventricular repolarization [16].

An ECG vector between two electrodes, or two sets of electrodes, is called an ECG lead. There are several standard ECG leads which give insight as to what different parts of the heart are doing, as shown in Figure 2-6. Standard electrode placement for a twelve lead ECG includes one on both the right and left shoulders, as well as an electrode on the left and right sides of the stomach below the umbilicus. Six electrodes (V1, V2, V3, V4, V5, and V6) are placed across the chest, with V1 and V2 in the fourth intercostal spaces, V4, V5 and V6 in a horizontal line, and V3 between V2 and V4, as shown in Figure 2-7 [17]. Leads I, II, and III are vectors from 2 electrodes, either right arm (RA) to left arm (LA), RA to left leg (LL) or LA to LL, while augmented vector right (aVR), augmented vector left (aVL) and augmented vector foot (aVF) are combinations of these three electrodes. The precordial leads (V1 - V6) are vectors from the Vx electrode to a summed combination of RA, LA and LL.

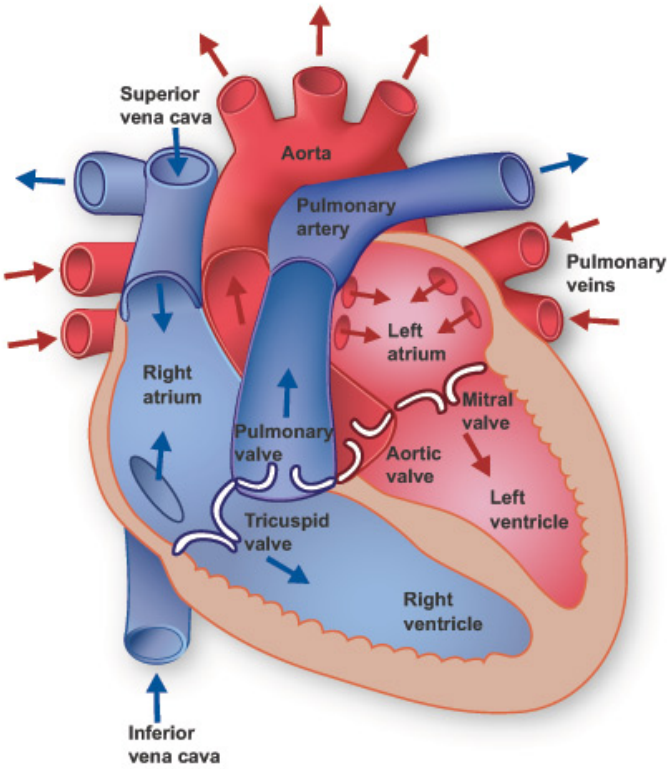

Figure 2-4: The anatomy of the heart (figure from [14]).

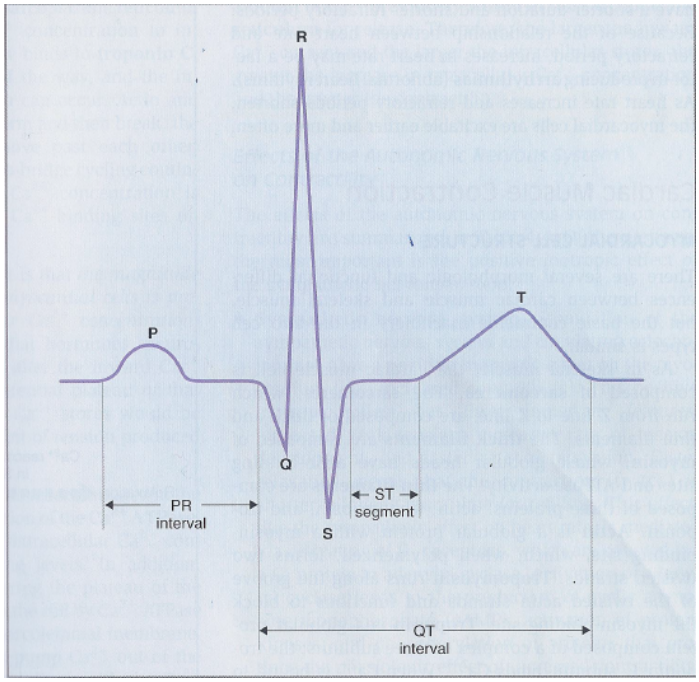

Figure 2-5: A simple example of a normal ECG with the P, Q, R, S, and T waves annotated (figure from [16]).

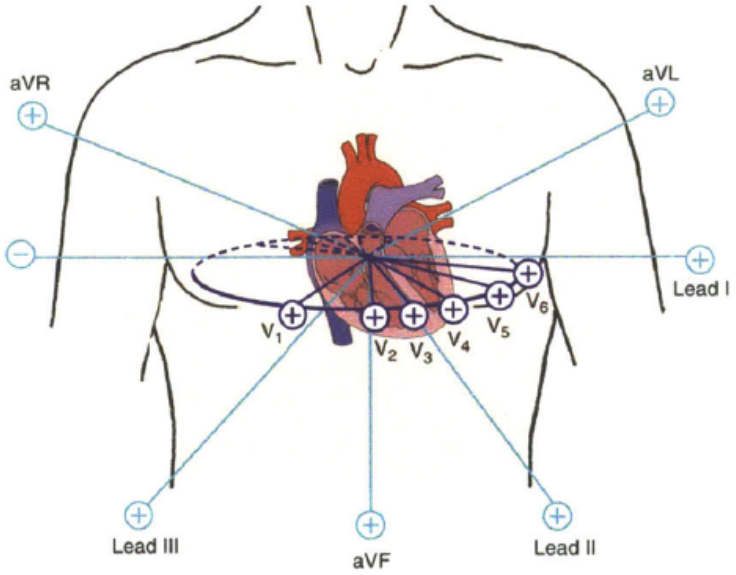

Figure 2-6: The Standard 12-lead ECG (figure from [18])

It is often useful to monitor a patient's ECG over several days to diagnose a heart arrhythmia. These monitoring devices are known as Holter monitors [19]. Holter monitors will measure one or more ECG leads and store the data in memory for off-line analysis. Many Holter monitors have wires going from the chest to a base station worn on or near the belt, while some newer form factors remove long wires and keep the base station at the chest or wirelessly transmit the ECG, as shown in Figure 2-8 [20] [21] [22]. All of these monitors use electrodes at the chest to obtain the highest ECG signal quality.

2.2.2 Head ECG

The wearable CHF monitor measures a single lead ECG from the head. This is to avoid long wires connected from the ear to the chest. The ECG is measurable at the head because the body is a conductive medium, therefore, the ECG can be obtained throughout the body in attenuated form. The CHF monitor utilizes one electrode at the mastoid region behind the left ear, and a second electrode on the back of the neck (Figure 1-1).

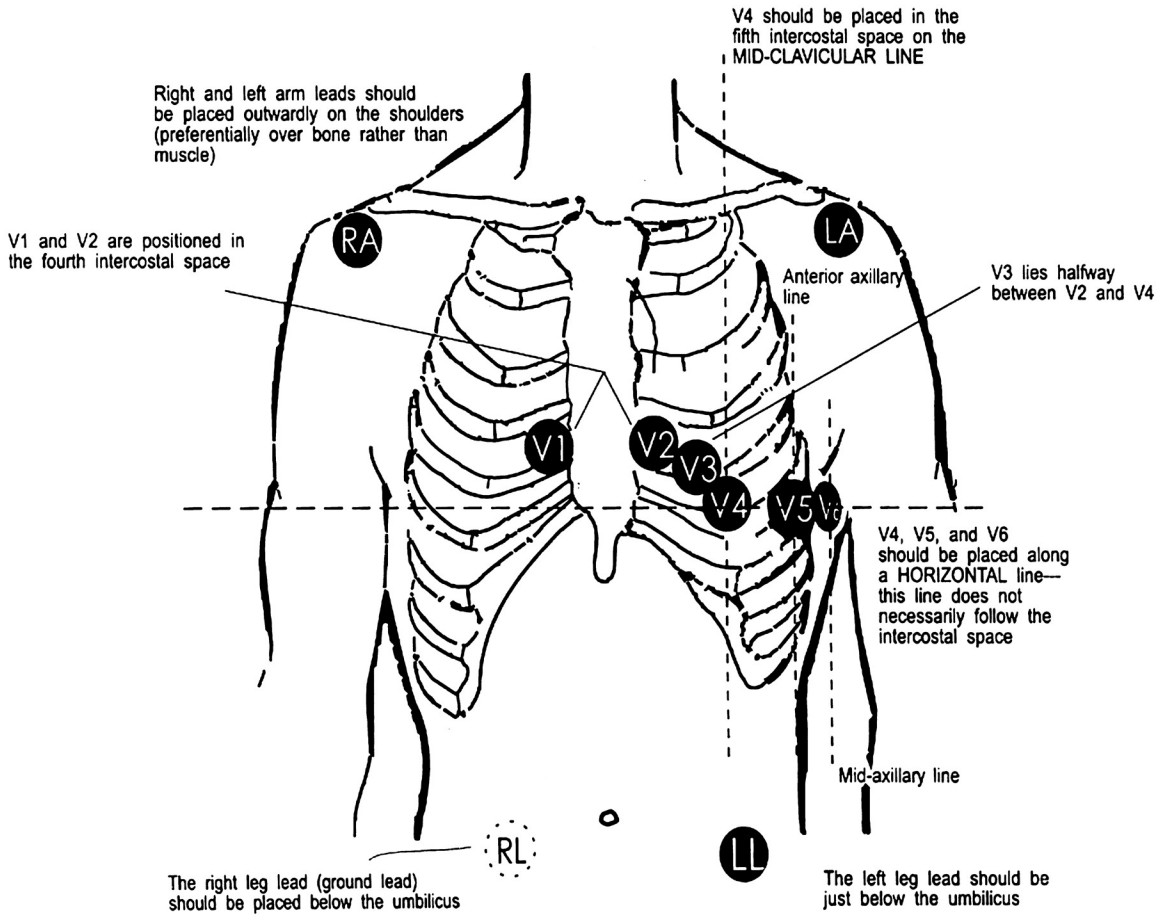

Figure 2-7: Electrode placement for a standard 12 lead ECG (figure from [17])

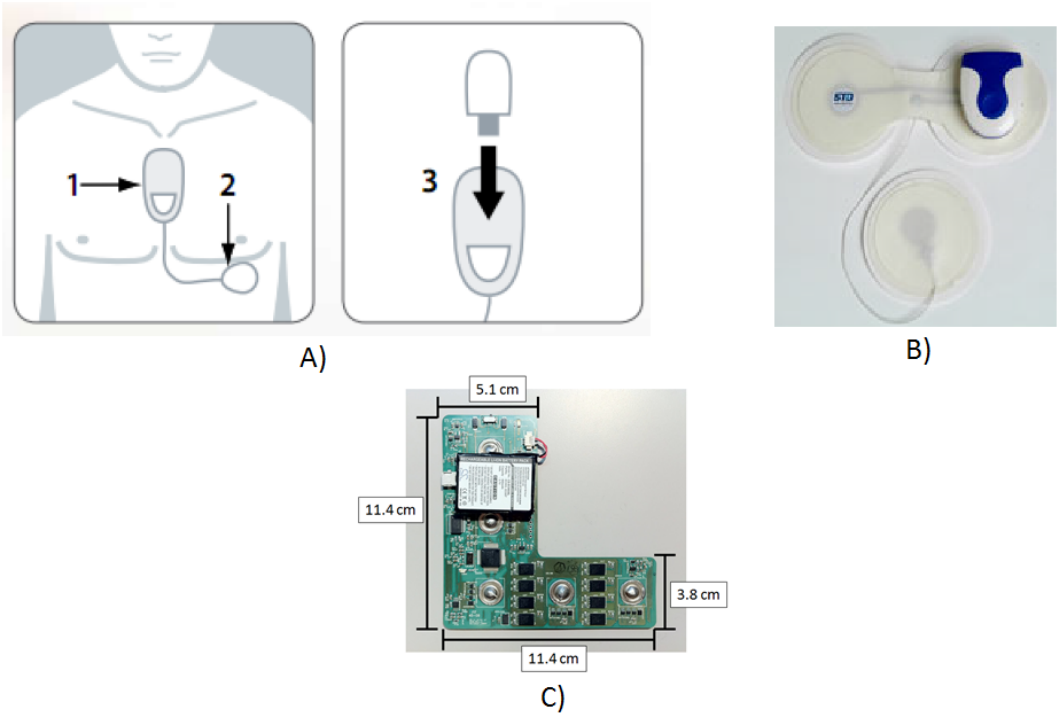

Figure 2-8: A) The Mindray Netguard [20], B) The V-Patch [21], C) The Wearable Cardiac Monitor [22]

Figure 2-9 shows the difference in signal quality between an ECG at the ear and an ECG at the chest [23]. The signal is attenuated by about a factor of 100, meaning that the R-waves at the ear are on the order of 10s of μvolts compared to millivolts. This attenuation is due to taking the measurement further from the source (head compared to chest) while also using two electrodes in close proximity to each other (4cm instead of 15cm at the chest).

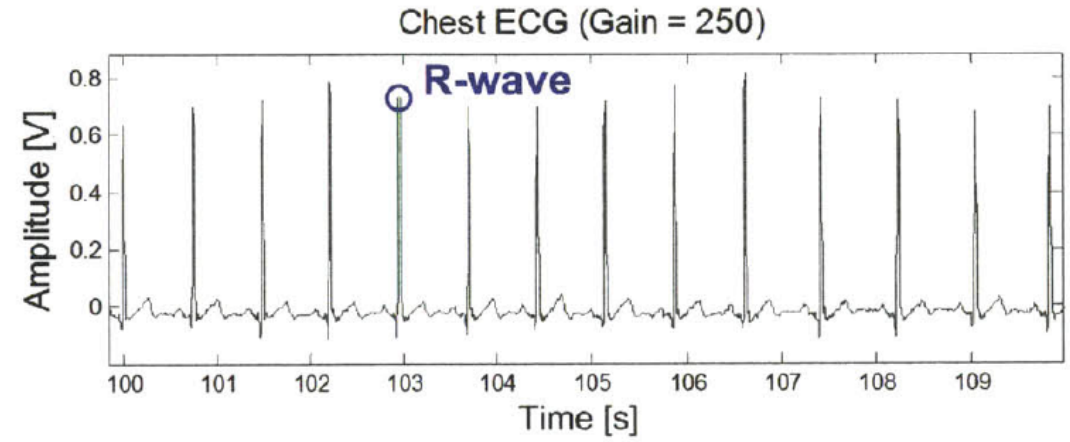

(a)

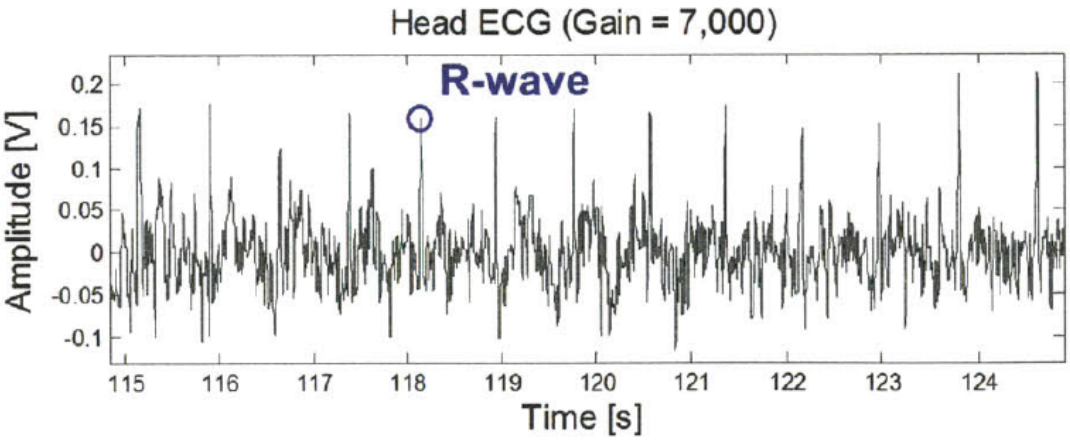

(b)

Figure 2-9: a) The ECG measured from the chest, and b) the ECG measured from the mastoid area behind the left ear. The ECG's are filtered with a 1 - 50 Hz bandpass filter. Measurements are not simultaneous.

2.3 The Photoplethysmogram (PPG)

2.3.1 Traditional PPG

The photoplethysmogram (PPG) is a non-invasive, optical, volumetric measurement of pulsatile blood flow in the peripheral vasculature. Traditionally, the PPG is obtained by transmitting light through a finger. The received light will have low frequency modulations due to the pulsation of the blood. PPG theory starts with the Beer-Lambert Law 2.2, which states:

$$I_t = I_0 e^{(-\alpha L)} \tag{2.2}$$

where I_0 is the incident light upon an absorbent medium, α is the absorption coefficient of the medium, L is the optical path length and I_t is the received light transmitted through the medium. Figure 2-10 graphically shows the Beer-Lambert Law.

Most of the optical absorbers in the body are slowly varying with time, such as skin thickness, hair and tissue [25] [26]. The portion of the PPG signal associated with these slowly varying absorbers will hence forth be denoted as I_{static}. In addition to I_{static}, there is a second portion of the PPG signal due to the pulsatile arterial blood, which will be denoted as $I_{pulsatile}$. The PPG signal can therefore be thought of as:

$$I_{PPG} = I_{static} + I_{pulsatile} \tag{2.3}$$

where I_{static} is:

$$I_{static} = I_0 e^{(-\alpha_S L)} \tag{2.4}$$

and $I_{pulsatile}$ is:

$$I_{pulsatile} = I_0 e^{(-\alpha_A \Delta L)} \tag{2.5}$$

The pulsatile component typically has an amplitude $0.25-2\%$ of the static component. Note that α_S in equation 2.4 is the aggregate absorbance of the static components of

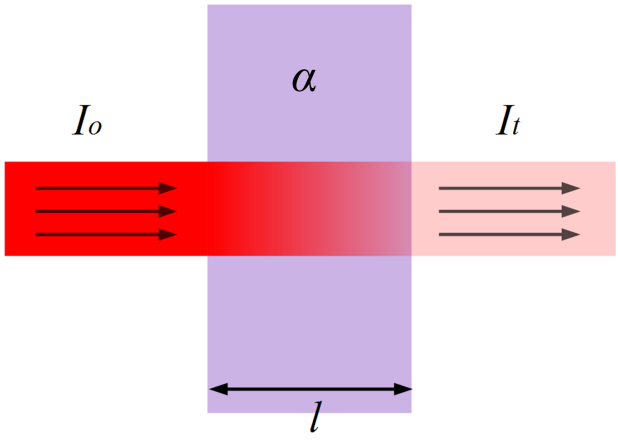

Figure 2-10: Beer's Law (figure adapted from [24]).

the PPG signal. Similarly α_A in equation 2.5 is the aggregate absorbance coefficient for arterial blood and ΔL is the change in optical path length due to the pulsatile arterial blood [27]. Clinically, two PPG signals can be used to obtain peripheral oxygen saturation (SpO_2), which will be discussed in more detail in section 2.3.3.

A typical PPG front end consists of several components, including a one or more light emitting diodes (LED), a LED driver, a photodiode (PD), a transimpedance amplifier (TIA), a demodulator, analog signal conditioning, an analog-to-digital converter (ADC), and a microcontroller unit (MCU), as shown in Figure 2-11. Usually, two different LED wavelengths (red and infrared (IR)) are used so that the SpO_2 value can be calculated. The LEDs are pulsed with low duty cycles to reduce system power consumption.

2.3.2 Head PPG

PPG signals at the head are obtained with the sensor operating in reflectance-mode instead of transmission-mode. In reflectance-mode, the LEDs shine light into the body, and the backscattered light from tissue, blood and bone is received by PDs in the same plane as the LEDs, as shown in Figure 2-12. Several new challenges arise in reflectance-mode. First, the mechanical housing of the sensor may not be

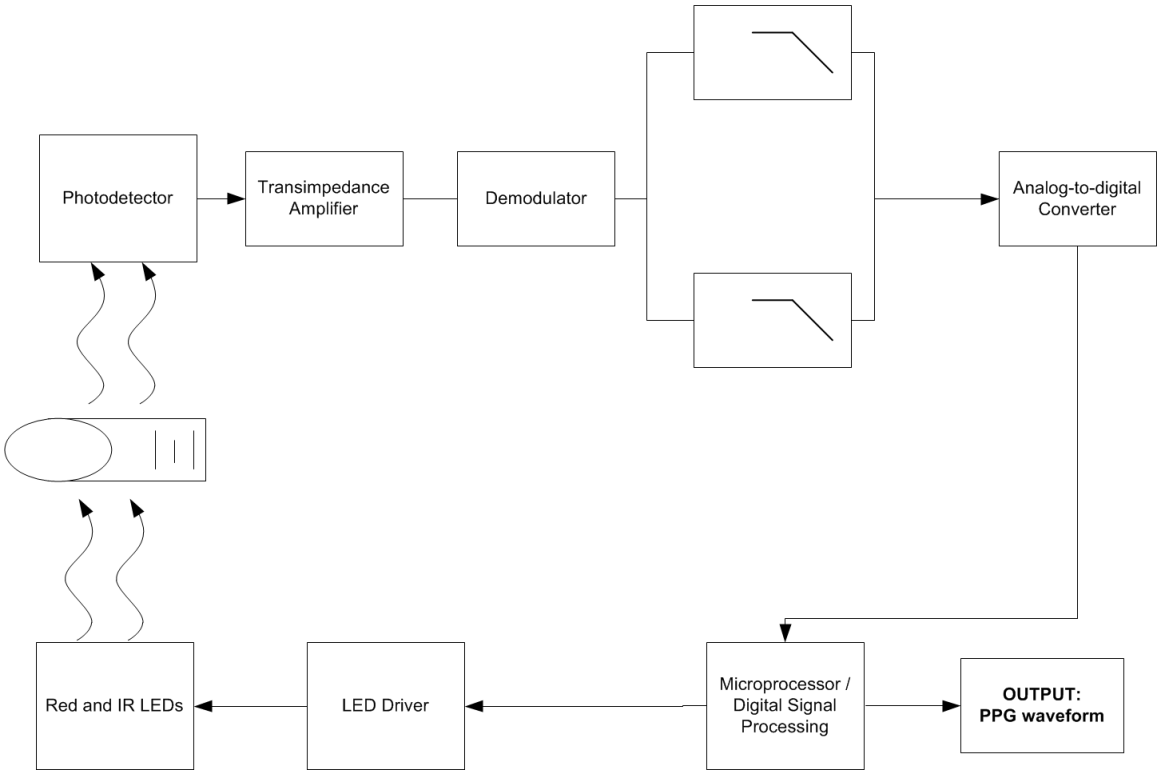

Figure 2-11: Block diagram of a typical pulse oximeter.

sufficient for blocking ambient light from the PDs, therefore, care must be taken when sampling and filtering to avoid aliasing interferers into the PPG bandwidth of interest. Second, reflectance-mode measurements are often part of wearable systems, which require low-power and low-voltage operation to reduce the battery size and optimize the form factor. To help mitigate these issues, the wearable CHF monitor uses a dynamic range enhancement (DRE) circuit to lower the voltage of the PPG front end and reduce the resolution requirements of the analog-to-digital converter (ADC), which is discussed in section 4.1.1.

Head PPG signals are similar to PPG signals obtained by transmission through the finger, as shown by Figure 2-13. The morphological differences are due to the vascular transmission line which sends the pulse from the heart to the head compared to the finger. The equations describing the static and pulsatile PPGs in section 2.3.1 also hold for reflectance mode PPG, with the difference that the optical path length is now 2 times the distance to the scatterer, instead of the thickness of the finger.

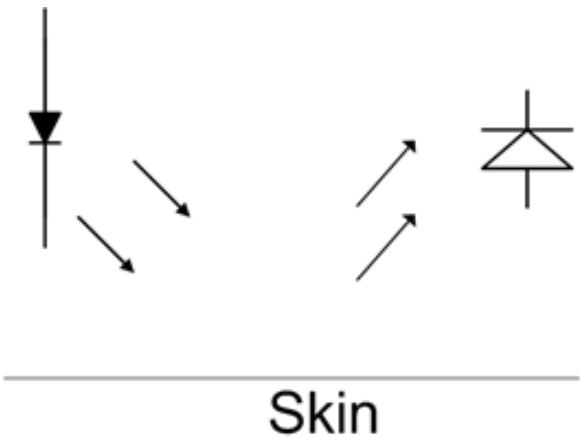

Figure 2-12: Graphical representation of reflectance -mode photoplethysmography. The LED emits light into the skin., then reflected light is collected by the photodiode, which is physically in the same plane as the LED.

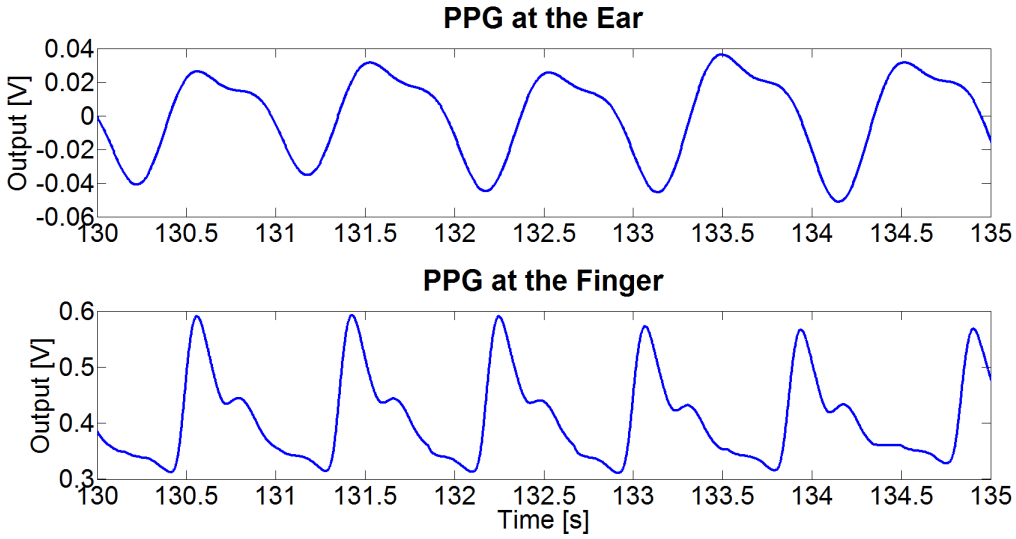

Figure 2-13: Top: PPG taken from the mastoid region behind the left ear. Bottom: PPG taken from the finger (measurements not simultaneous).

2.3.3 The Photoplethysmogram and Pulse Oximetry

Arterial oxygen saturation (SaO_2) is the amount of oxygenated versus total hemogloben in the arterial blood. Under normal conditions, this value is very close to 1, which is known as 100% oxygen saturation. Under certain conditions, such as when gas transport in the lungs is diminished, this value can dip significantly below 100%. Patients with lung diseases such as chronic obstructive pulmonary disease (COPD) or conditions such as pulmonary edema caused by CHF, have been known to live with stable oxygen saturation closer to 90% or below [28] [29].

To quickly and non-invasively estimate SaO_2, two PPGs can be used to calculate the peripheral oxygen saturation (SpO_2). SpO_2 is a measure of oxygenated versus total hemogloben in the peripheral vasculature bed where the PPGs are being measured, and is usually a very good indicator of SaO_2. Clinically, SpO_2 monitoring is used widely in anesthesia as well as disease management for COPD and CHF patients.

To understand how to go from a PPG waveform to SpO_2, start with the absorbance coefficient α_A in equation 2.5. α_A is dependent on the percentage of oxygenated to de-oxygenated hemoglobin in the arterial blood and is defined as:

$$\alpha_A = (\alpha_{OA})(SaO_2) + (\alpha_{DA})(1 - SaO_2) \tag{2.6}$$

where SaO_2 is the arterial oxygen saturation, described in terms of oxygenated and de-oxygenated hemoglobin as $\frac{HbO_2}{Hb+HbO_2}$, α_{OA} is the absorbance of oxygenated hemoglobin and α_{DA} is the absorbance of de-oxygenated hemoglobin.

As can now be seen in equation 2.6, the arterial oxygen saturation SaO_2 is embedded in α_A. Therefore, a derivative of 2.5 is taken to obtain α_A:

$$\frac{(\frac{dI_{pulsatile}}{dt})}{I_{pulsatile}} = -\alpha_A * \frac{dL}{dt} \tag{2.7}$$

The final portion of the derivation requires additional knowledge of the absorbance of blood to different wavelengths of light. Figure 2-14 shows optical absorbance curves for oxygenated and de-oxygenated hemoglobin for wavelengths from 600nm to

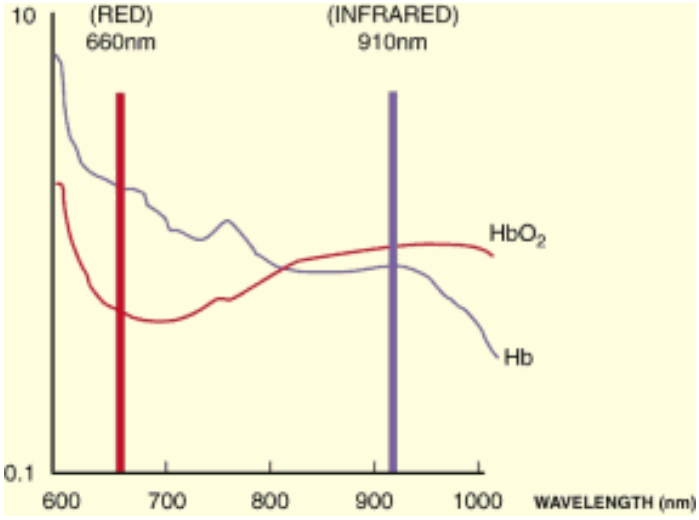

Figure 2-14: Oxygenated and de-oxygenated hemoglobin absorbance versus wavelength.

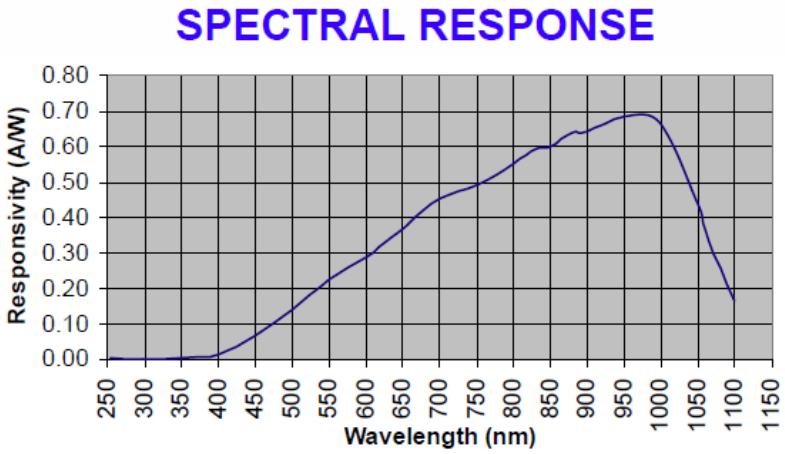

Figure 2-15: A responsivity curve of an Advanced Photonix PDB-C160SM silicon PIN photodiode.

1000nm. Optically, when blood is rich in oxygen, it is bright red in color. As blood de-oxygenates it becomes darker. Therefore, one can think of measuring the oxygenation of blood by comparing it's red absorbance against a reference, typically infrared (IR). IR is used for two reasons. Physiologically, the ratio of red and IR absorbance for oxygenated and de-oxygenated hemoglobin has a wide dynamic range compared to other wavelengths as is shown in Figure 2-14. Electrically, silicon photodiodes are very responsive to IR frequencies, increasing the SNR of those signals as shown in Figure 2-15. Taking a ratio of equation 2.7 for two different wavelengths removes

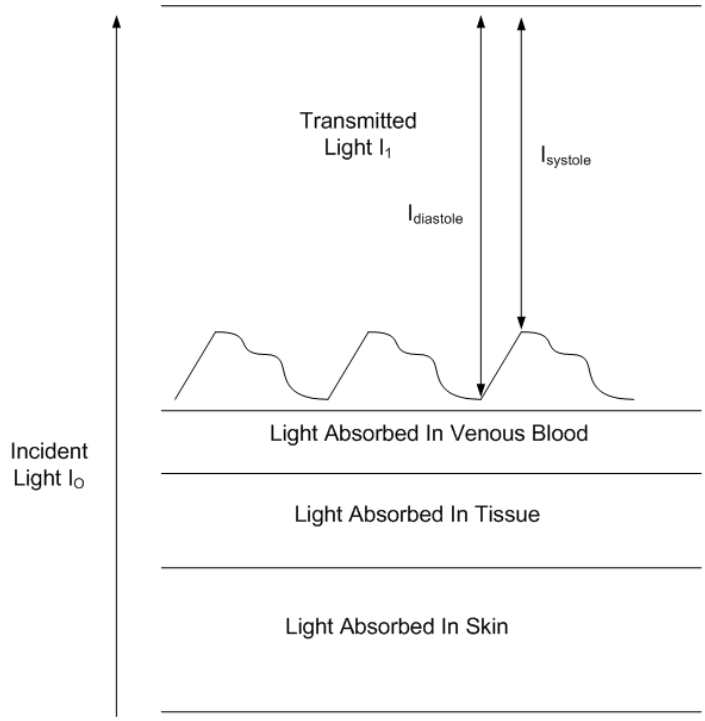

Figure 2-16: Samples taken at systole and diastole for the red and IR PPG waves can be used to approximate the RoR.

the dependence of $\frac{dL}{dt}$ from 2.7. This ratio of ratios (RoR) becomes:

$$RoR = \frac{(\frac{dI_R(t)}{dt} \frac{}{I_R})}{(\frac{dI_{IR}(t)}{dt} \frac{}{I_{IR}})} = \frac{\alpha_A(\lambda, _R)}{\alpha_A(\lambda, _{IR})} \tag{2.8}$$

Equivalently, Figure 2-16 shows that equation 2.8 can be approximated by using samples taken only at systole and diastole.

$$RoR \approx \frac{(\frac{I_R(systole) - I_R(diastole)}{\frac{I_R(systole) + I_R(diastole)}{2}})}{(\frac{I_{IR}(systole) - I_{IR}(diastole)}{\frac{I_{IR}(systole) + I_{IR}(diastole)}{2}})} \tag{2.9}$$

Finally, in it's most basic form, SpO_2 has been empirically shown to be related to

two constants and the RoR [27].

$$SpO_2 = C_1 - C_2 * RoR \tag{2.10}$$

where C_1 and C_2 are factory calibrated constants which depend upon the characteristics of the measurement system and are not subject dependent. A more physiologically thorough derivation can be found in Chapter 4 of [27].

2.4 Heart Intervals

Several physiologically pertinent parameters can be obtained by combining timing information from multiple signals measured by the wearable CHF monitor. The following sections will discuss the pre-ejection period, pulse transit time, and pulse arrival time, and their clinical relevancy.

2.4.1 The Pre-ejection Period (PEP)

The pre-ejection period (PEP) of the heart is defined as the beginning of ECG's Q-wave to the time that the aortic valve opens and the left ventricle begins pushing blood into the aorta. This electro-mechanical (EMD) delay first is composed of the electrical depolarization of the ventricles, noted by the QRS complex of the ECG, and then the mechanical isovolumic contraction time (ICT), where the left ventricle is contracting, but the internal pressure has not become large enough to open up the aortic valve, as shown in Figure 2-17.

The PEP is a measure of heart muscle strength, as the weaker the heart muscle, the longer it takes to generate the internal pressure to open up the aortic valve. The heart muscle strength is referred to as cardiac contractility. This elongation of the PEP can be especially pronounced in heart failure patients [31].

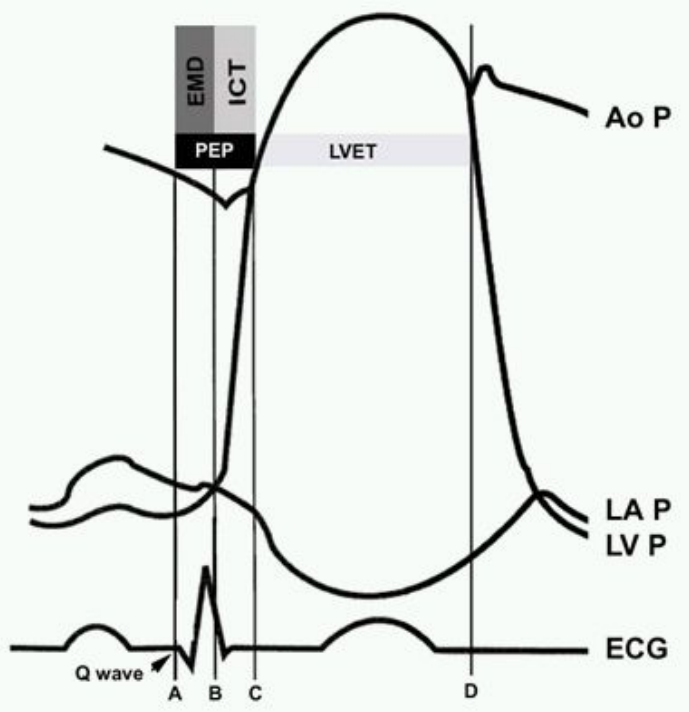

Figure 2-17: The pre-ejection period, which includes the electromechanical delay (EMD) and isovolumic contraction time (ICT) of the left ventricle. The left ventricular ejection time (LVET) denotes the duration that the aortic valve is open. Figure from [30].

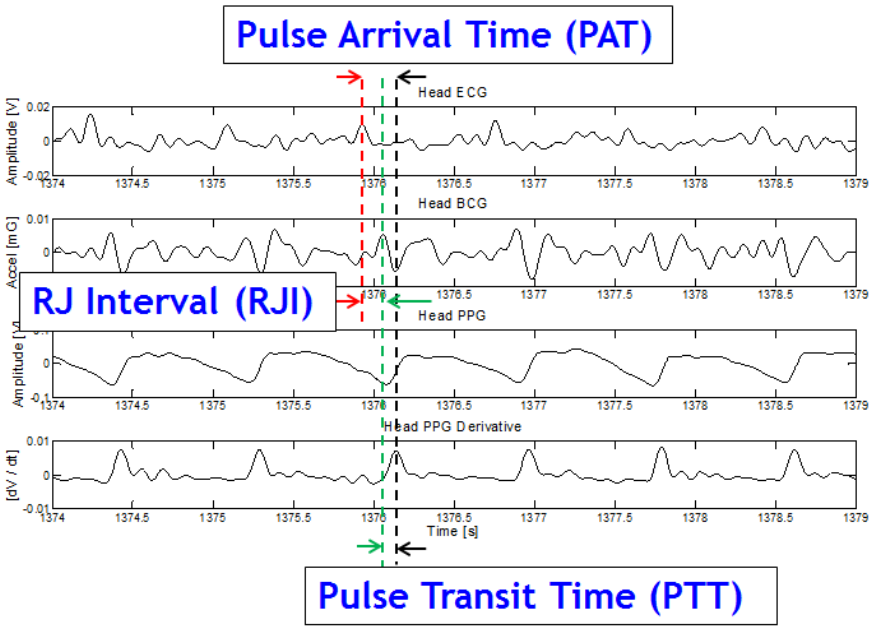

Figure 2-18: From top to bottom, the head ECG signal, the head BCG signal, the head PPG signal, and the derivative of the head PPG signal. The RJI, defined as the peak of the R-wave of the ECG to the peak of the J-wave of the BCG correlates to the heart's PEP. The PTT, defined as the peak of the J-wave of the BCG to the peak of the derivative of the PPG, correlates to mean blood pressure. The PAT, defined as the peak of the R-wave of the ECG to the peak of the derivative of the PPG includes both the PEP and PTT intervals.

Estimating the PEP using the RJ Interval

The time interval between the R-wave of the ECG and the principle peak of the BCG (J-wave) is known as the R to J interval (RJI), as shown in Figure 2-18. Figure 2-19 shows that the PEP and RJI have high correlations, since the RJI includes the PEP, plus a small transit time from the aortic valve to the aortic arch [4] [32]. Figure 2-20 graphically describes the direction of blood flow as it leaves the heart and moves from the aorta, to the aortic arch, and eventually the ear. Using the R-wave peak as the start of the PEP instead of the Q-wave is a valid assumption, as the qR interval is usually short and constant. The R-wave also has significantly higher SNR than the Q-wave at the ear, which allows for automated algorithms such as cross-correlation, to estimate the PEP from the wearable CHF monitor data [23].

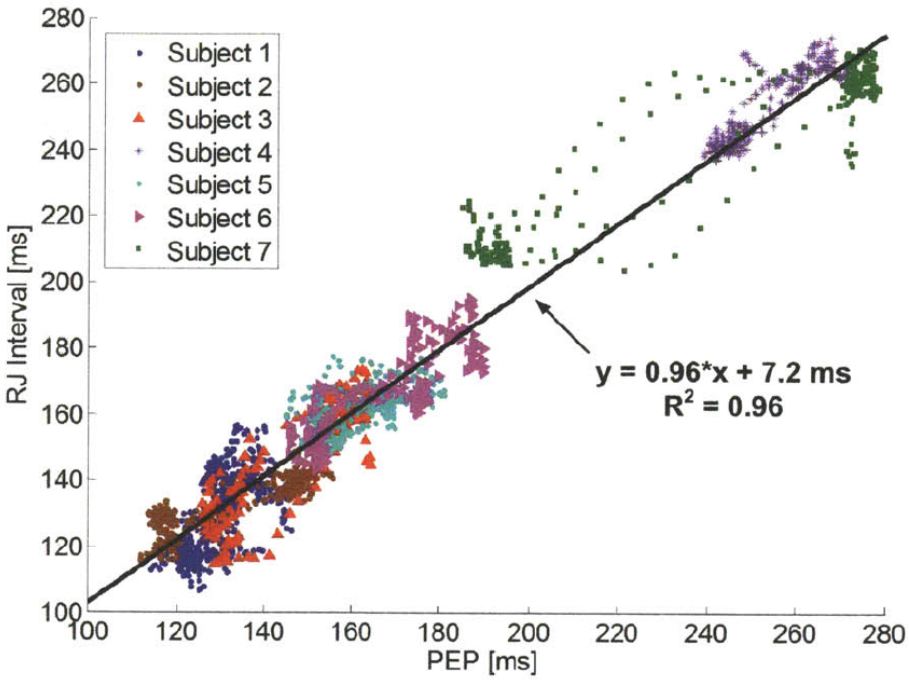

Figure 2-19: The beat-to-beat RJ Interval and PEP among seven subjects during 28 tilt maneuvers (Figure from [4]).

2.4.2 Pulse Transit Time (PTT)

Pulse transit time (PTT) is defined as the time it takes for a blood pulse to go from one point in the body, to another point in the body. Traditionally, PPG signals at two different locations are used to obtain the PTT. To measure this delay, a specific feature is chosen on both PPG signals, typically the foot, peak, or peak of the derivative [33] [34], as shown in Figure 2-21. There is a fluid dynamics model, derived in section 3.6, detailing how a shorter PTT corresponds to an increase in internal pressure along the vessel being measured.

The wearable CHF monitor uses the J-wave from the BCG as the first time marker for PTT, and the edge of the PPG from behind the ear as the second time marker, as shown in Figure 2-18. Measuring the PTT from the aortic arch, up the carotid to the ear and using the fluid dynamics model derived in section 3.6 allows estimation of mean arterial pressure (MAP) to the head, in a continuous and non-invasive manner while only using a single site of measurement.

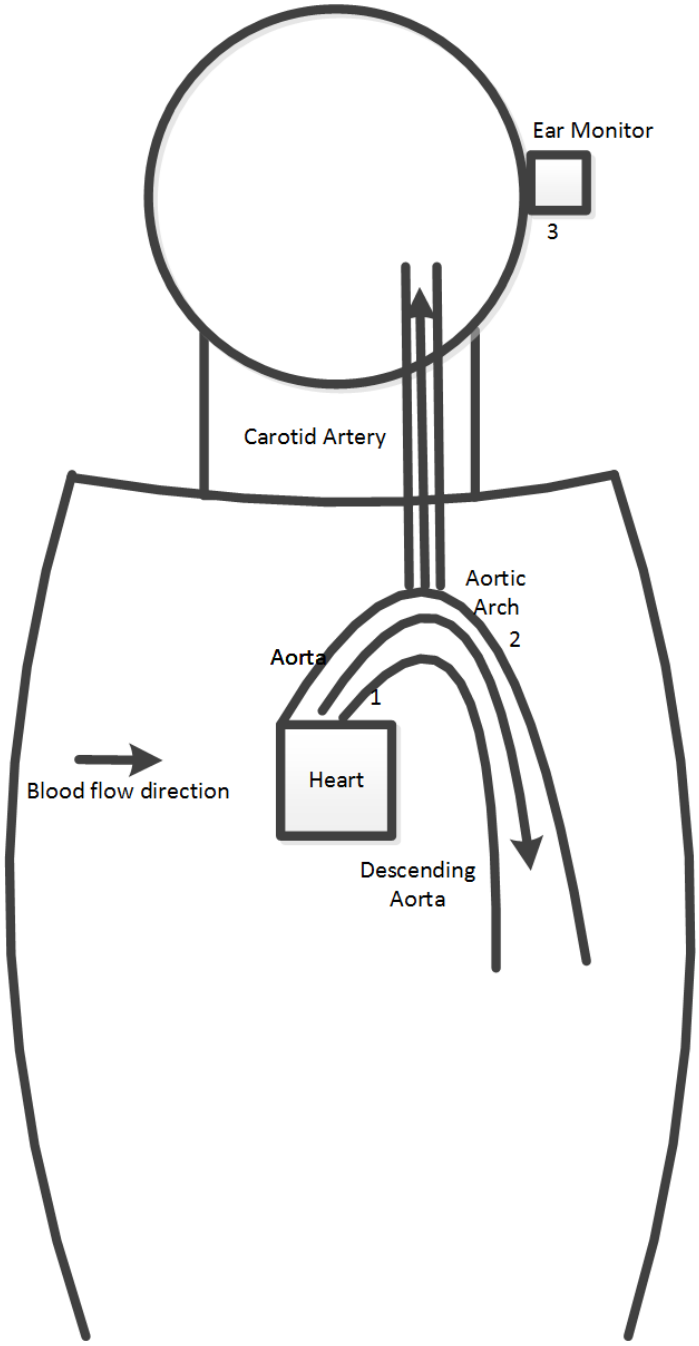

Figure 2-20: The blood is expelled by the heart (1) and heads to the aortic arch (2), where it then travels up the carotid artery and arrives behind the ear (3). The J-wave occurs at (2) and the PPG arrives at (3) for the wearable CHF monitor.

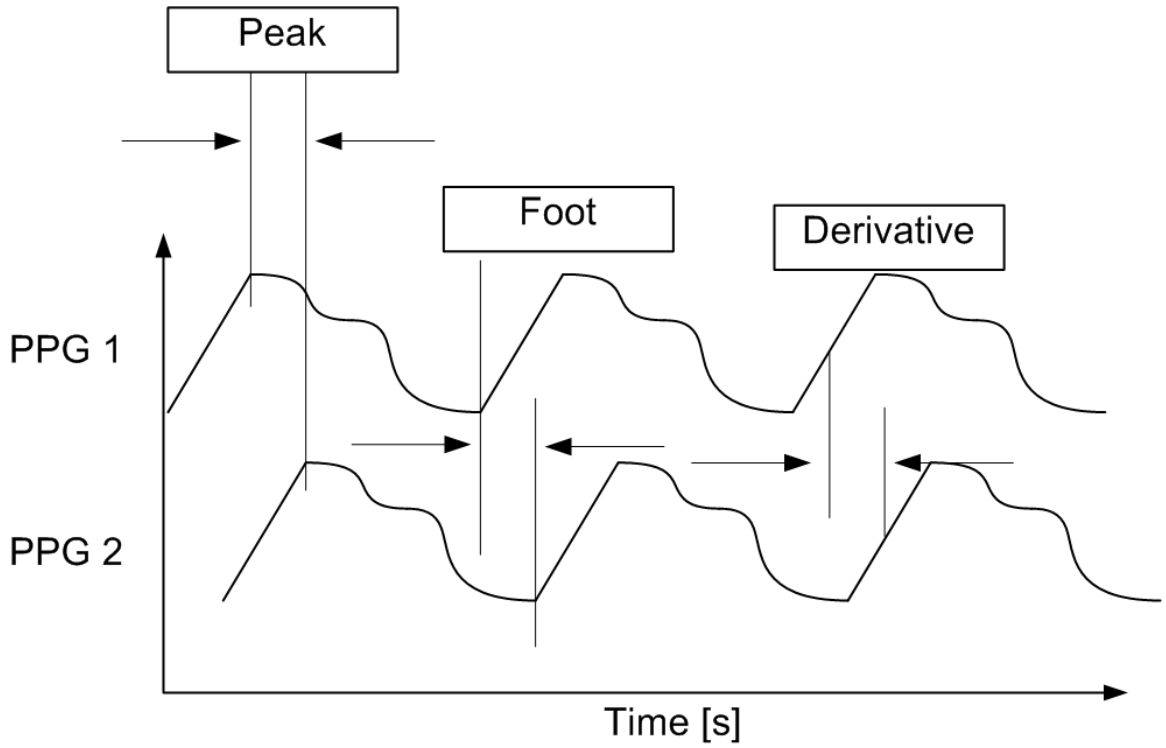

Figure 2-21: Three ways to traditionally measure pulse transit time, the peak-to-peak, foot-to-foot, and peak-of-derivative to peak-of-derivative.

2.4.3 Pulse Arrive Time (PAT)

Pulse arrival time (PAT) is the interval from the R-wave of the ECG to either the trough, peak, or peak of the derivative of the PPG, as shown in Figure 2-18 [35] [36] [33] [34]. This interval encompasses both the PEP of the heart, and the transit time of the blood from the aorta to wherever the PPG is taken on the body.

Due to it's ease of measurement, the PAT interval has been used by many groups to try to correlate to non-invasive blood pressure [37] [38] [39]. However, because of the PEP, which is not directly related to blood pressure, this interval may not always be a good indicator. Section 4.3 shows cases where the PAT both shows good and bad correlation to MAP.

2.5 Summary

A mechanical (BCG), electrical (ECG) and optical signal (PPG) have been introduced. Traditional measurement methods and morphologies have been compared to

those from behind the ear using the wearable CHF monitor. A derivation for obtaining SpO_2 using multiple PPG wavelengths was also explored. Three timing intervals (RJI, PTT, and PAT) obtained through combinations of the BCG, ECG, PPG, were described. The RJI was shown to be directly correlated to the heart's PEP and the PTT was mentioned as a proxy for internal blood pressure measurements. The PAT is a combination of both the RJI and PTT.

Chapter 3

Non-implantable Methods of Measuring Arterial Blood Pressure

This chapter begins with an introduction to arterial blood pressure and it's classifications. Several non-implantable methods for measuring arterial blood pressure are then discussed. Next, a relationship between pulse transit time (PTT) and mean blood pressure is derived. Finally, inaccuracies in the relationship are theoretically explored and potential improvements are proposed.

3.1 Arterial Blood Pressure

Arterial Blood pressure (ABP) is defined as the pressure of the blood in the arterial system, which depends on the heart's pumping pressure, the resistance of the arterial walls, elasticity of vessels, the blood volume, and its viscosity. [40]. Each cardiac cycle has a maximum and minimum value for blood pressure, denoted as systolic and diastolic blood pressure respectively, as shown in Figure 3-1. Normal values for systolic blood pressure are between 90 - 120 mmHg and normal values for diastolic blood pressure are between 60 - 80 mmHg. Mean arterial pressure (MAP), is defined as the average blood pressure in the aorta, and is estimated by:

$$MAP = P_{distolic} + \frac{(P_{systolic} - P_{diastolic})}{3} \tag{3.1}$$

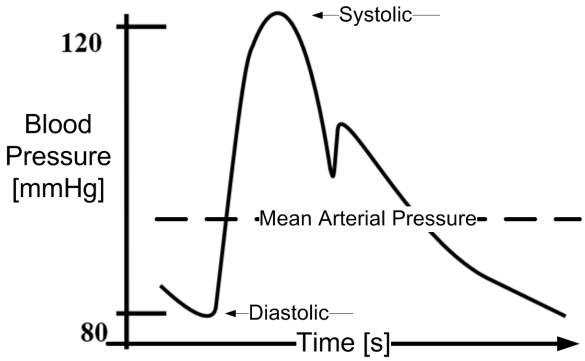

Figure 3-1: A typical blood pressure waveform over 1 cardiac cycle with the systolic, diastic and mean arterial pressure points denoted (Figure from [41]).

Low blood pressure, also known as hypotension is defined as when either systolic or diastolic pressures are below the clinical normal values of 90 or 60 respectively. Symptoms of hypotension can include dizziness and fainting and can be caused by heart malfunction or neurological disorders among other conditions [42].

High blood pressure, also known as hypertension, is defined as when either systolic or diastolic pressures are higher than the clinical normal values of 120 or 80 respectively. Hypertension causes the heart to work harder to pump blood into the body and significantly increases the risk of heart attack, stroke, and heart failure. Hypertension in the US accounts for nearly $100 billion in health care services, medication and lost productivity [43]. Table 3.1 shows clinical diagnoses for measured systolic and diastolic blood pressure values [42] [44].

Catagory	Systolic, mmHg	Diastolic, mmHg
Hypotension	<90	<60
Desired	90-120	60-80
Prehypertension	120-140	80-90
Stage 1 Hypertension	140-160	90-100
Stage 2 Hypertension	160-180	100-110
Hypertensive Emergency	≥180	≥110

Table 3.1: Adult Classification of Blood Pressure

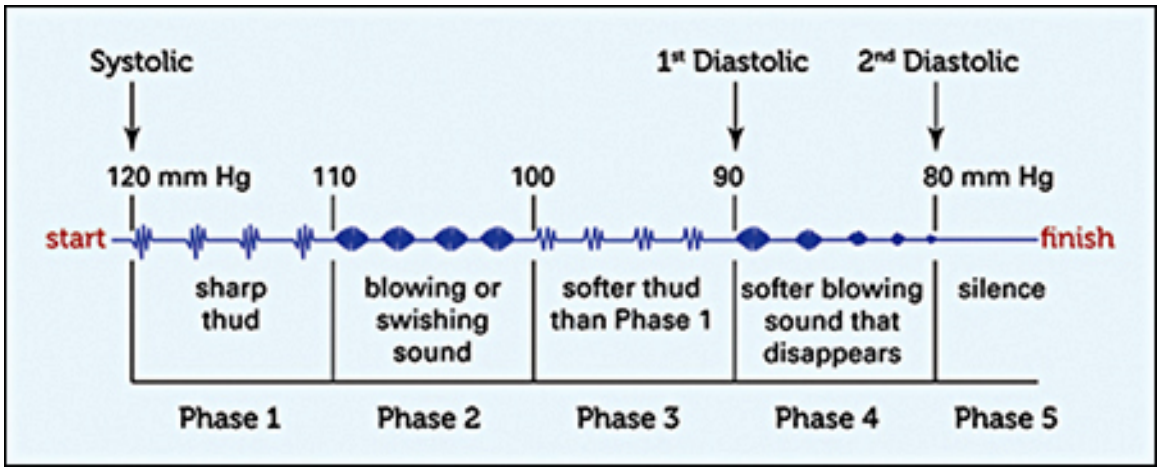

Figure 3-2: The five Korotkoff sounds and their clinical significance (Figure from [46]).

3.2 Sphygmomanometry / Auscultatory

Blood pressure is normally measured by a sphygmomanometer and stethoscope. The sphygmomanometer is comprised of an inflatable cuff, and a mechanical meter to display the pressure in millimeters of mercury (mmHg). The cuff is placed around the biceps of a patient and inflated until blood flow is cut-off. The cuff is then slowly deflated while a clinician listens through a stethoscope placed on the radial artery at the elbow. When blood begins flowing to the arm again, a snapping or whooshing sound is heard, which is defined as the first Korotkoff sound and is equal to when the cuff is pressurized to the systolic pressure [45]. As the pressure in the cuff drops, more sounds are heard corresponding to the 2nd through 4th Korotkoff sounds. These sounds are due to turbulent blood flow through the artery caused by external pressure from the cuff. Eventually, the 5th Korotkoff sound, which is the absence of sound, corresponds to when the cuff is at diastolic pressure. Figure 3-2 details the five Korotkoff sounds and their clinical significance.

3.3 Arterial Tonometry

Arterial tonometry is a noninvasive technique of measuring the full blood pressure waveform [47]. Tonomotry works by placing a hand-held strain gauge over the radial

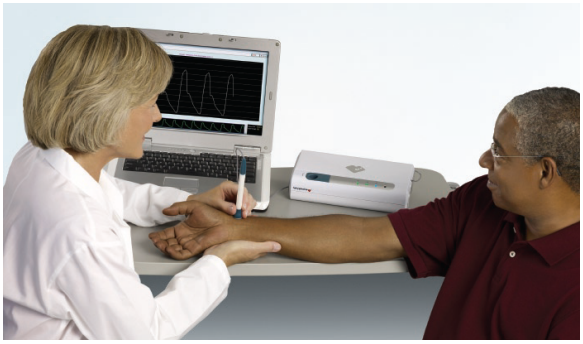

Figure 3-3: The SphygmoCor CP tonometer system from AtCor Medical (Sydney Australia).

artery and applying mild pressure to partially flatten the artery. The strain gauge detects the internal pressure of the radial artery as a change in strain on the sensor. Fast Fourier transform (FFT) algorithms have been approved by the Food and Drug Administration (FDA) for internal pressure readings [47]. Figure 3-3 shows a SphygmoCor CP tonometer system from AtCore Medical (Sydney, Australia). Tonometers are known for high accuracy blood pressure readings at the expense of a trained technician applying pressure with the sensor to obtain the data.

3.4 Oscillometry

Oscillometry is similar to Auscultatory in that an inflatable cuff is placed around the biceps. However, oscillometers are usually controlled by automatic methods and do not require a trained clinician to take measurements manually once the device has been placed on the patient. Oscillometers work by inflating cuff pressure until blood flow has ceased. The cuff is then slowly deflated, and when blood flow is present, but restricted, the pressure transducer inside the cuff will oscillate with the pulsatile waveform. Automatic algorithms estimate systolic and diastolic values for the blood pressure based on these oscillations. Many continuous blood pressure cuffs are oscillometers, and will periodically inflate to take blood pressure measurements, however due to their sensing nature of cutting off blood flow to the arm, only one measurement every few minutes can be obtained. The output of the oscillometer are

Figure 3-4: The BP 3AC1-1 PC Oscillometer from Microlife (Widnau, Switzerland).

the systolic and diastolic values, not the entire blood pressure waveform. Figure 3-4 shows an oscillometer from Microlife (Widnau, Switzerland).

3.5 The Volume Clamp Method

The volume clamp method, utilized by the Finapres Portapres [48] and Unitron Nexfin [49], is another way to obtain the complete continuous blood pressure waveform without implanting a device inside the body. The volume clamp method uses a small inflatable cuff, which wraps around a finger. The pressure between the cuff and finger is adjusted to maintain a constant volume of blood in the finger, which is measured by a photoplethysmogram. During systole, a higher pressure is required to squeeze out excess blood, while during diastole, a lower pressure is used since blood volume is decreased in the finger. A proportional-integral-derivative (PID) controller electrically controls an air valve to maintain a constant value of the PPG from the finger. The output of the device is cuff manometric pressure. Figure 3-5 shows a block diagram of the Finapres controller. Although convenient for continuous blood pressure measurements, the cost of a Finapres Portapres is on the order of $\$10,000$ and it's accuracy is at times suspect.

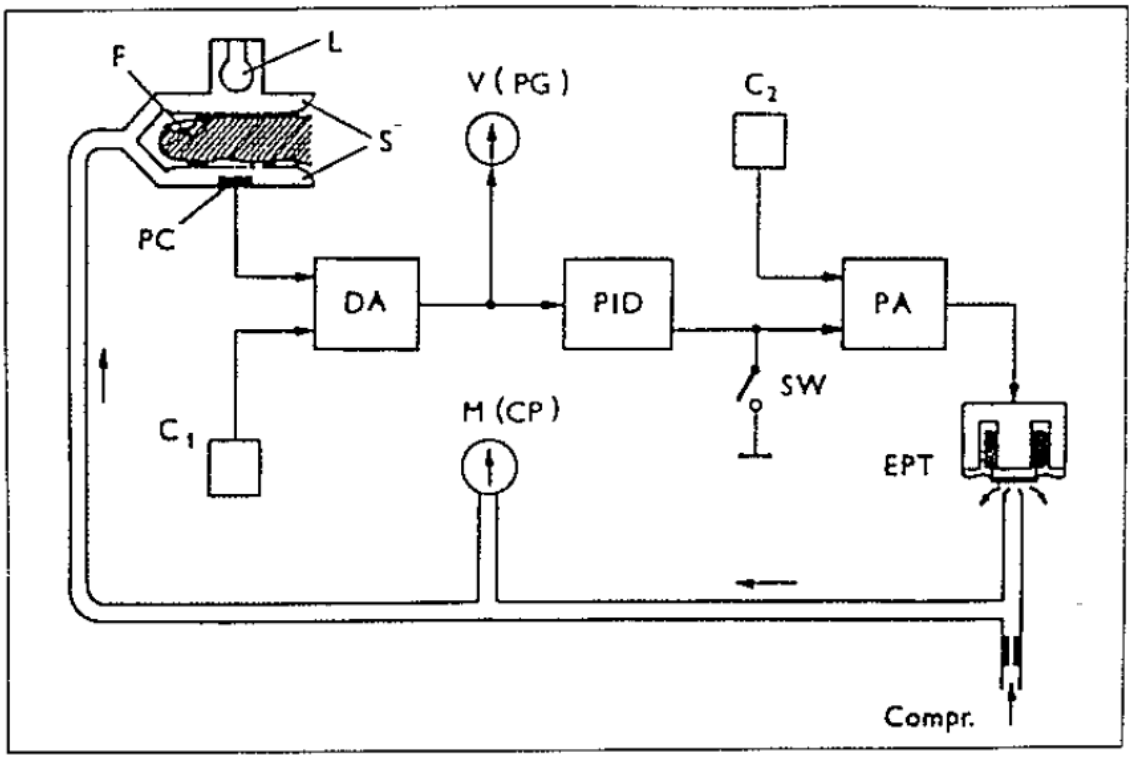

Figure 3-5: The control loop for a Finapres Portapres, (Figure from [48]).

3.6 Pulse Wave Velocity (PWV) and Pulse Transit Time (PTT)

Pulse wave velocity (PWV) is the velocity that a pulse wave travels along a tube, or in the physiologic sense, an artery. Many groups have looked into using PWV to correlate to blood pressure, which can be intuitively thought of in the following manner. If a rubberised tube is filled with a viscous liquid, it will have an internal pressure P_1. If one end of the tube is tapped with your hand, a small pulse wave will travel from the tapped end of the tube to the other end. The time it takes for the pulse wave to travel from one end to the other is called the pulse transit time (PTT). Now what happens if the internal pressure of the tube is increased to P_2? Tapping the same end of the tube, the pulse wave will once again travel from one end to the other, however this time it will travel faster. Therefore, if the properties of the tube remain constant, one can measure the PTT and have a proxy for the internal pressure of the tube.

Mathematically, PWV is related to PTT by:

$$PWV = \frac{\Delta X}{PTT} \tag{3.2}$$

where ΔX is the distance traveled (m). Next, it can also be shown using the Moens-Korteweg equation that:

$$PWV = \sqrt{\frac{Eh}{2r\rho}} \tag{3.3}$$

where E is the Young's modulus of the tube ($\frac{kg}{m \cdot s^2}$), h is the thickness of the tube (m), r is the inner radius of the tube (m), and ρ is the density of the viscous fluid ($\frac{kg}{m^3}$) [50] [51].

If instead of a tube, the large arteries are substituted, then the viscous fluid becomes blood, and Young's modulus is described by:

$$E = E_o e^{\alpha P} \tag{3.4}$$

where E_o is the value of Young's modulus when P equals zero, P is the mean arterial pressure (MAP) ($mmHg$), and α is a fitting coefficient with units ($\frac{1}{mmHg}$) [52]. Plugging equation 3.4 into equation 3.3 yields:

$$PWV = \sqrt{\frac{E_o e^{\alpha P} h}{2r\rho}} \tag{3.5}$$

Substituting equation 3.2 into equation 3.5 then taking a logarithm of both sides and solving for P yields:

$$P = \frac{1}{\alpha} ln(\frac{2r\rho\Delta X^2}{E_o h}) - \frac{2}{\alpha} ln(PTT) \tag{3.6}$$

Typical assumptions for using PTT to obtain MAP are that E_o, h, ΔX, ρ, r and α are all constant. Therefore, after calibrating for the constants, 3.6 becomes:

$$P = C_1 - C_2 ln(PTT) \tag{3.7}$$

where C_1 is $\frac{1}{\alpha} ln(\frac{2r\rho\Delta X^2}{E_o h})$ and C_2 is $\frac{2}{\alpha}$.

3.6.1 Inaccuracies with PWV

As mentioned in the previous section, many variables in equation 3.6 are considered to be constant. Several of these assumptions are valid over nearly all conditions, such as the length of the blood vessels (ΔX), the density of blood (ρ), and the thickness of the vessels (h). Other assumptions such as the radius of the vessel, may change due to ambient conditions (ie temperature), or changes in metabolic oxygen demand (ie periods of exercise).

One possible way to account for changes in the radius of the blood vessels, is to use the following simple relationship:

$$TPR = \frac{\Delta P}{Q} \tag{3.8}$$

where TPR is the total peripheral resistance ($\frac{mmHg}{\frac{L}{min}}$), ΔP is the drop in pressure from the aorta to the right atrium ($mmHg$), and Q is cardiac output ($\frac{L}{min}$). Cardiac output is defined as:

$$Q = SV \cdot HR \tag{3.9}$$

where SV is the stroke volume per heart beat ($\frac{L}{beat}$), and HR is the heart rate, with units of $\frac{beat}{minute}$. TPR can be related to vessel radius by the Hagen-Poiseuille equation:

$$TPR = \frac{8\Delta X \eta}{\pi r^4} \tag{3.10}$$

where ΔX is the length of the vessel (m), η is the viscosity of blood ($mmHg \cdot s$), and r is the vessel inner radius (m). Solving for r and plugging back into equation 3.8, it can be shown that the lumped vessel radius is proportional to:

$$r \propto \sqrt[4]{\frac{Q}{\Delta P}} \tag{3.11}$$

Therefore, a scaling factor can be defined as:

$$S_F = \frac{ln(\sqrt[4]{\frac{Q}{\Delta P}})}{ln(\sqrt[4]{\frac{Q_0}{\Delta P_0}})} \tag{3.12}$$

where Q_0 and ΔP_0 are values of cardiac output and MAP during calibration. The updated equation to go from PTT to MAP becomes:

$$P = C_1 S_F - C_2 ln(PTT) \tag{3.13}$$

The cardiac output Q can be estimated as $20.3\frac{mL}{mG} \cdot |Jwave| \cdot HR$ [4] and ΔP can be estimated from previous calculated values of MAP, making equation 3.13 recursive. The data in section 4.3.3 used beat-to-beat MAP and averaged Q over 10 beats to solve equation 3.13.

3.7 Summary

Arterial blood pressure and it's classifications were defined. Several methods of non-invasive blood pressure measurement were described. A derivation based on fluid dynamics showed the linear relationship between mean blood pressure and $ln(\frac{1}{PTT})$. Using the Hagen-Poiseuille equation and amplitude information from the BCG J-wave, improvements to the PTT-to-BP algorithm by accounting for the change in vessel radius are theoretically explored.

Chapter 4

The Clinical Test

The clinical test was designed to act as a proof of concept for the wearable CHF monitor. Results on heart rate, stroke volume (SV) and pre-ejection period (PEP) were discussed in [4]. The following sections delve into validations of continuous blood pressure and head PPG measurements. The chapter first discusses the wearable CHF monitor hardware and software. Then, the clinical testing protocol is introduced. Finally, the measurement results are analyzed to characterize head PPG morphology across test subjects and to assess the ability of the device to measure continuous blood pressure. The following sections 4.1.1, 4.1.2, 4.1.3, and 4.2 are reported in David He's PhD thesis [4] and are reproduced here with minimal changes for the reader's reference.

4.1 The Clinical Prototype

The wearable vital signs monitor is designed to measure the BCG, ECG and PPG at the ear and send data wirelessly in real-time to a computer for visualization, recording and analysis. A block diagram of the system is shown in Figure 4-1.

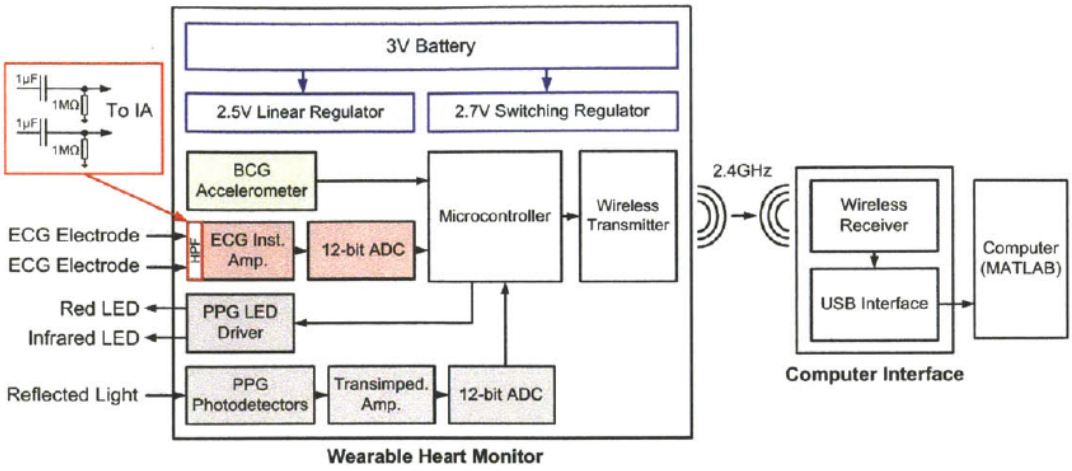

Figure 4-1: The system block diagram of the wearable CHF monitor with arrows indicating signal path.

4.1.1 Device Hardware

The hardware for the wearable vital signs monitor can be divided into several subsections. The BCG sensor is composed of a Bosch BMA180 accelerometer. This accelerometer was chosen for it's low-noise performance of $0.69mG_{RMS}$ within a 10Hz bandwidth with a $\pm 2G$ range. The ECG front end uses 2 capacitively coupled electrodes to sense the electrical signals from the heart at the head. An instrumentation amplifier (IA) (INA333, Texas Instruments) and 12 bit analog-to-digital converter (ADC) (AD7466, Analog Devices) complete the ECG signal chain, as shown in Fig. 4-2. The INA333 has an input noise of $0.16\mu V_{rms}$ for a $0.1Hz - 10Hz$ bandwidth, which is low enough to sense the $30\mu V$ ECG signals at the head. The electrodes are capacitively coupled to block DC voltages from the input of the IA. This is required because a third electrode is not present to set the common mode of the body. The ECG front end was designed by David He.

The PPG transmit chain uses a digital-to-analog converter (DAC) (AD5622, Analog Devices) and an operation amplifier (Op-Amp) (MCP603, Microchip) to create a drive voltage for a current sinking NFET (IRLMS2002PbF, International Rectifier). Two LEDs, red (LTST-C230CKT, Light-On Inc.) and IR (APT1608F3C, Kingbright Corp.) are connected to the battery voltage through a single pole, triple tap switch

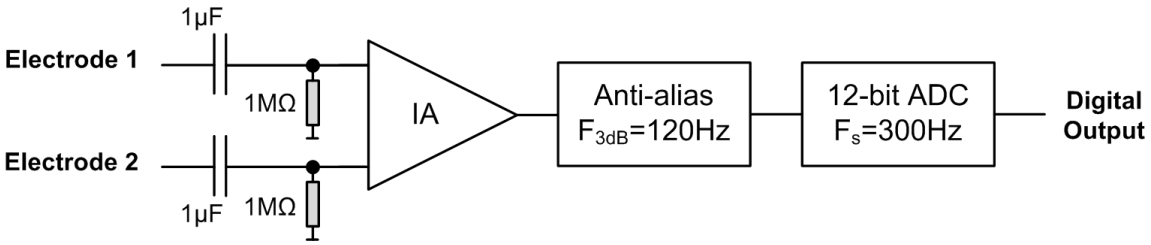

Figure 4-2: The ECG front-end from the wearable CHF monitor.

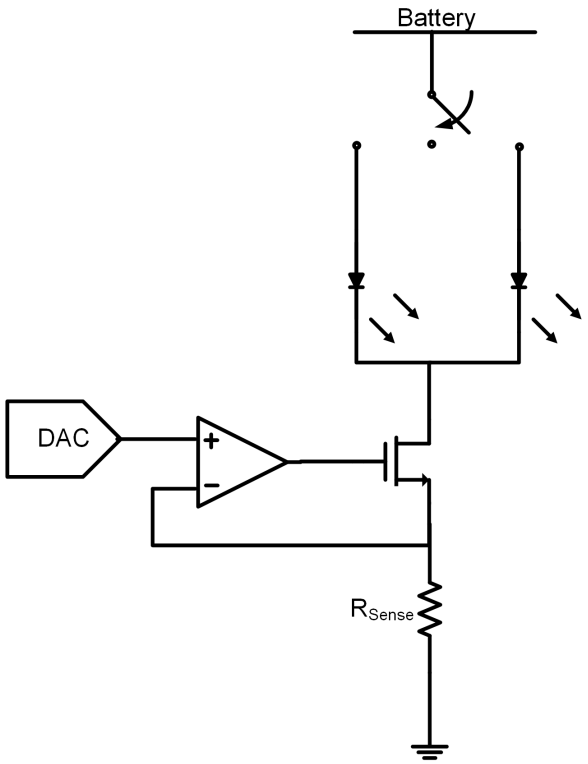

Figure 4-3: The LED drive for the CHF monitor.

(TS5A3359, Texas Instruments), as shown in Figure 4-3.

The PPG receive chain has 4 forward biased photodiodes (PD) (PDB-C160SM, Advanced Photonix) in parallel to collect the reflected photons and convert them to photocurrent I_{ph}. The photocurrent is amplified by a transimpedance amplifier (TIA) (MCP601, Microchip) and digitized by an AD7466. The transimpedance of the TIA is $1M\Omega$. The positive terminal of the TIA is connected to a DAC (AD5541A, Analog Devices) which generates voltage V_{ref}, as shown in Figure 4-4. The virtual ground of the TIA mirrors V_{ref} to be the same voltage as V_D, a forward potential across the

PDs. V_D induces a forward current I_F through the photodiodes:

$$I_F = I_S(e^{\frac{V_D}{V_T}} - 1) \tag{4.1}$$

where I_S is the reverse bias saturation current, and V_T is the thermal voltage $\frac{kT}{q}$. I_F subtracts a static amount of I_{ph} from the PPG signal, allowing for an increase in dynamic range without increasing the voltage supplies or decreasing the transimpedance gain.

Although the forward biased diodes increased the dynamic range of the PPG signal, this topology has several drawbacks which were addressed in the integrated version of the PPG front end. First, forward biased diodes have significantly higher capacitance than reverse biased, which slows down the front end and ultimately limits the LED duty cycle. Second, the forward current I_F has a strong temperature coefficient, which took several minutes to settle during the clinical test.

The microcontroller (MCU) (MSP430F2274, Texas Instruments) and radio (CC2500, Texas Instruments) are part of an EZ430-RF2500 daughter board which connects to an 18-pin header on the CHF monitor. The MCU continuously samples the BCG, ECG and PPG signals and sends the data to the radio via an SPI interface. The radio uses the open source SimpliciTI protocol to transmit to a USB receiver attached to a computer running MATLAB. The MCU also adjusts the LED drive currents and V_{ref} to ensure that the drive currents are not too high or too low, and that the output of the TIA is within the rails of the amplifier.

The energy source is a 3V 220mAh lithium coin cell battery (CR2032, Energizer). The power management circuitry regulates the battery voltage, first with a 2.7V buck-boost converter (TPS60242, Texas Instruments) to power the digital circuits, and then with a 2.5V low drop-out (LDO) regulator to power the analog circuits. A buck-boost was required first because the battery voltage dropped from 3V to 2V as it became discharged.

The USB receiver consists of another EZ430-RF2500 daughter board, which receives the wireless data and sends it to an UART-to-USB interface (FT232RL, FTDI).

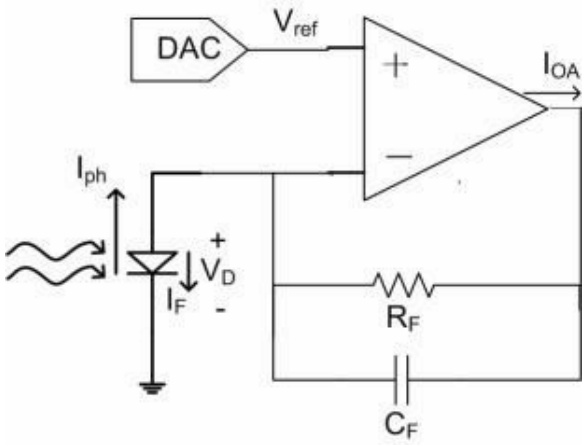

Figure 4-4: The PPG receive chain for the CHF monitor.

This creates a virtual COM port which can be accessed by computer software. MATLAB is used to record, plot and filter the BCG, ECG, and PPG signals in real time, as well as for off-line post-processing.

The prototype is shown in Figure 4-5 with labelled components. The red colored printed circuit board (PCB) is the EZ430-RF2500 daughter board. The PPG board is attached to the main board via an integrated flex connector that is designed to bend 180^o so that the PPG LEDs and PDs rest on the mastoid of the wearer. The PCBs are mechanically supported by a hearing aid housing manufactured by Taising Hearing Amplifier Ltd. and modified by David He. The device is anchored to the ear using the attached earbud. Two ECG electrodes are attached to the mastoid and neck using 3M Red Dot AgCl gel electrodes. All components on the side facing the wearer are coated in parylene-C (Paratronix) to ensure electrical isolation as part of clinical safety requirements. Figure 4-6 shows the device being worn at the ear with the ECG electrodes applied and the PPG board on the mastoid area hidden from view.

4.1.2 Device Firmware

The MSP430 MCU firmware on the wearable vital signs monitor serves four functions: the initialization of all circuits, the polling of data, adjusting the PPG front end

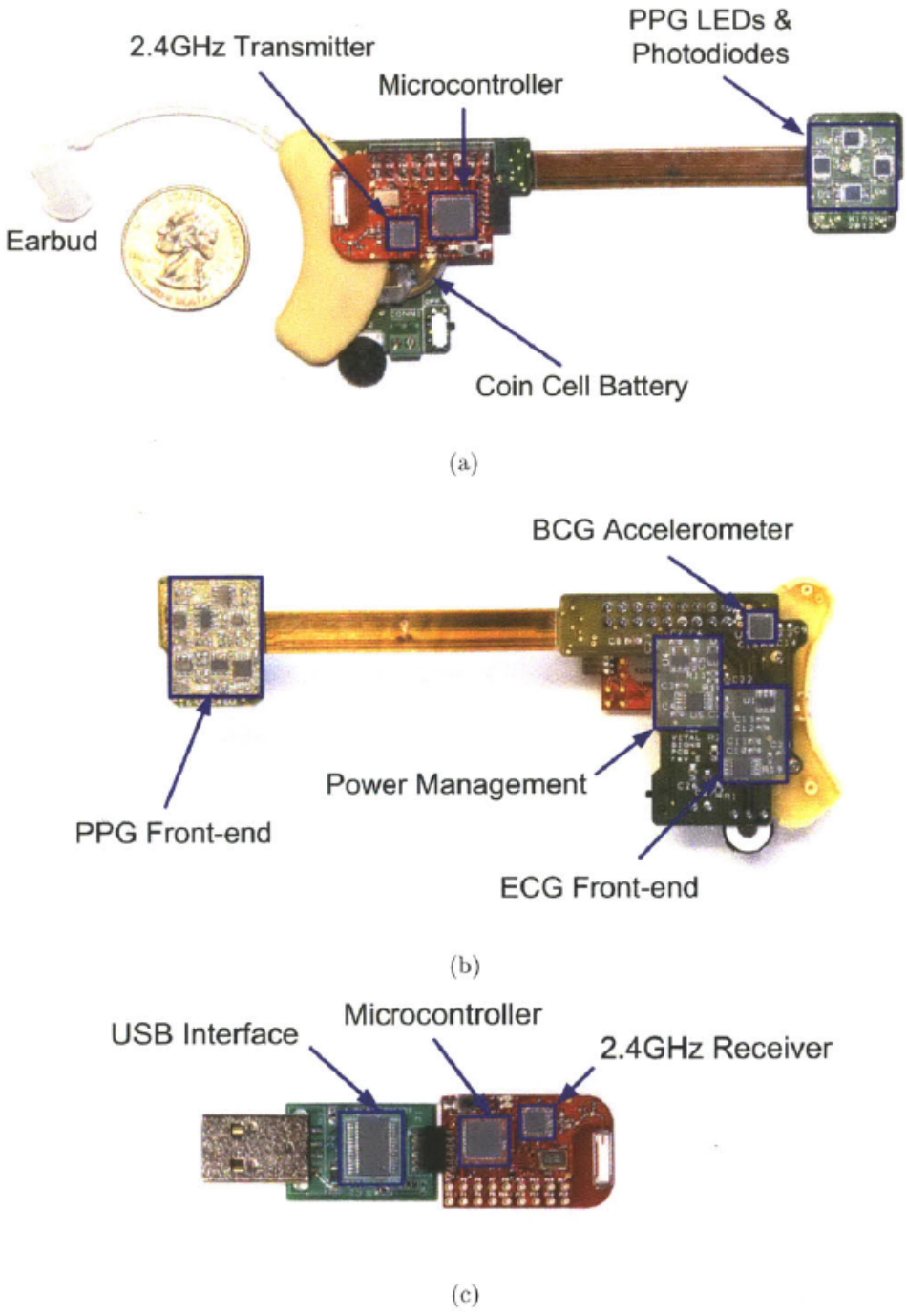

Figure 4-5: a) The wearable CHF monitor used in the clinical test, b) the device backside with the case removed, and c) the USB receiver (figure from [4]).

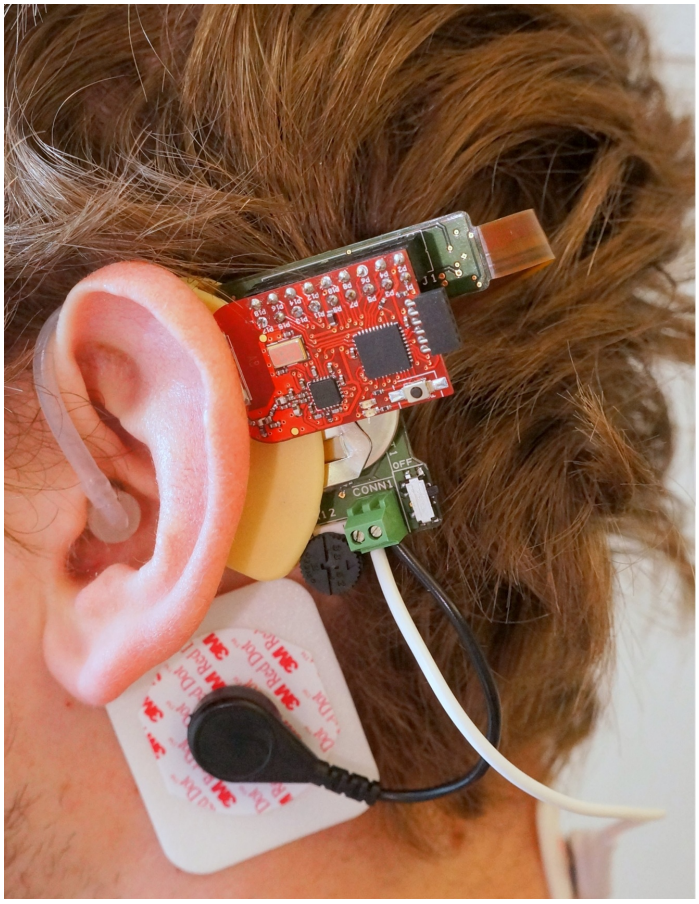

Figure 4-6: The clinical prototype being worn at the ear.

feedback, and the transmission of packetized data to the radio. The MSP430 firmware on the USB receiver unpacketizes the received data and sends it to the FT232RL, which in turn sends the data to the computer. The firmware is written in C in Code Composer Studio v4. Figure 4-7 is a flowchart of the firmware and Figure 4-8 is a flowchart of the PPG digital feedback algorithm.

4.1.3 Computer Software

The MATLAB script on the computer reads the received data from the virtual COM port, records the data into memory, and plots the data with real time filtering. Figure 4-9 shows a flowchart of the MATLAB script. Figure 4-10 shows a screenshot of the real time plots displayed by MATLAB. Plots of red PPG (red), infrared PPG (white), filtered PPG (red and white bold), ECG (blue), filtered ECG (blue bold), and tri-axial accelerations (green) are displayed simultaneously for immediate feedback during the clinical test.

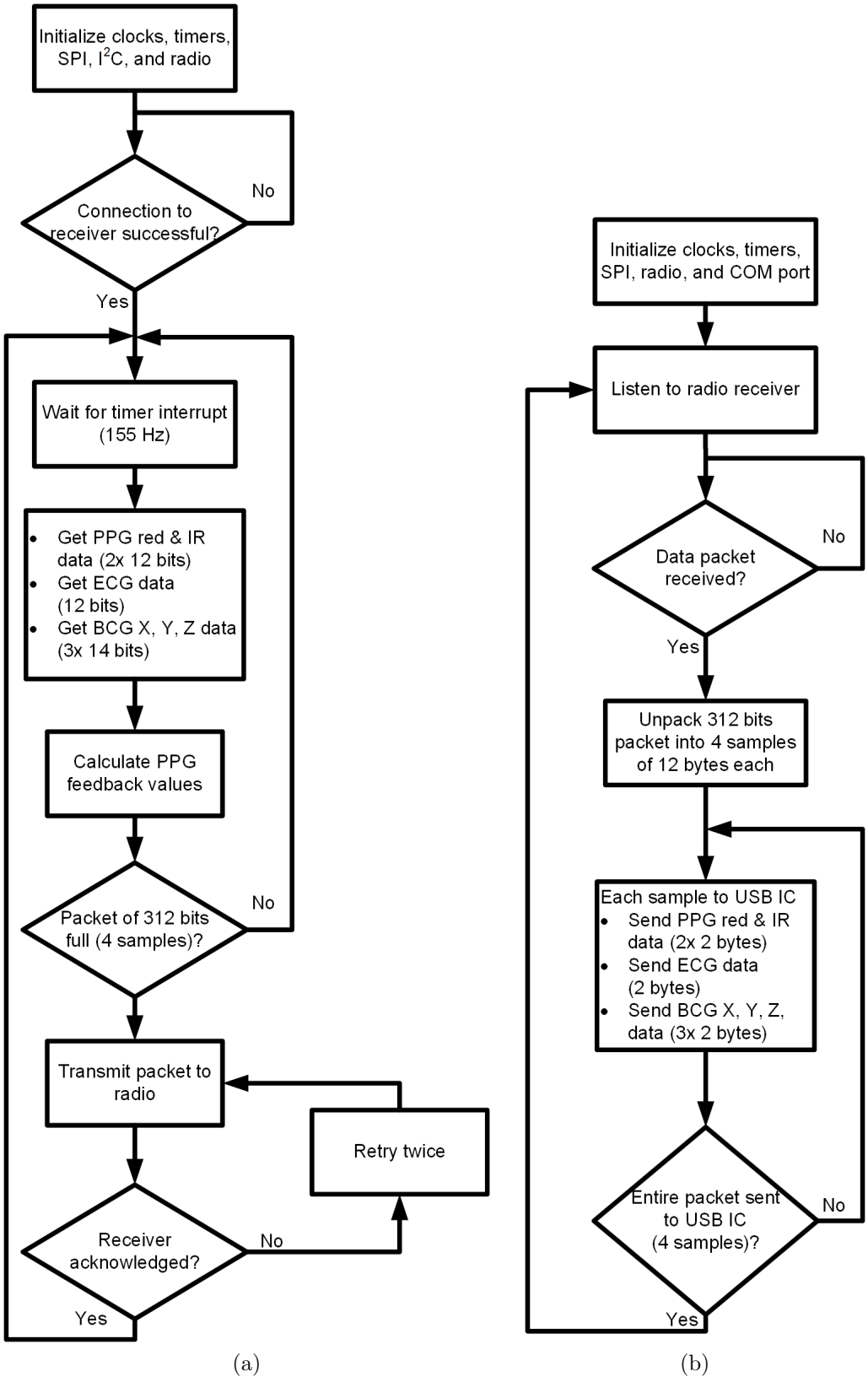

Figure 4-7: Firmware flowcharts of a) the wearable CHF monitor and b) the USB receiver.

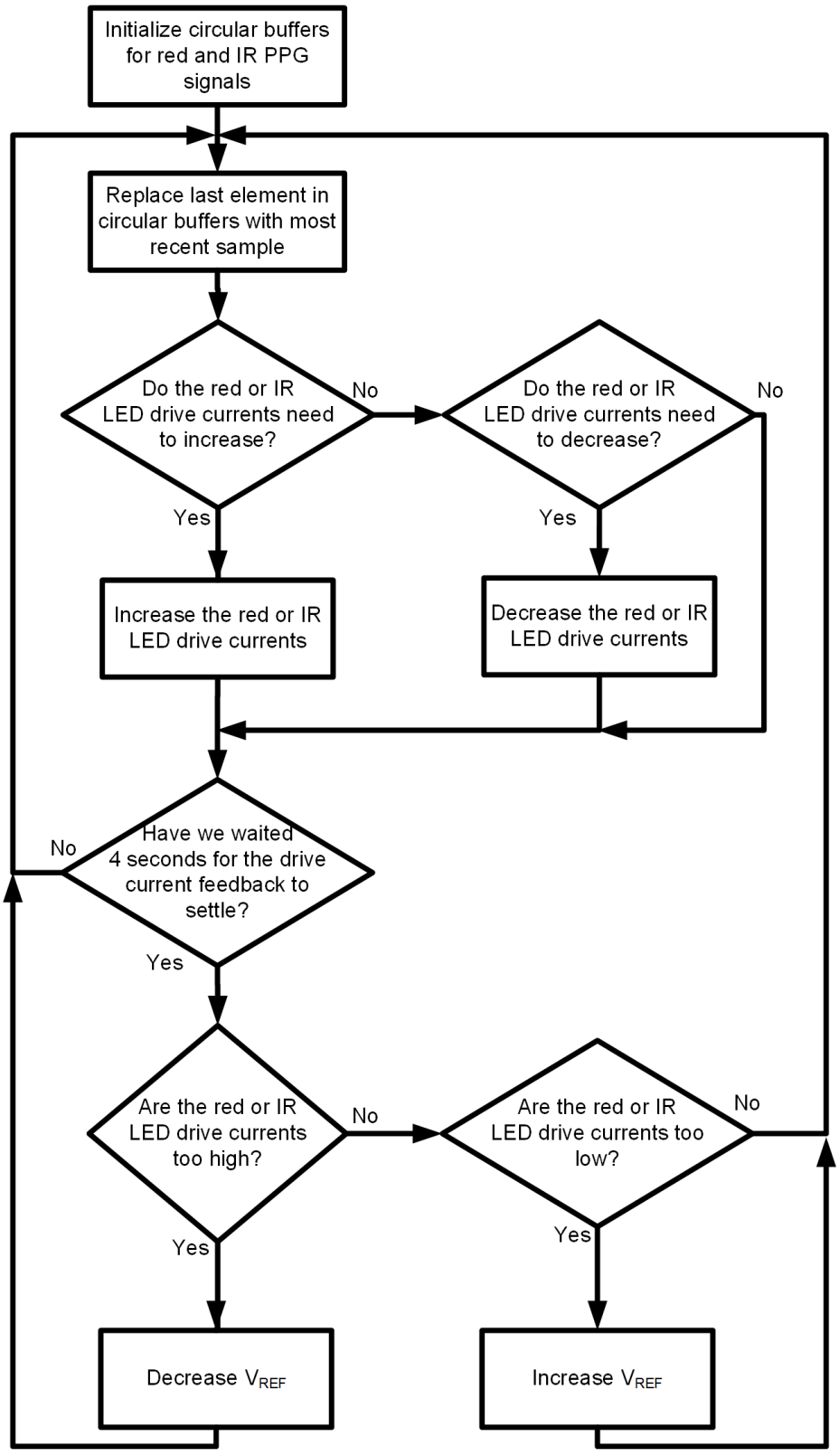

Figure 4-8: Firmware flowchart of the PPG digital feedback algorithm.

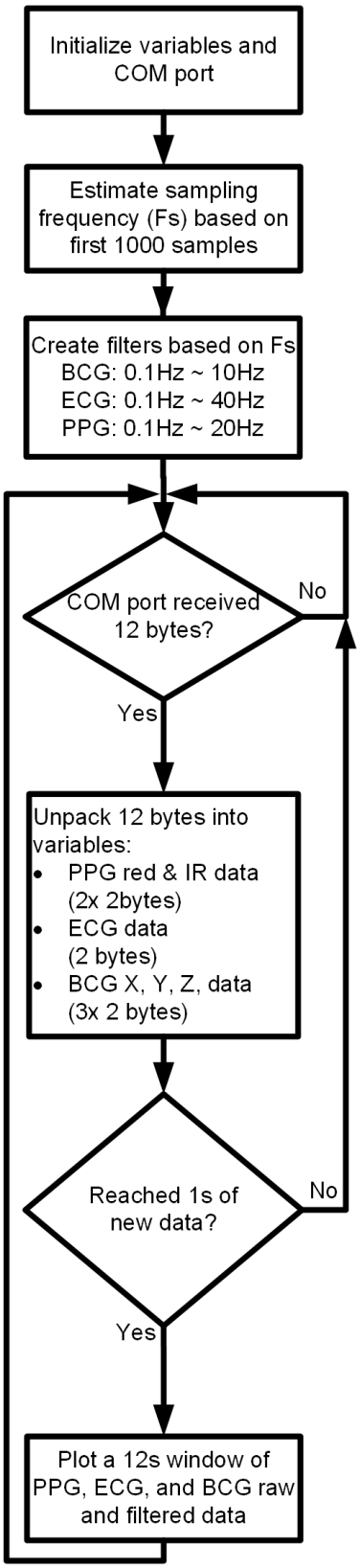

Figure 4-9: The MATLAB script flowchart.

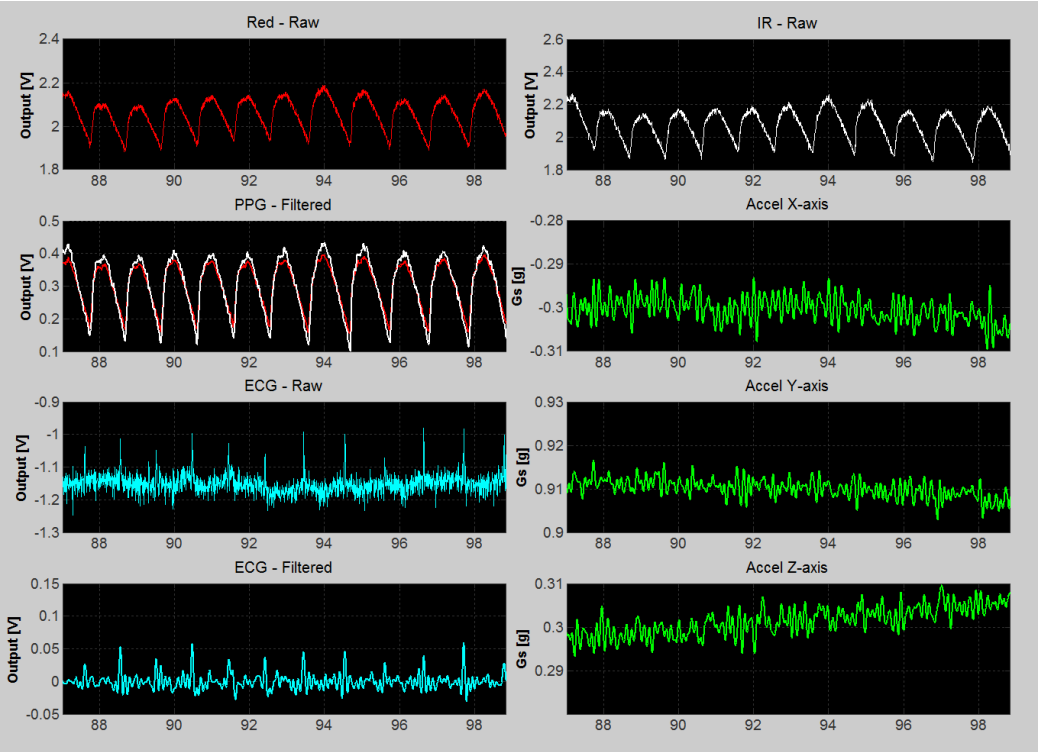

Figure 4-10: A screenshot of the MATLAB real time plotter.

4.2 Clinical Test Design

The goal of the clinical test is to alter the subject's blood pressure through non-invasive hemodynamic maneuvers. The first maneuver is the sit-to-stand maneuver, where the subject is sitting in a chair, and then abruptly stands up. The second maneuver is the head-up tilt, where the subject lies facing up on a motorized tilt table that is tilted between horizontal and 75^o vertical. The third maneuver is the Valsalva maneuver, which is a breath-hold exercise where the subject tries to forcibly exhale against a closed airway. Finally, a cold-pressor maneuver, where a subject places their hand in a bucket of ice-water was also performed on two subjects.

The test begins with consenting the subject and then completing a health questionnaire to ensure that the subject has no previous cardiovascular conditions. Then, reference measurement equipment is connected to the subject. The equipment is shown in Figure 4-11 and includes the Criticare 504-US chest ECG and finger pulse oximeter, the Finapres Portapres for continuous blood pressure, and the Sonosite BioZ Dx impedance cardiography (ICG) machine for continuous PEP and SV. The

ECG, PPG, and Portapres are recorded on an Agilent DSO6104A oscilloscope sampling at $500Hz$ in high resolution acquisition mode where the oscilloscope internally oversamples to achieve greater resolution. The ICG data is internally recorded on the BioZ device.

The Criticare unit measures the chest ECG in a modified Lead II configuration with one electrode placed on the left chest (left mid-clavicular and sixth intercostal), and the second electrode placed on the right chest (right mid-clavicular and first intercostal). The ground ECG electrode is placed right mid-clavicular and sixth intercostal. The Criticare unit also measures transmission PPG on the left index finger. The Portapres unit obtains continuous blood pressure through peripheral pressure detected at the left middle or ring finger using the volume clamp method [53]. The ICG machine obtains PEP by detecting the delay between the ECG's Q-wave and the ICG's B-wave. The ICG machine also calculates SV based on SV's dependence on PEP and left ventricular ejection time (LVET) $\frac{PEP}{LVET}$ [54]. Two ICG electrodes are placed on each side of the torso (midaxillary and sixth intercostal), and two ICG electrodes are placed on each side of the neck along the midaxillary. Lastly, the wearable CHF monitor is attached onto the subject with the PPG sensor placed on the mastoid area above Reid's line, one ECG electrode placed below the mastoid, and one ECG electrode placed on the upper middle neck.

The test protocol is summarized below:

1. Subject consent
2. Nurse assessment
3. Administer and review health questionnaire
4. Setup equipment and device on subject
5. Sit stand maneuver (subjects 7 - 13)
    - 5.1 Portapres calibration and cuffed blood pressure (automatic oscillometric monitor at arm) measurement
    - 5.2 Sit (2 min) to stand (2 min)
    - 5.3 Portapres calibration and cuffed blood pressure measurement

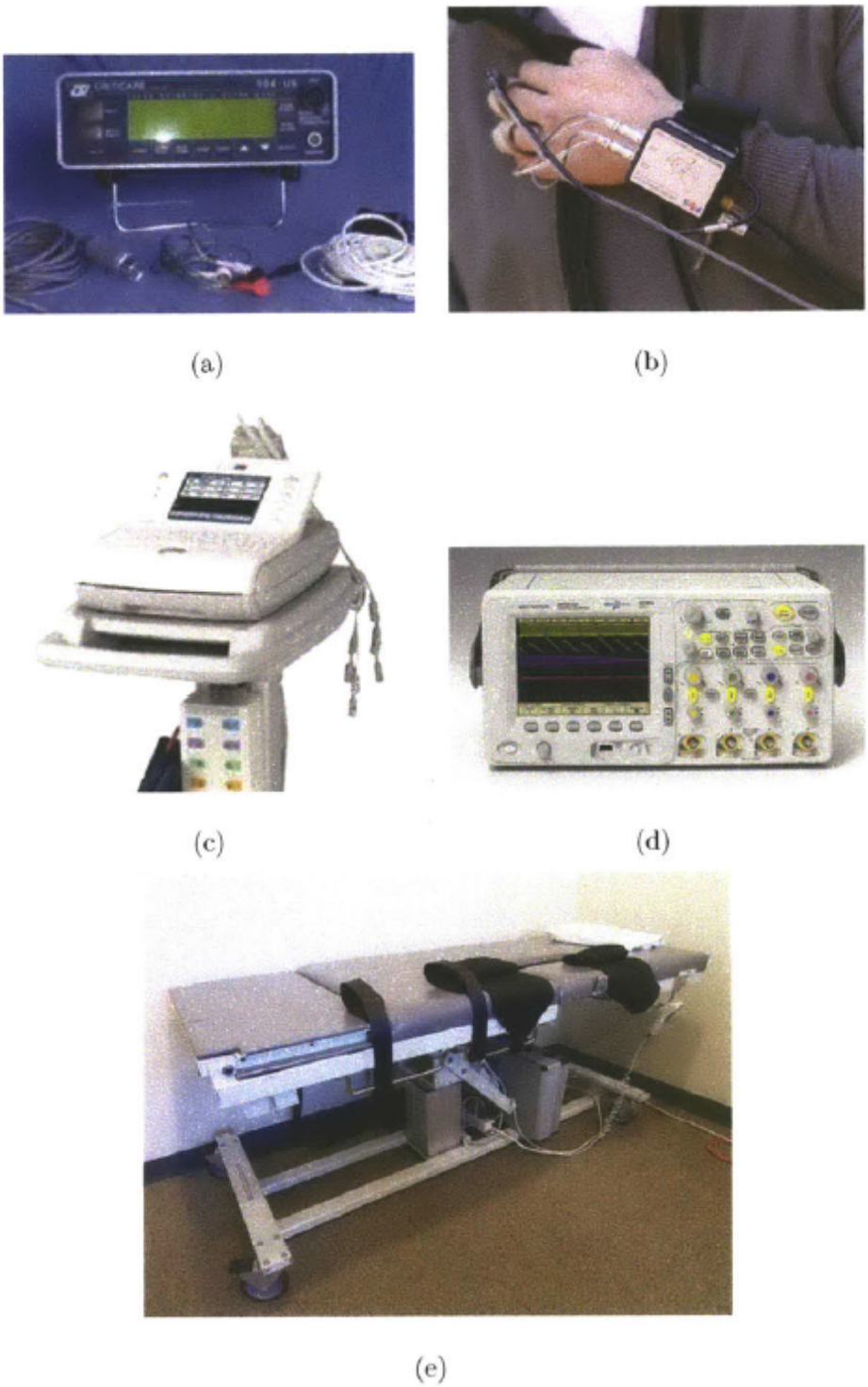

Figure 4-11: The measurement equipment: a) the Criticare 504-US (with transducers), b) the Finapres Portapres, c) the Sonosite BioZ Dx ICG, d) the Agilent DSO6104A, and e) the motorized tilt table.

5.4 Stand (2 min) to sit (2 min)

5.5 Portapres calibration and cuffed blood pressure measurement

5.6 Sit (2 min) to stand (2 min)

6. Tilt maneuver (subjects 1 - 13)

6.1 Portapres calibration and cuffed blood pressure (automatic oscillometric monitor at arm) measurement

6.2 Supine (2 min) to tilted (2 min)

6.3 Portapres calibration and cuffed blood pressure measurement

6.4 Tilted (2 min) to supine (2 min)

6.5 Portapres calibration and cuffed blood pressure measurement

6.6 Supine (2 min) to tilted (2 min)

6.7 Portapres calibration and cuffed blood pressure measurement

6.8 Tilted (2 min) to supine (2 min)

7. Valsalva maneuver (subjects 1 - 13)

7.1 Portapres calibration and cuffed blood pressure measurement

7.2 Stand at rest (40 sec), Valsalva (20 sec), then stand at rest (40 sec)

7.3 Portapres calibration and cuffed blood pressure measurement

7.4 Stand at rest (40 sec), Valsalva (20 sec), then stand at rest (40 sec)

7.5 Portapres calibration and cuffed blood pressure measurement

7.6 Stand at rest (40 sec), Valsalva (20 sec), then stand at rest (40 sec)

8. Cold pressor maneuver (subjects 14 - 15)

8.1 Portapres calibration and cuffed blood pressure measurement

8.2 Sit at rest (3 min)

8.3 Insert right hand into ice-water bath (2 min)

8.4 Remove right hand from ice-water bath and sit at rest (3 min)

9. Exit cuffed blood pressure measurement

10. Exit questionnaire

The setup time and test duration are each approximately one hour. 15 healthy subjects are tested consisting of 12 male subjects and three female subjects. The subjects varied from 25 to 63 years old, 1.55m to 1.93m in height and 49.9kg to

103kg in mass. The clinical test is conducted at the MIT Catalyst Clinical Research Center (CRC) under IRB approval #1104004449, CRC protocol #615, and grant #UL1RR025758.

4.3 Clinical Test Results

4.3.1 Head PPG Measurements

Data for the head PPG signals are summarized in Table 4.1 where R_{avg} and IR_{avg} are the mean peak-to-peak amplitudes in mV of the red and IR head PPG signals. R_{std} and IR_{std} are the standard deviations of the peak-to-peak amplitudes, and $\#R$ and $\#IR$ are the number of beats per PPG wavelength for each test subject. The data was generated automatically in MATLAB by using the peak detection algorithm described in [4] to find each individual R-wave, then the PPG signals were individually windowed to find the local minima and maxima. Peak-to-peak amplitudes were considered valid if they were smaller than 300mV. Values larger than 300mV were due to motion artifact and removed from the data analysis. Figure 4-12 shows red and IR PPG measurements from subjects H001 - H013 in the standing posture (H014 and H015 were always sitting). PPG waveforms from all subjects are shown in order to give the reader a sense of morphological variation among subjects.

Several observations can be made from Table 4.1 and Figure 4-12. First, the morphology and amplitude of the PPG waveforms are highly variable among subjects. Some subjects, such as H005 possess a Dicrotic Notch, while others do not. Pulse amplitudes varied from $\pm 10mV$ to $\pm 100mV$. Noisier waveforms, such as those seen in the IR PPG of subject H004 may be due to hair blocking the IR LED, thus reducing the amount of signal emitted into the body. However, each subject had a discernible pulsatile component to their PPG corresponding to the cardiac cycle.

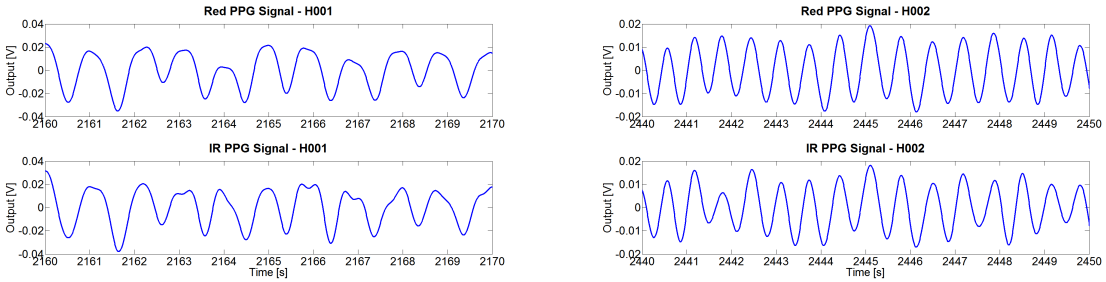

(a) (b)

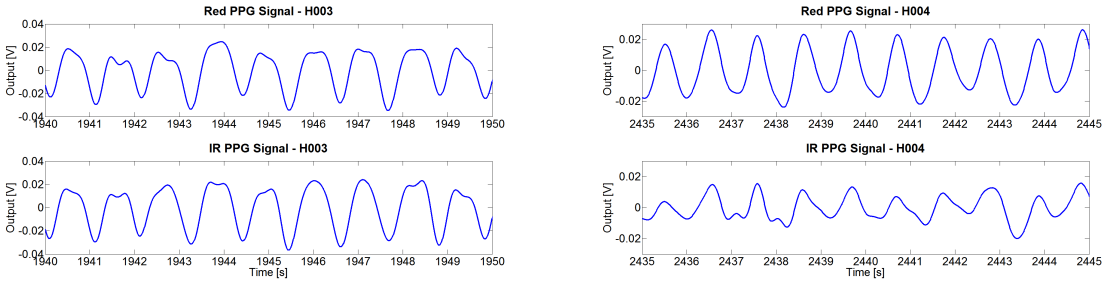

(c) (d)

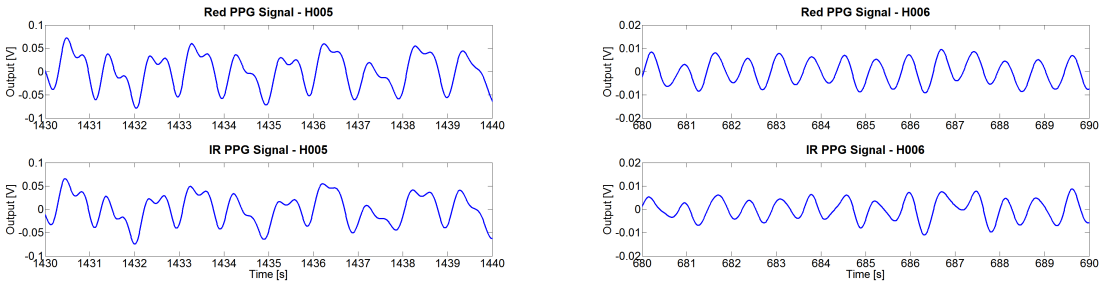

(e) (f)

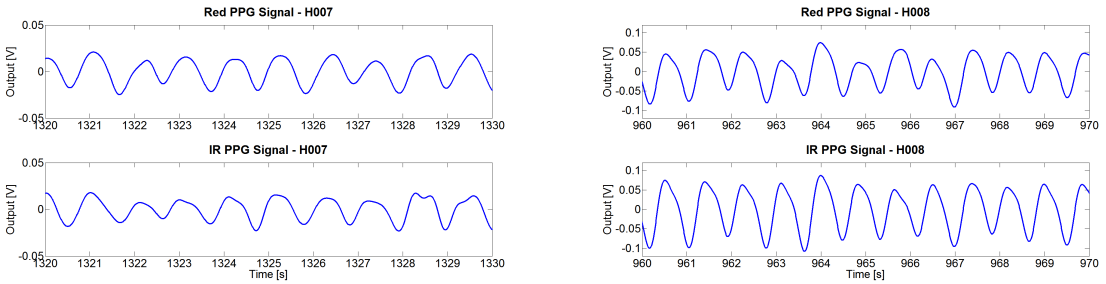

(g) (h)

Figure 4-12

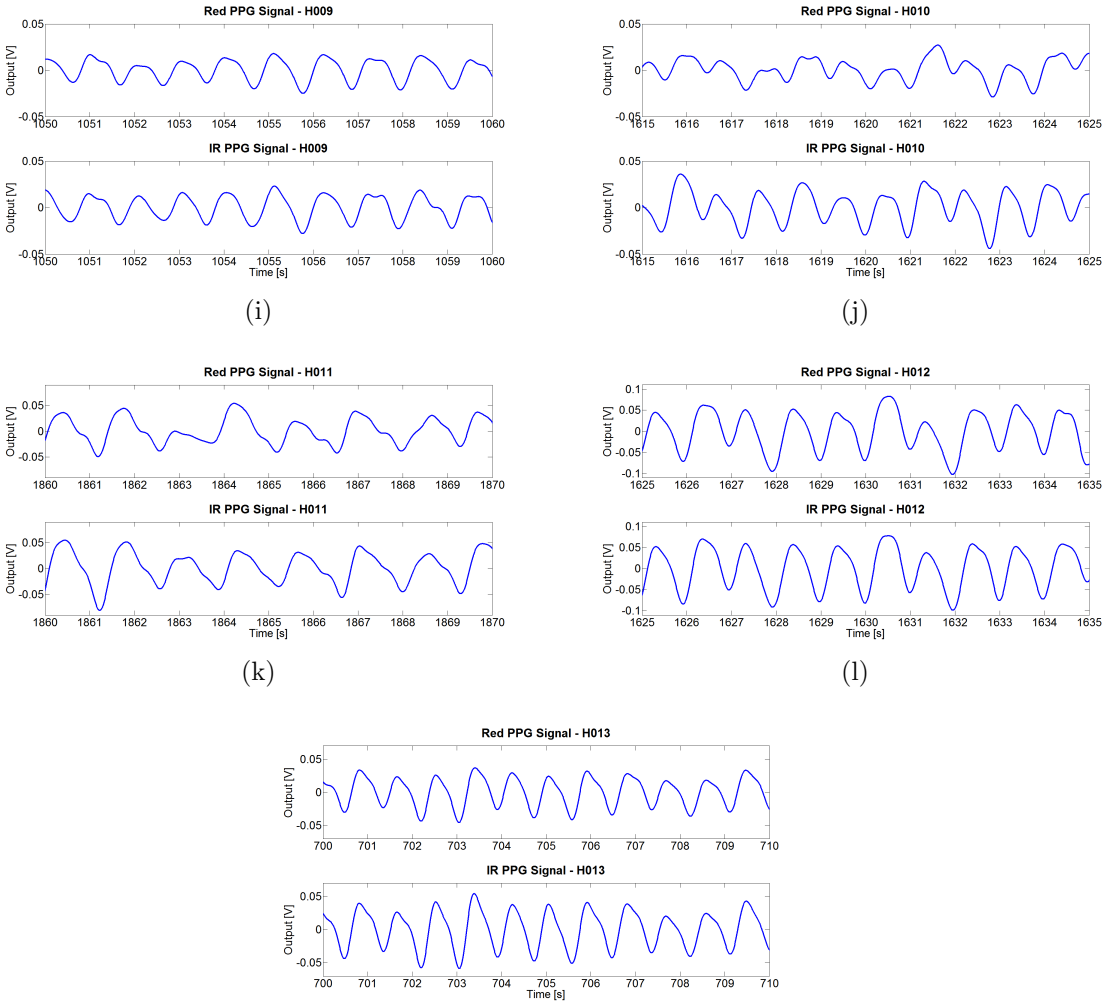

Figure 4-12: Head PPG signals in the standing posture from a) H001 to m) H013.

Subj.	Age	Height [m]	Mass [kg]	R_{avg} [mV]	IR_{avg} [mV]	R_{std} [mV]	IR_{std} [mV]	#R beats	#IR beats
H001	27	1.78	67.1	76.7	78.1	53.9	53.1	3661	3684
H002	27	1.80	74.8	24.8	27.6	33.1	31.6	3612	3629
H003	28	1.83	81.6	39.6	41.5	39.4	39.3	3394	3531
H004	31	1.70	70.3	32.4	26.6	43.1	40.3	3335	3333
H005	26	1.83	72.6	59.8	62.0	45.3	50.1	2555	2534
H006	40	1.93	103.0	42.9	33.7	46.8	38.3	4072	4122
H007	49	1.78	78.0	50.4	35.0	53.0	35.1	3074	3191
H008	53	1.75	85.3	113.0	119.9	64.1	61.7	4387	4450
H009	60	1.83	78.0	41.9	42.2	39.5	32.1	2394	2406
H010	33	1.55	49.9	44.3	47.8	54.2	47.7	4863	5047
H011	25	1.70	66.7	69.9	67.3	58.3	60.2	2860	2748
H012	54	1.83	83.9	87.3	94.6	73.9	70.5	5041	5308
H013	63	1.65	61.7	68.7	71.1	48.3	45.5	3632	4039
H014	29	1.83	77.0	33	35.8	38.9	27.0	679	726
H015	28	1.83	77.1	20.4	23.9	27.9	28.1	576	576
Mean	38.2	1.77	77.13	53.67	53.81	47.98	44.04	3209	3288
Stdev	13.7	0.093	9.75	25.47	27.9	12.02	13.09	1292	1354

Table 4.1: Summary of Head PPG and Subject Parameters

4.3.2 Estimating Blood Pressure at the Head

Comparing Head PTT Measurements to Blood Pressure

Two maneuvers chosen to compare $ln(\frac{1}{PTT})$ to BP in the carotid artery are the sit-to-stand maneuver, and the Valsalva maneuver. Both maneuvers transiently change blood pressure, with responses as short as 2 seconds (stage III of Valsalva), to as long as 20 seconds (sit-to-stand maneuver). Transient changes were chosen because the body regulates blood pressure very tightly, especially in the head. Long-term changes in the head are difficult to obtain, and may be unsafe.

The sit-to-stand maneuver is highly repeatable, and has a well known response to mean arterial pressure (MAP) and cerebral blood flow velocity (CBFV). The sit-to-stand repeatability allows for a more thorough analysis, not only for intra-subject maneuvers, but also for inter-subject comparison. Conversely, the Valsalva maneuver morphology is highly variable, even comparing multiple maneuvers over one subject. Although there is some information that can be obtained from measuring the $ln(\frac{1}{PTT})$

response during Valsalva, the usefulness of this data is limited since it is not repeatable.

Continuous, non-invasive measurements of blood pressure in the carotid artery are difficult to obtain. Due to the lack of available continuous blood pressure measurements in the carotid artery for subjects performing sit-to-stand, and Valsalva maneuvers, the following analysis shows how to relate $ln(\frac{1}{PTT})$ from the wearable CHF monitor to blood pressure by using cerebral blood flow velocity ($CBFV$).

$CBFV$ is related to pressure through the relationship:

$$F = V \times A = \frac{P}{R} \tag{4.2}$$

where F is blood flow ($\frac{m^3}{s}$), V is blood flow velocity ($\frac{m}{s}$), A is cross sectional area of the vessel (m^2), P is blood pressure ($mmHg$), and R is vessel resistance ($\frac{mmHg \cdot s}{m^3}$). Concurrently:

$$PWV = \sqrt{\frac{E_{inc}h}{2r\rho}} = \frac{\Delta X}{PTT} \tag{4.3}$$

where PWV is pulse wave velocity ($\frac{m}{s}$), E_{inc} is Young's modulus of the vessel ($\frac{kg}{m \cdot s^2}$), h is the vessel wall thickness (m), r is the vessel inner radius (m), ρ is the density of blood ($\frac{kg}{m^3}$), ΔX is the length of the vessel (m), and PTT is the pulse transit time (s). Substituting the area of a circle (πr^2) for A and equation 3.10 for R into equation 4.2, and solving for V yields:

$$V = \frac{Pr^2}{8\Delta X \eta} \tag{4.4}$$

where ΔX is the length of the vessel and η is the blood viscosity ($mmHg \cdot s$). Similarly, substituting equation 3.4 for E_{inc}, assuming unit vessel length, and solving equation 4.3 for $ln(\frac{1}{PTT})$ yields:

$$ln(\frac{1}{PTT}) = \frac{\alpha P}{2} ln(\frac{E_0 h}{2r\rho}) \tag{4.5}$$

where E_0 is the value of the Young's modulus when mean blood pressure is 0, α is a fitting parameter with units $\frac{1}{mmHg}$, and P is pressure. From equations 4.4 and 4.5, it

can be shown that:

$$V \propto P \quad and \quad V \propto r^2 \tag{4.6}$$

while:

$$ln(\frac{1}{PTT}) \propto P \quad and \quad ln(\frac{1}{PTT}) \propto ln(\frac{1}{r}) \tag{4.7}$$

Therefore, if the trend of $CBFV$ from previous studies is directly correlated to the trend of $ln(\frac{1}{PTT})$ during the same type of hemodynamic maneuver, then theoretically the blood pressure in the carotid artery is dominating the transient changes. However, if $CBFV$ and $ln(\frac{1}{PTT})$ are inversely correlated, then the change in vessel radius is dominating. If there is no statistical correlation, then neither blood pressure, nor vessel radius is dominating. Data in the following subsections show $ln(\frac{1}{PTT})$ from the wearable CHF monitor compared to previous studies obtaining mean cerebral blood flow velocity ($\overline{CBFV}$) during the same type of hemodynamic maneuvers. Finapres MAP is also plotted as a reference measurement for comparing measurements in the carotid to pressure changes occurring below the neck.

To obtain the $ln(\frac{1}{PTT})$ data points, the R-peaks were annotated using the peak detection algorithm described in [4] in MATLAB. The PPG signals were then windowed over the next $200ms$ from the R-peak to find the trough of the waveform, and then windowed again from the trough over the next half R-R interval to find the peak of the PPG. The edge of the PPG was determined to be the mid-point between the trough and the peak. The annotations from MATLAB were then imported into Physionet's WAVE to manually ensure that they were correct. Once the annotations were checked, they were re-imported back into MATLAB to calculate the different timing intervals. Each of the intervals was averaged over 5 beats to smooth the trend lines.

Sit-to-Stand Maneuvers

Figure 4-13 shows a comparison of $ln(\frac{1}{PTT})$ measured from the wearable CHF monitor for a sit-to-stand maneuver, and previous work measuring mean cerebral blood flow velocity ($\overline{CBFV}$) during the same type of maneuver [55]. MAP from a Finapres is shown as a reference measurement in both Figure 4-13a and 4-13b. In both datasets, once the subjects stand up, the MAP dips, bottoming out approximately 10 seconds after standing, and returning to baseline approximately 20 seconds after the start of the maneuver. The $ln(\frac{1}{PTT})$ and $\overline{CBFV}$ also have matching characteristics as a dip followed by an increase in pressure compared to baseline approximately 10 seconds after the maneuver began. Both $ln(\frac{1}{PTT})$ and $\overline{CBFV}$ return to baseline approximately 20 seconds after the maneuver began. Figure 4-14 is a scatter plot of the normalized and averaged $ln(\frac{1}{PTT})$ sit-to-stand data for subjects H007 - H013 versus the normalized $\overline{CBFV}$ data from [55]. The data are directly correlated with a correlation coefficient of 0.545 that is statistically significant ($P < 0.05$).

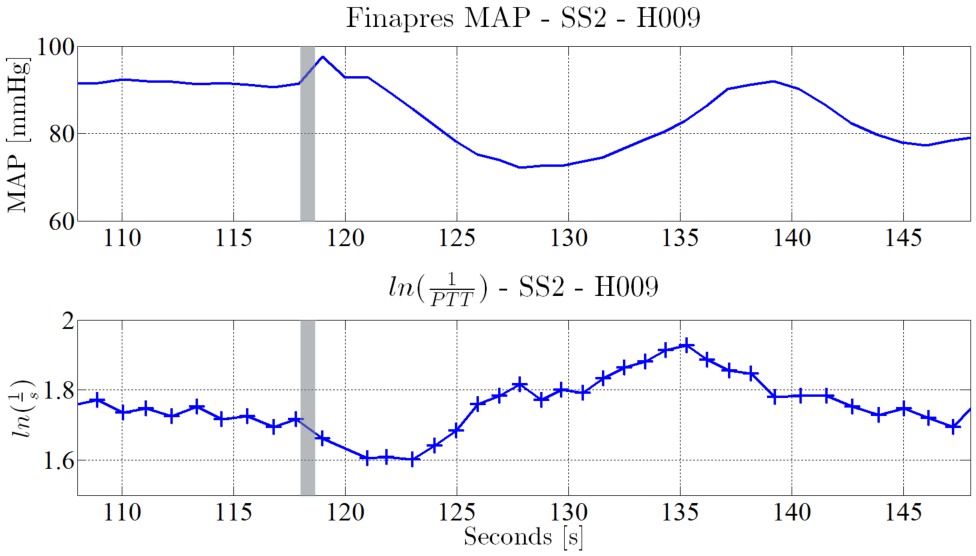

(a)

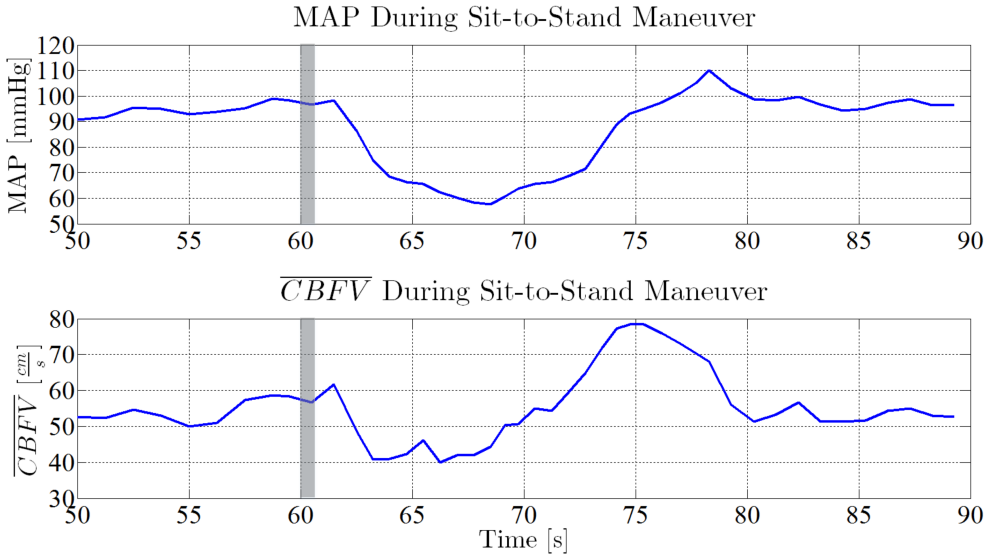

(b)

Figure 4-13: a) Top: Mean Arterial pressure from a Finapres and Bottom: $ln(\frac{1}{PTT})$ measured from the wearable CHF monitor during a sit-to-stand maneuver from subject H009. b) Top: Mean arterial pressure from a Finapres, and Bottom: $\overline{CBFV}$ measured by [55] during a sit-to-stand maneuver. Gray lines indicate where the subjects stood up.

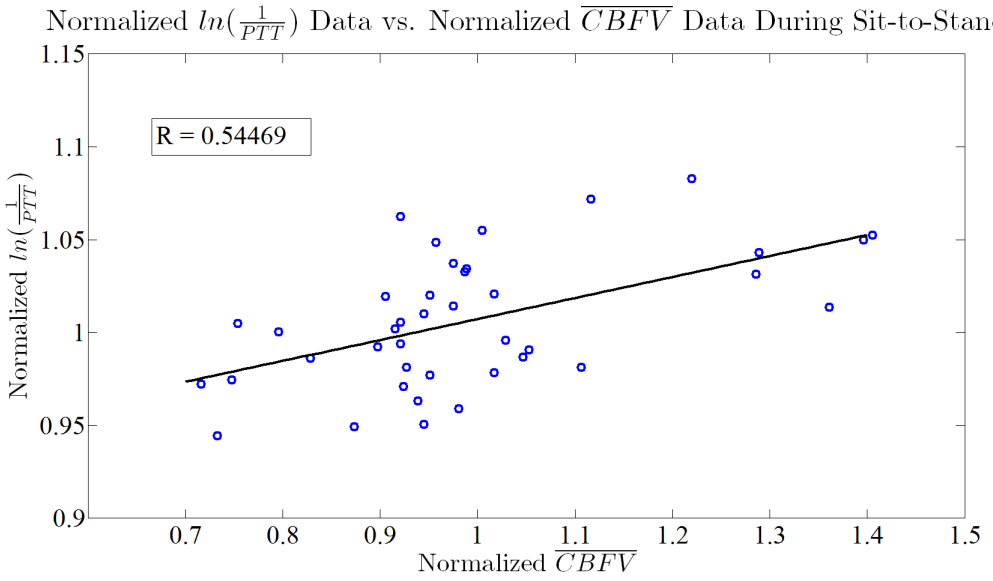

Figure 4-14: Normalized and averaged $ln(\frac{1}{PTT})$ data from subjects H007-H013 for sit-to-stand maneuvers vs. normalized $\overline{CBFV}$ from [55]. The data are directly correlated with a correlation coefficient of 0.545 which is statistically significant ($P < 0.05$).

Figure 4-15 shows averaged and normalized MAP, $ln(\frac{1}{PTT})$, $ln(\frac{1}{PAT})$, and PEP for all sit-to-stand maneuvers. To average data points from different maneuvers, each plot was windowed from 20 seconds before, to 40 seconds after the subject stood up. Each maneuver was normalized over this one minute range and data points were placed in one second wide bins, and then averaged.

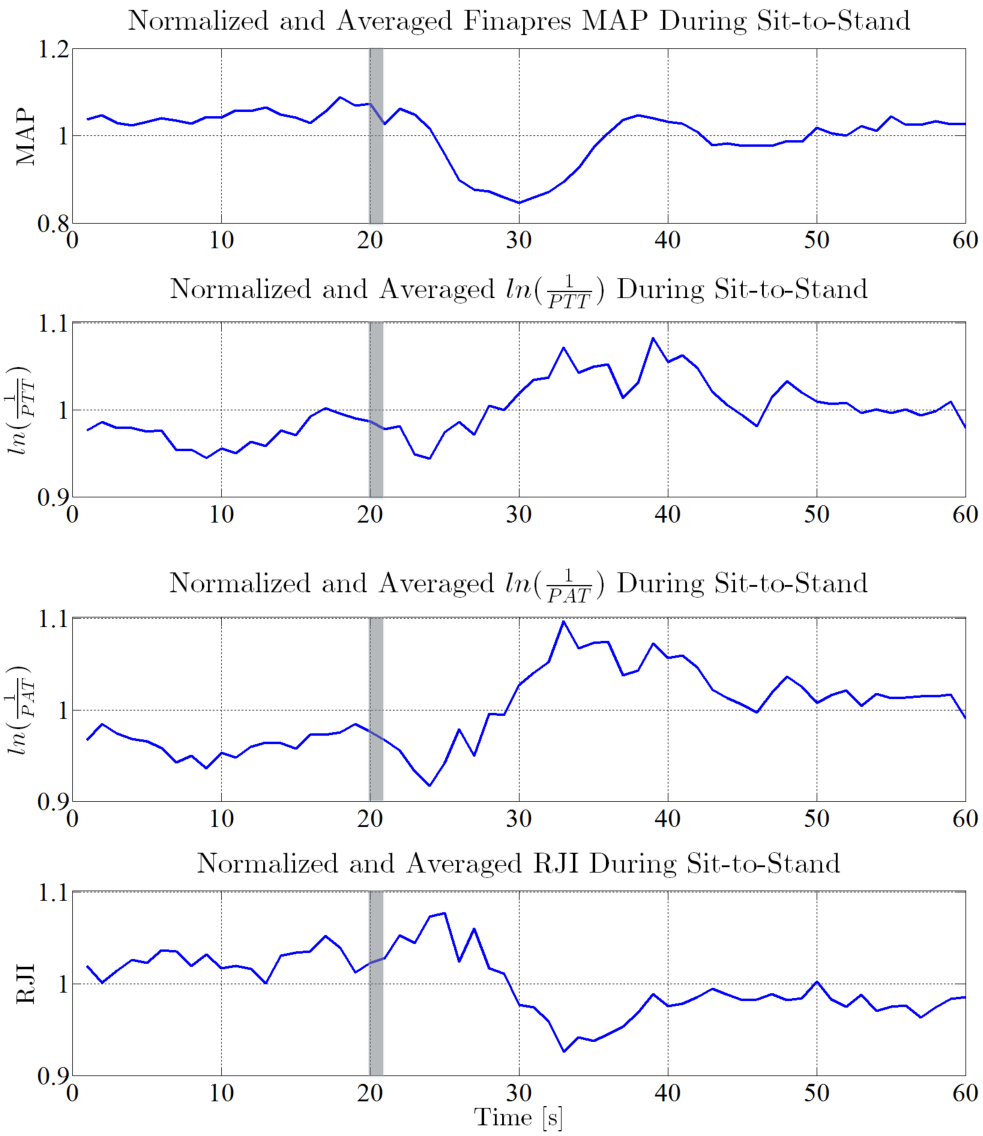

Figure 4-15: Normalized and averaged data from subjects H007-H013 for sit-to-stand maneuvers. Top: Finapres MAP, second: $ln(\frac{1}{PTT})$, third: $ln(\frac{1}{PAT})$, and bottom: RJI. Gray lines indicate when the subjects stood up.

Figure 4-16 shows the normalized and averaged sit-to-stand data with error bars. During the maneuver, the RJ interval increases transiently, due to the reduced venous return to the right atrium. As the body compensates for gravity, the normalized RJI drops to slightly below 1, indicating that one of the body's responses for maintaining blood pressure while standing is a slight increase in contractility. This change in RJI would cause MAP estimates using PAT to error slightly higher.

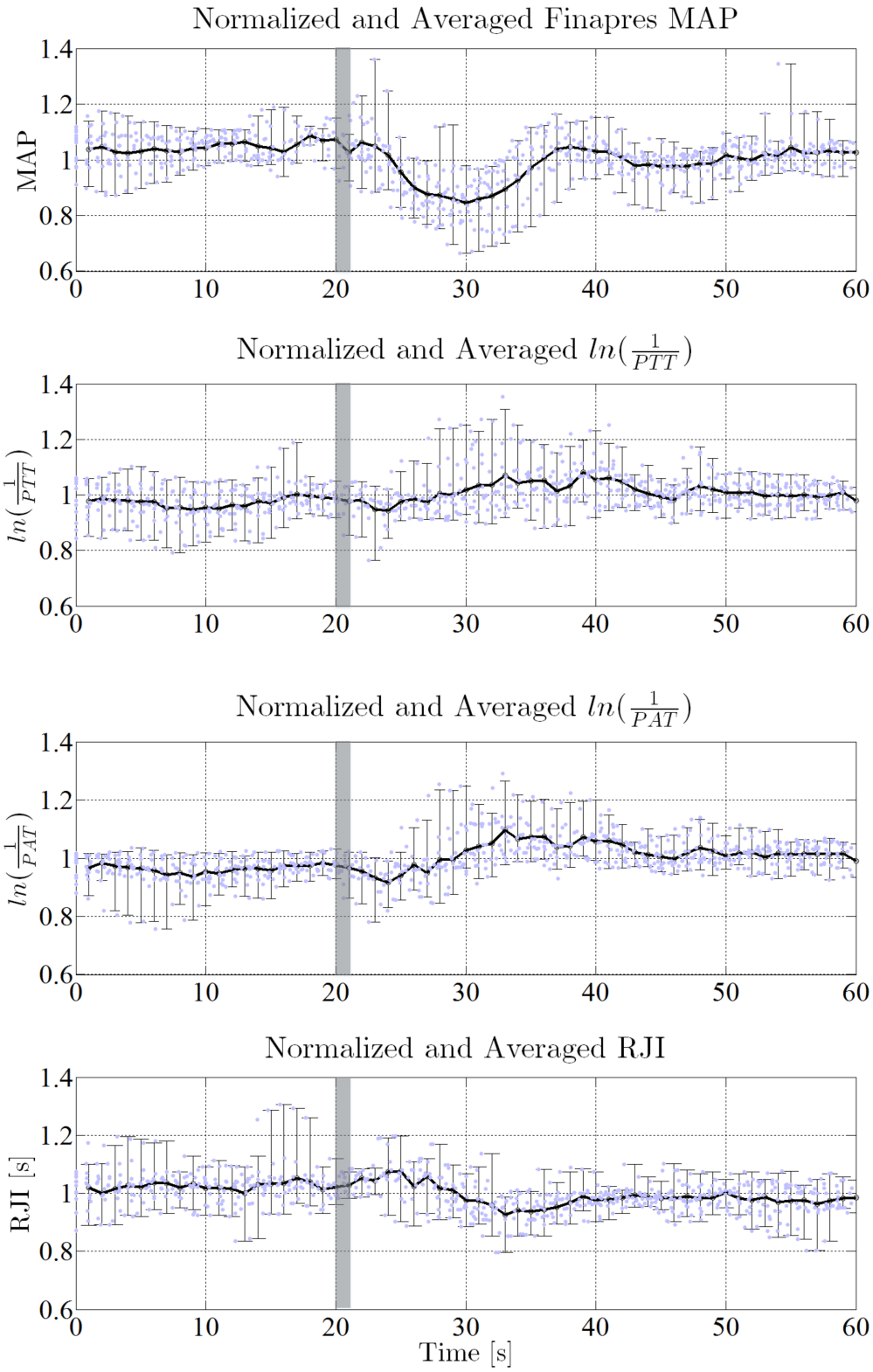

Figure 4-16: Normalized and averaged data from subjects H007-H013 during sit-to-stand maneuvers with error bars. Gray lines indicate when the subjects stood up.

Valsalva Maneuvers

Figure 4-17 shows a comparison of $ln(\frac{1}{PTT})$ measured from the wearable CHF monitor for a Valsalva maneuver and previous work measuring $\overline{CBFV}$ during the same type of maneuver, with MAP from a Finapres as a reference measurement [56]. Due to the fast transients of the Valsalva maneuver, all four stages are present in both the $ln(\frac{1}{PTT})$ and $\overline{CBFV}$ [56] [57]. The MAP shows very dramatic and fast transitions between the stages, where the pressure changes by approximately $70-100\%$ between minimum and maximum points. Conversely, for $ln(\frac{1}{PTT})$ and $\overline{CBFV}$, the difference between minimum and maximum points is only $30-50\%$, which suggests that even with fast hemodynamic transients, the change in blood pressure to the head is muted compared to the change to the rest of the body. The four stages of the Valsalva maneuver are as follows:

- Stage I of the Valsalva occurs as the subject initially bears down on their chest. The increased intrathoracic pressure increases cardiac output and blood pressure as blood is forced out of pulmonary circulation into the left atrium.

- Stage II is denoted by a drop in cardiac output, due to reduced venous return to the right atrium, followed by compensation of the body to increase vascular resistance and blood pressure.

- Stage III is the release of the intrathoracic pressure, which allows the pulmonary vessels and aorta to re-expand, causing a slight drop in cardiac output and blood pressure.

- Stage IV occurs as venous return increases, allowing cardiac output and blood pressure to return to normal. Usually the body overcompensates before hemodynamics return to their pre-Valsalva values.

Figure 4-18 shows representative data from Valsalva maneuvers during the clinical test. Once again, the top plot of each sub-figure is Finapres MAP, while the second, third, and bottom plots correspond to $ln(\frac{1}{PTT})$, $ln(\frac{1}{PAT})$, and RJI from the wearable

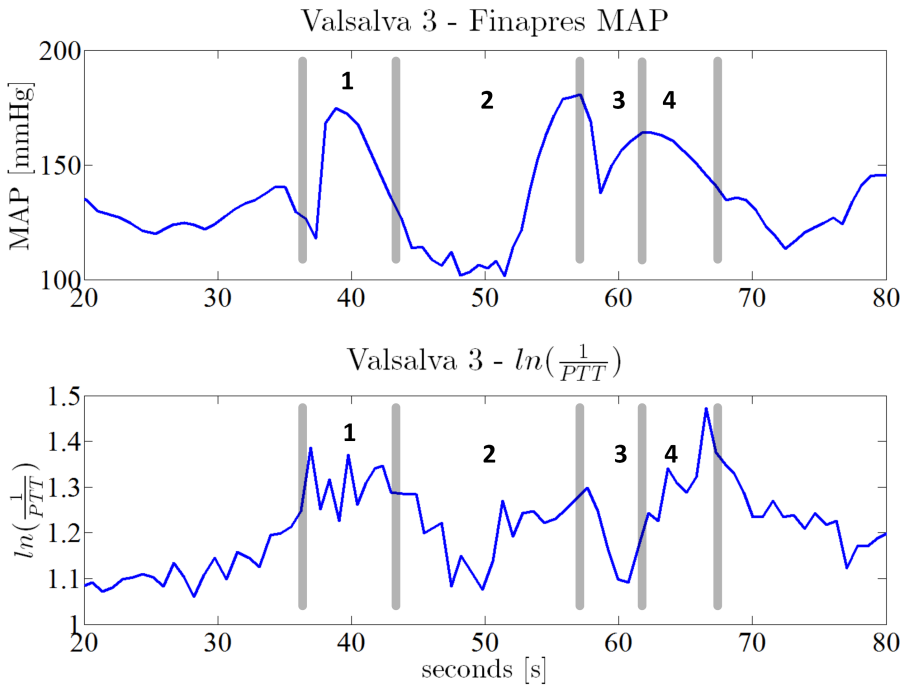

(a)

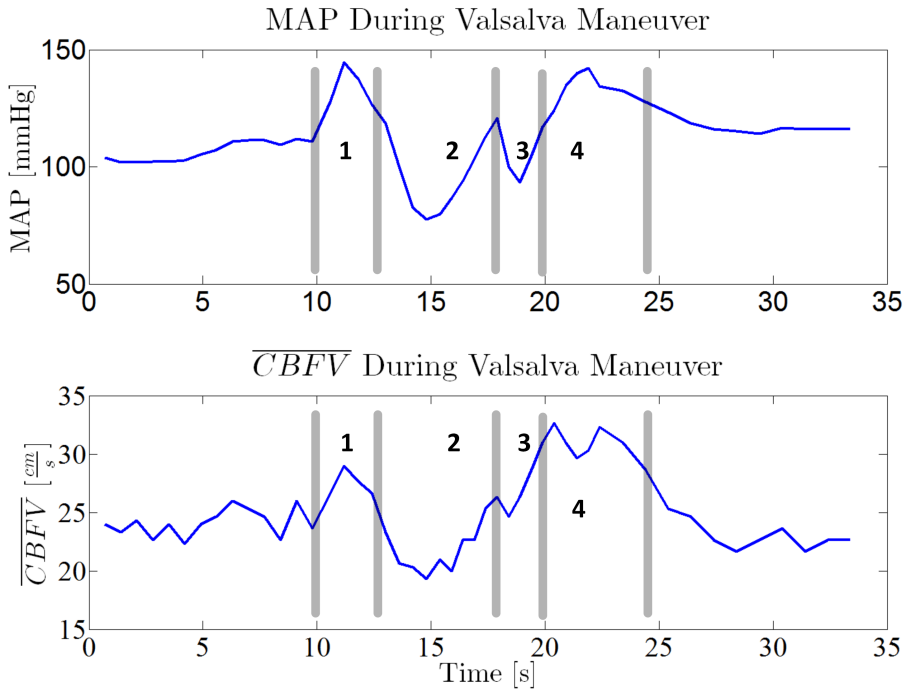

(b)

Figure 4-17: a) Top: Mean arterial pressure from a Finapres and Bottom: $ln(\frac{1}{PTT})$ measured from the wearable CHF monitor during a 20 second Valsalva maneuver from subject H006. b) Top: MAP from a Finapres, and Bottom: ($\overline{CBFV}$) from a 10 second Valsalva maneuver measured by [56]. $1-4$ denote stages I-IV of the Valsalva maneuver.

CHF monitor respectively. The large variation in the RJI causes errors in pressure estimation when using $ln(\frac{1}{PAT})$ instead of $ln(\frac{1}{PTT})$.

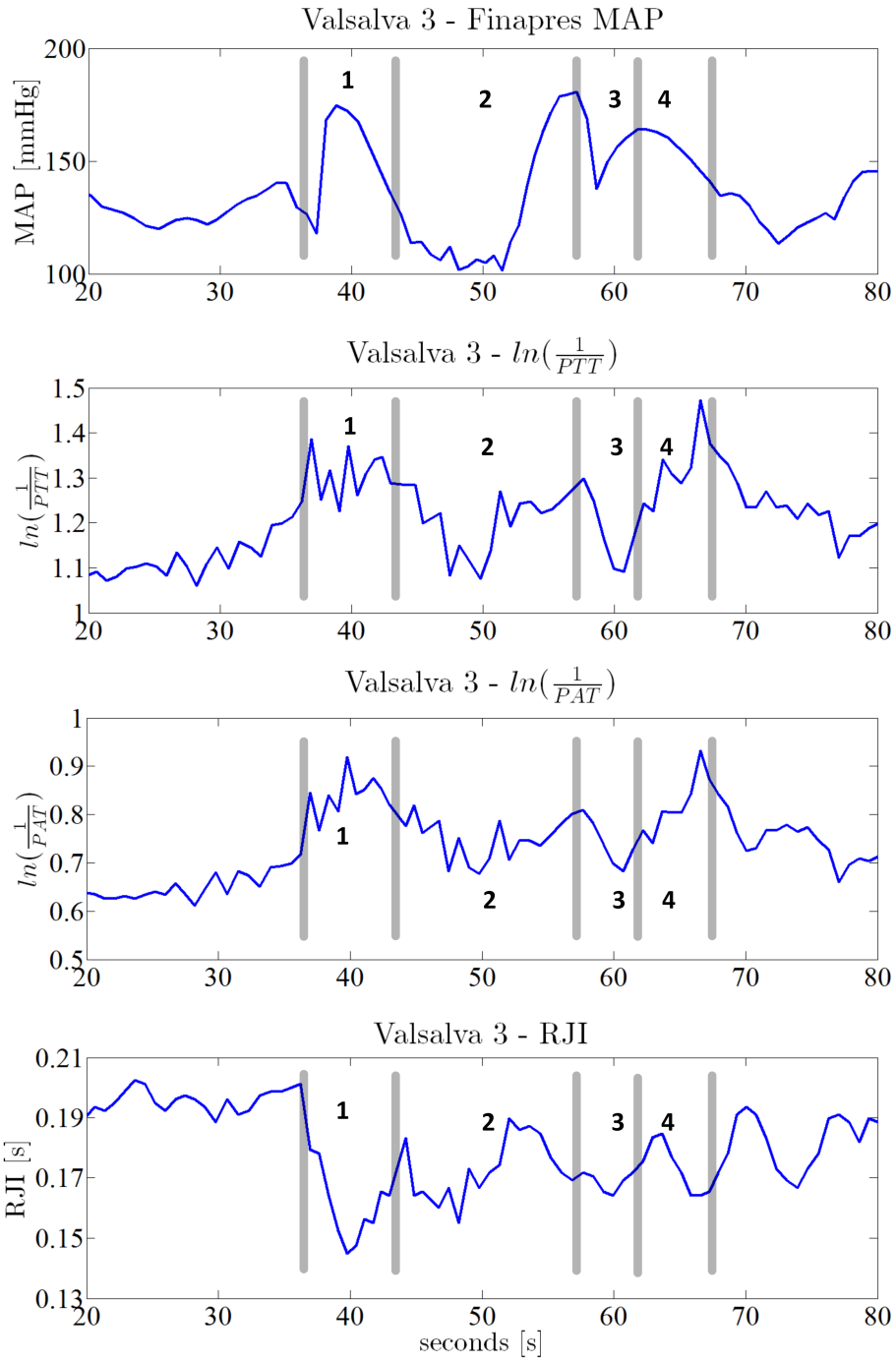

Figure 4-18: Representative Valsalva maneuver data from the clinical test. Top: Finapres MAP, second: $ln(\frac{1}{PTT})$, third: $ln(\frac{1}{PAT})$, and bottom: RJI. Data is from subject H006.

Interpretation of the Data

Theoretically, a direct correlation between $\overline{CBFV}$ and $ln(\frac{1}{PTT})$ trends indicate that a change in blood pressure is dominating. For the sit-to-stand maneuver, a direct correlation coefficient of $R = 0.545$ was obtained for $\overline{CBFV}$ between a normalized subject from [55] and the averaged and normalized $ln(\frac{1}{PTT})$ data from subjects H007 - H013. However, without a direct measurement of pressure in the carotid, the correlation of $ln(\frac{1}{PTT})$ to pressure cannot be calculated.

Analyzing the Valsalva data is more difficult. It's unrepeatable nature removes the ability to average $ln(\frac{1}{PTT})$ over several maneuvers, which makes statistical correlations all but impossible. Additionally, the morphological variations remove the ability to directly compare $ln(\frac{1}{PTT})$ from subjects H001 - H013 and $\overline{CBFV}$ from previous studies. In the future, using Valsalva for analyzing correlation between $ln(\frac{1}{PTT})$ and pressure in the carotid requires $\overline{CBFV}$ or a direct pressure measurement of the subject under test.

4.3.3 Estimating Blood Pressure Below the Head, and Accounting for Vessel Radius

Cold pressor maneuvers were completed by subjects H014 and H015. The effect of the cold pressor on blood pressure below the head is quite dramatic, with increases in pressure of $25 - 30\%$ over prolonged periods. This large, and lengthy change makes the cold pressor a good maneuver for estimating blood pressure below the head with $ln(\frac{1}{PTT})$. Since the BCG is a total body movement, taking the interval from the J-wave at the ear, to the edge of the PPG from the finger is akin to making measurements beginning at the aortic arch, and traveling along the brachial and radial arteries.

As mentioned in section 3.6.1, the radius of the vessel under test is proportional to cardiac output and mean blood pressure, and is not constant. Utilizing the SV calculation from the BCG J-wave amplitude, and heart rate to obtain cardiac output, we can recursively solve for MAP and obtain a scaling factor for the change in radius,

as shown in equation 3.13. Using the ECG, BCG, and PPG allow for comparison of blood pressure estimation with $ln(\frac{1}{PAT})$, $ln(\frac{1}{PTT})$, and *adjusted* $ln(\frac{1}{PTT})$, where *adjusted* $ln(\frac{1}{PTT})$ accounts for the estimated change in vessel radius.

Figure 4-19 compares calibrated $ln(\frac{1}{PAT})$, $ln(\frac{1}{PTT})$, and *adjusted* $ln(\frac{1}{PTT})$ from a PPG at the finger, against the MAP obtained by the Finapres for subject H014 during the cold pressure experiment. The bottom plot corresponds to the calculated normalized change in $ln(r)$. For estimation of the vessel radius, cardiac output was generated by averaging 10 values around the data point of interest, and the previous value of estimated MAP was used for ΔP. Five calibration points were used for each plot, and none of the points were taken after 300 seconds into the test.

In Figure 4-19, calibrated $ln(\frac{1}{PAT})$ shows difficulty tracking Finapres MAP during transients as the hand is placed in and out of the cold pressor. There is also a significant positive bias after the hand has been out of the cold pressor through the end of the test. Calibrated $ln(\frac{1}{PTT})$ follows Finapres MAP better than calibrated $ln(\frac{1}{PAT})$ during transients, and after the hand has been removed from the cold pressor. However, there is a slight negative bias while the hand is inside of the cold pressor. Calibrated *adjusted* $ln(\frac{1}{PTT})$ tracks the first transient similarly to $ln(\frac{1}{PAT})$, and the second transient better than both $ln(\frac{1}{PAT})$ and $ln(\frac{1}{PTT})$. Additionally, the bias is further reduced after the hand has been removed from the cold pressor. However, there is a greater negative bias while the hand is inside the cold pressor. Figure 4-20 shows Bland-Altman plots corresponding to different blood pressure estimations using a PPG at the finger for subjects H014 and H015. The data bias is minimized when adjusting for the change in radius ($+1.1mmHg$), but the standard deviation is minimized when $ln(\frac{1}{PTT})$ is used ($\pm 7.8mmHg$).

Data in Figure 4-19 show that the PEP reduces after the cold pressor maneuver, and does not return to baseline within the first 3 minutes after the maneuver has been completed. This is evidenced by the positive bias in calibrated $ln(\frac{1}{PAT})$ shown in Figure 4-20a. The data also suggest that accounting for the change in vessel radius can improve $ln(\frac{1}{PTT})$ to MAP algorithms during large transients. However,

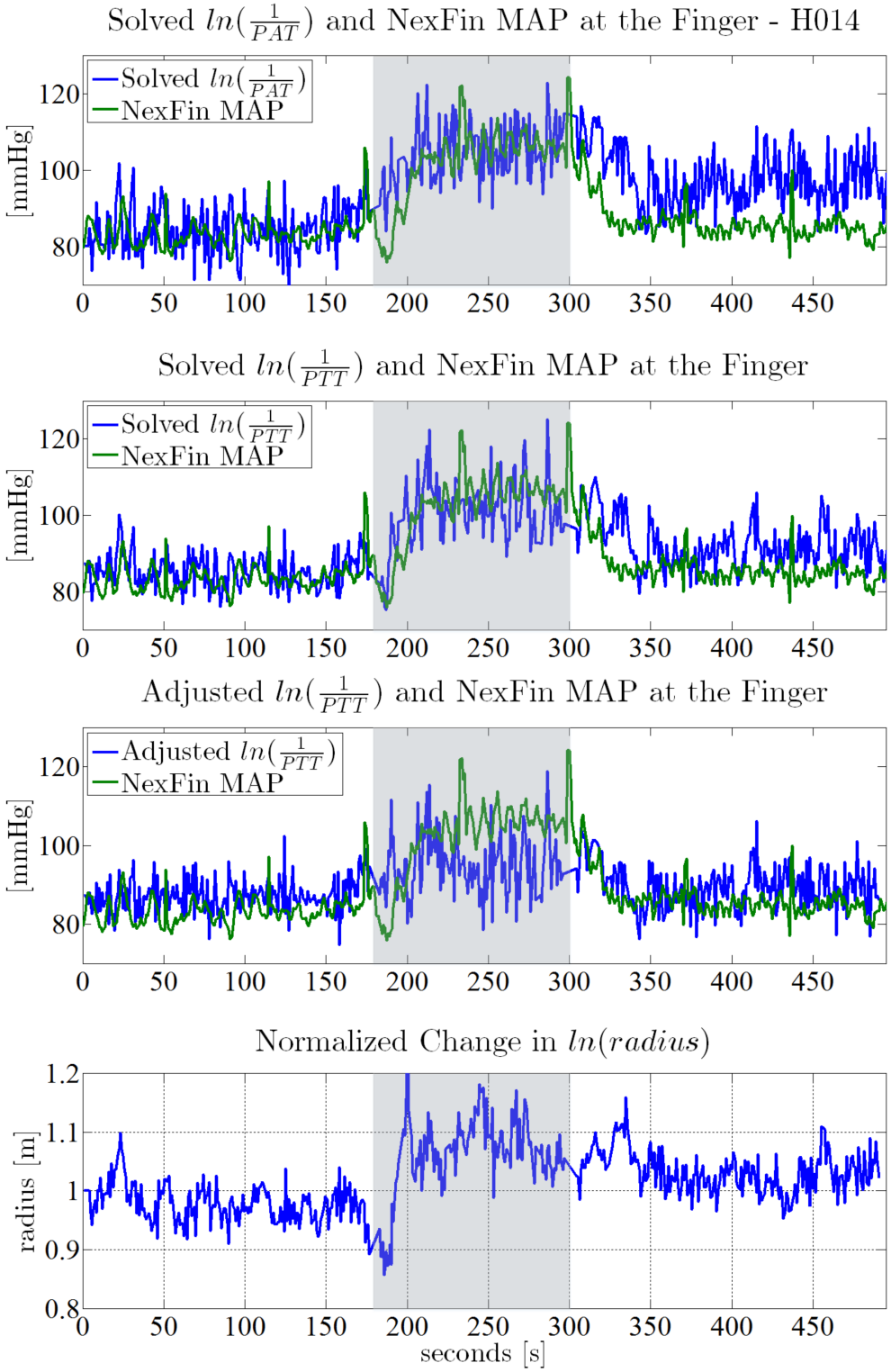

Figure 4-19: Subject H014 cold pressor maneuver. Top: $ln(\frac{1}{PAT})$ to a finger PPG (blue) and Finapres MAP (green). Second: $ln(\frac{1}{PTT})$ to a finger PPG (blue) and Finapres MAP (green). Third: Adjusted $ln(\frac{1}{PTT})$ to a finger PPG (blue) and Finapres MAP (green). Bottom: Normalized change of the vessel radius.

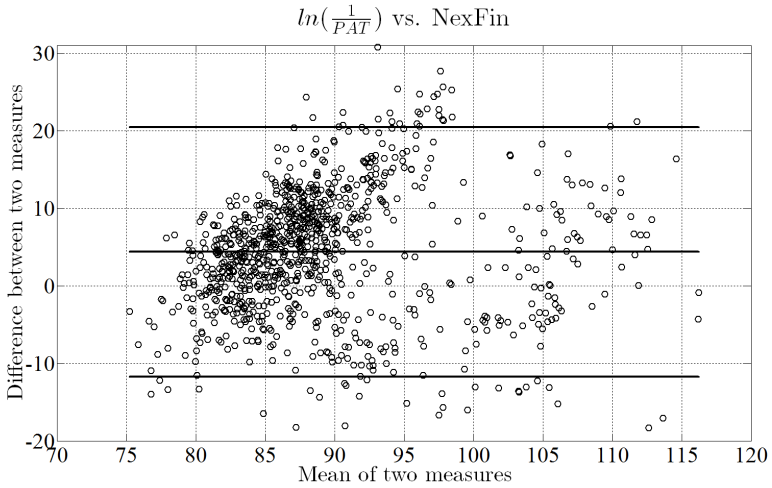

(a)

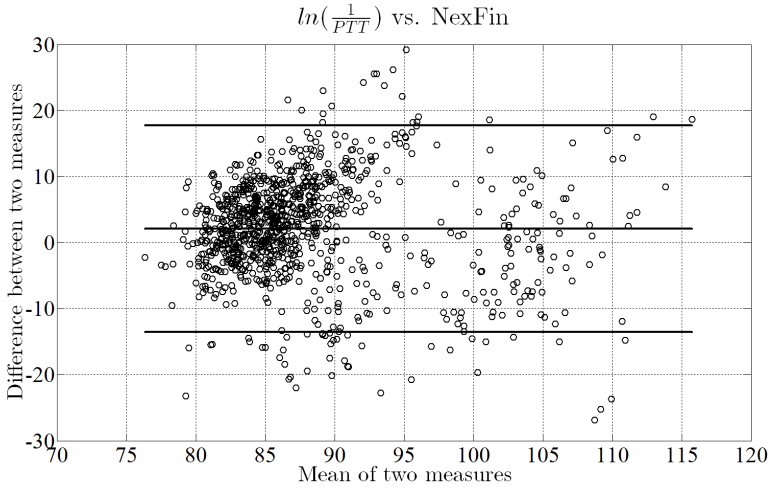

(b)

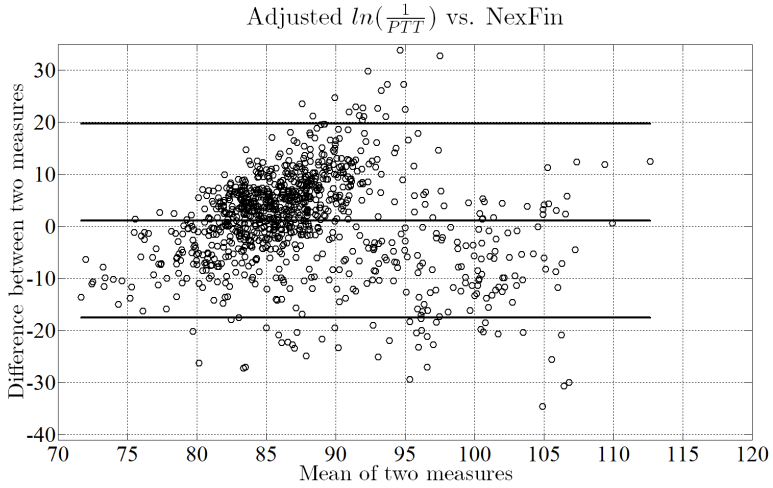

(c)

Figure 4-20: Bland-Altman plots for subjects H014 and H015 for a) $ln(\frac{1}{PAT})$, b) $ln(\frac{1}{PTT})$ and c) adjusted $ln(\frac{1}{PTT})$.

accounting for the change in vessel radius increased the standard deviation from 7.8 to 9.3 mmHg compared to estimations using $ln(\frac{1}{PTT})$ without accounting for the change in vessel radius. Table 4.2 shows correlation values for subjects H014, H015, and the concatenation of both datasets. The P-values for $ln(\frac{1}{PTT})$ and *adjusted* $ln(\frac{1}{PTT})$ from subject H015 were not statistically significant ($P > 0.05$).

Subject	**PAT R value**	**PAT P value**	**PTT R value**	**PTT P value**	**Adj. PTT R value**	**Adj. PTT P value**
H014	0.6012	0.0000	0.6393	0.0000	0.4358	0.0000
H015	0.0976	0.0322	-0.0552	0.2262	0.0479	0.3023
Total	0.5474	0.0000	0.5083	0.0000	0.3077	0.0000

Table 4.2: Statistical significance of finger PPG intervals to MAP

4.4 Summary

The wearable CHF monitor hardware and software were characterized in detail. The clinical testing protocol, which was used for proof-of-concept experimentation for PTT-to-BP algorithms and measurement system was also described. Test results showed morphological changes of $ln(\frac{1}{PTT})$ from the wearable CHF monitor compared directly with that of $\overline{CBFV}$ from previous studies during sit-to-stand maneuvers. They were theoretically shown to be dominated by changes in pressure in the carotid artery instead of vessel radius. Using the J-wave from the BCG as the first PTT time marker, and the edge of the PPG at the mastoid for the second PTT time marker, allowed for continuous measurement from a single site on the body. Cold pressor experiments also compared $ln(\frac{1}{PTT})$, *adjusted* $ln(\frac{1}{PTT})$, and $ln(\frac{1}{PAT})$ from a finger PPG to continuous Finapres MAP. Hysteresis in the PEP of the heart was observed and contributed to error in $ln(\frac{1}{PAT})$ to MAP, compared to using $ln(\frac{1}{PTT})$. Finally, adjusting the values of the calibration constants for changes in vessel radius improved $ln(\frac{1}{PTT})$ to MAP during cold pressor transients, but increased the overall standard deviation for the duration of the test.

Chapter 5

A Reflectance Mode PPG Architecture

This chapter begins with a description of a typical PPG receiver signal chain. Dynamic range enhancement (DRE) architectures are then introduced as a way to improve the dynamic range of a PPG receiver. A new DRE architecture will then be explained which does not negatively affect the desired bandwidth of the PPG signal, and it will be compared to previous work. Next, previous time-varying interferer removal algorithms will be explained, and a novel, low-power on-off keying (OOK) modulation, sampling, filtering and demodulation architecture is proposed to remove unwanted time varying interferers from the PPG signal.

5.1 A Typical PPG Receiver Architecture

A simplified block diagram of a typical PPG receiver is shown in Figure 5-1. The photodiode receives light emitted from the LEDs that has passed through tissue, typically the finger, and the signal is amplified by a transimpedance amplifier. If the PPG receiver is used for multiple wavelengths, as in pulse oximetry, then the LEDs are turned on serially, and the signals are demodulated into separate signal chains, followed by analog signal conditioning, such as low-pass filtering and correlated double sampling [27]. After analog signal conditioning, the signal is converted to the digital domain, where calculation of physiological parameters such as timing information, or blood oxygenation can occur.

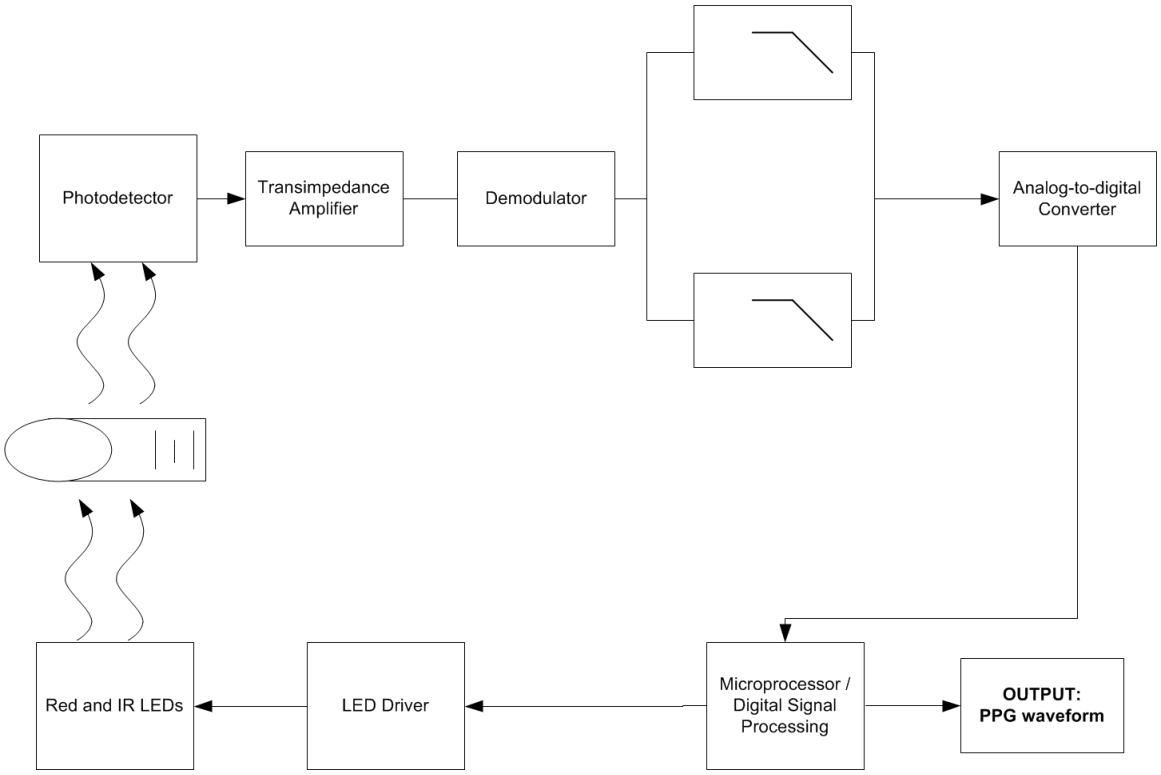

Figure 5-1: Block diagram of a typical PPG front end.

Although this simple architecture can work for finger transmission-mode probes and higher voltage front ends, it poses several challenges to single-supply, low voltage and low-power reflectance-mode operation. Two solutions to these challenges will be addressed in the following subsections.

5.2 Techniques for Dynamic Range Enhancement in PPG Front Ends

5.2.1 Existing Techniques

Removal of the static portion of the PPG signal, as well as static interferers is required for low-voltage and high transimpedance gain PPG front ends. For example, if the pulsatile portion of the PPG signal has a magnitude of $300nA$, and is $\frac{1}{100}\times$ the static portion, the total amount of photocurrent is $30\mu A$. A front end transimpedance of $1M\Omega$ would yield an output of $30V$, with only $300mV$ being part of the pulsatile

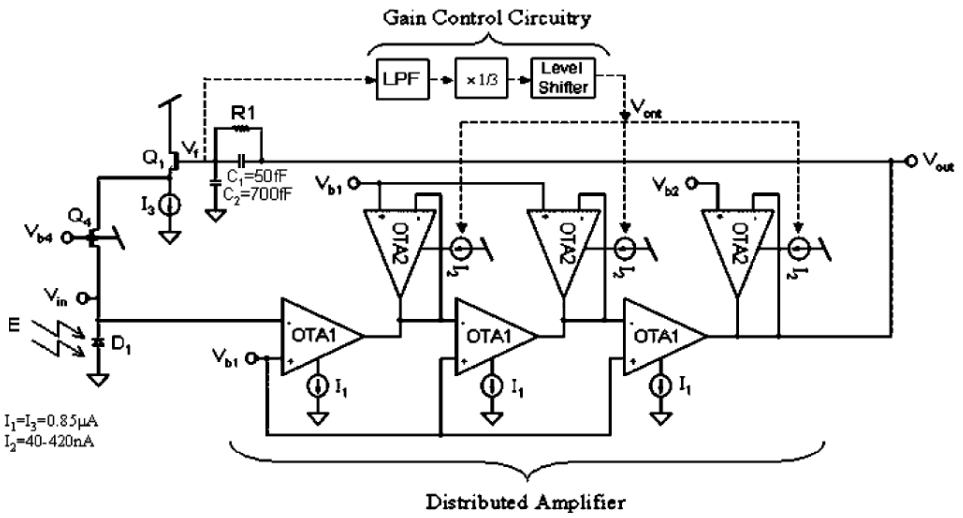

Figure 5-2: Logarithmic front end as designed by Tavakoli [58].

PPG. If the PPG is taken in reflectance-mode, then ambient lighting such as sunlight could become incident on the photosensor, thus increasing the total amount of static current and ultimately, the output voltage of the transimpedance amplifier. For low-power and wearable applications, a front end with a 30V supply is not feasible.

Techniques to increase the dynamic range of a PPG front end have mostly stayed in the analog domain. Tavakoli utilized a log amplifier at the front end with a sinh resistor in feedback, as shown in Figure 5-2, to logarithmically increase the amplifier output to changes in DC levels while still maintaining high gain of the pulsatile portion of the PPG signal [58]. This method achieves a wide dynamic range in the front end (∼6 orders of magnitude) at the cost of added analog complexity. A second approach utilizes an error amplifier in feedback to the photo-receptor, as shown in Figure 5-3. The error amplifier drives a current sourcing FET which removes static current from the PD [59]. This approach pins the output voltage of a transimpedance amplifier (TIA) to a specific value, which adds a zero to the transfer function at DC. The pass-band of this technique is therefore also dependent upon the total amount of current sourced by the FET. Due to the low-frequency nature of PPG signals, it is very difficult to generate a pole close enough to DC in an integrated circuit such that the pass band of the PPG signals begins at 1 Hz or below, as shown in Figure 5-4.

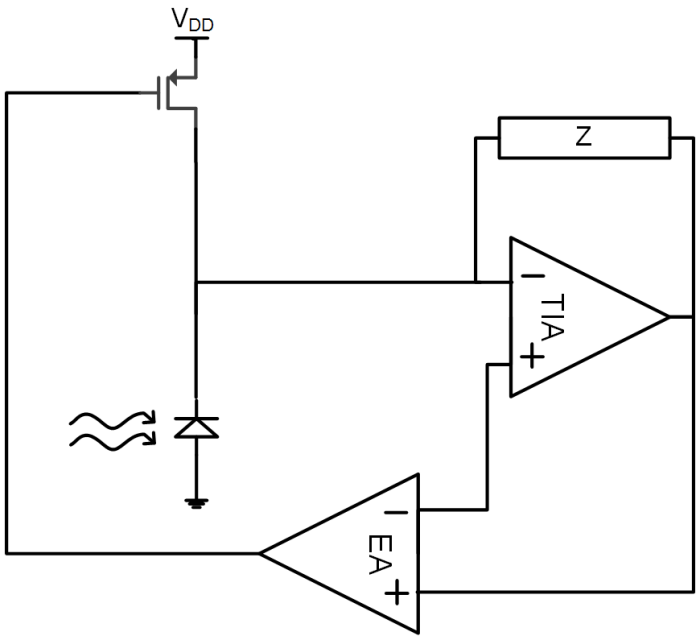

Figure 5-3: A simplified schematic of using an error amp in feedback with a photoreceptor to subtract static current from a photo-diode.

A third dynamic range enhancement technique previously reported was designed by Patterson et al. [60]. Patterson used a digitally-assisted analog technique to subtract ambient light from his photoreceptor, as shown in Figure 5-5. His algorithm updates the subtraction current at >10 Hz intervals, and the subtraction steps are finely tuned.

5.2.2 A New DRE Technique for Removing Static Interferers

One of the biggest challenges with designing a low-voltage PPG system is the limited dynamic range at the front end. This challenge becomes more difficult when the PPG system operates in reflectance-mode, where mechanically blocking ambient light from incidence on the sensor is not feasible. In order to mitigate this dynamic range challenge, a digitally assisted analog dynamic range enhancer (DRE) architecture has been designed to increase the dynamic range of the front end by up to 40dB. The DRE architecture is comprised of a current DAC, which is used to subtract a static amount of current (I_{st}) from the photodiode current (I_{ph}), and an amplifier to amplify

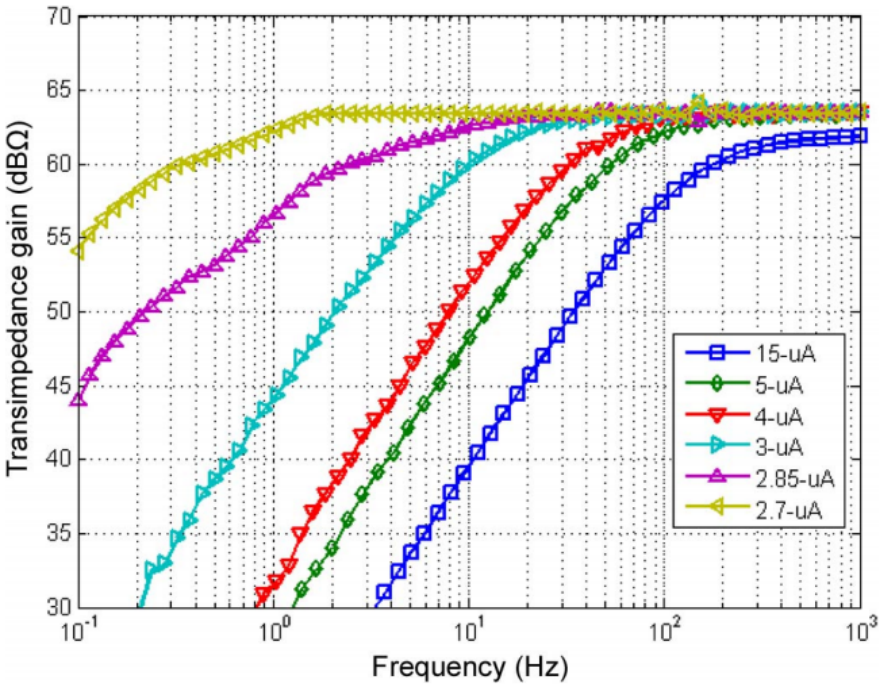

Figure 5-4: Frequency response characteristics of a static current subtraction scheme utilizing an error amplifier in feedback (figure from [59]).

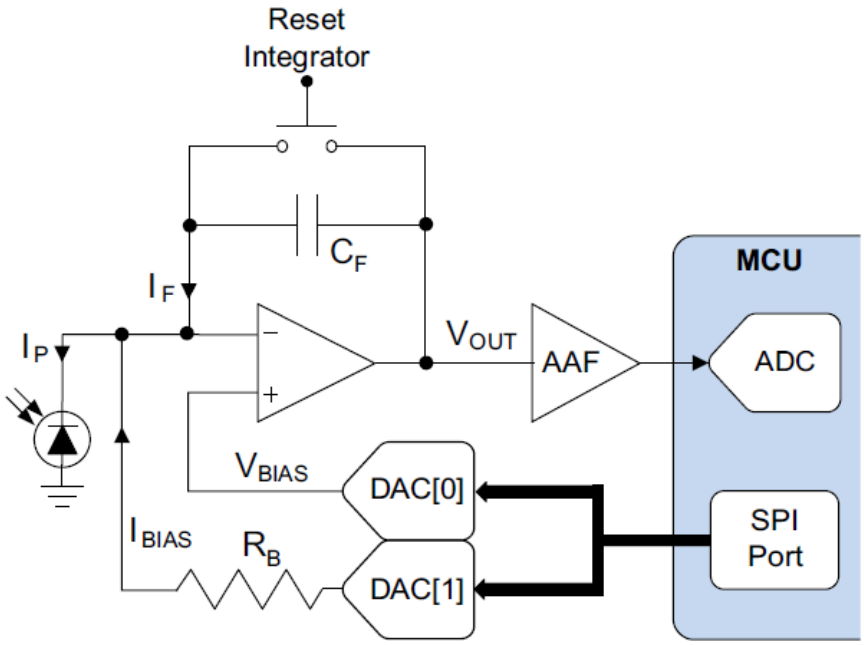

Figure 5-5: Diagram of the digitally assisted analog current subtraction technique utilized by [60]. The subtraction DAC (DAC[1]) was updated digitally at >10Hz to remove static ambient interferers (figure from [60]).

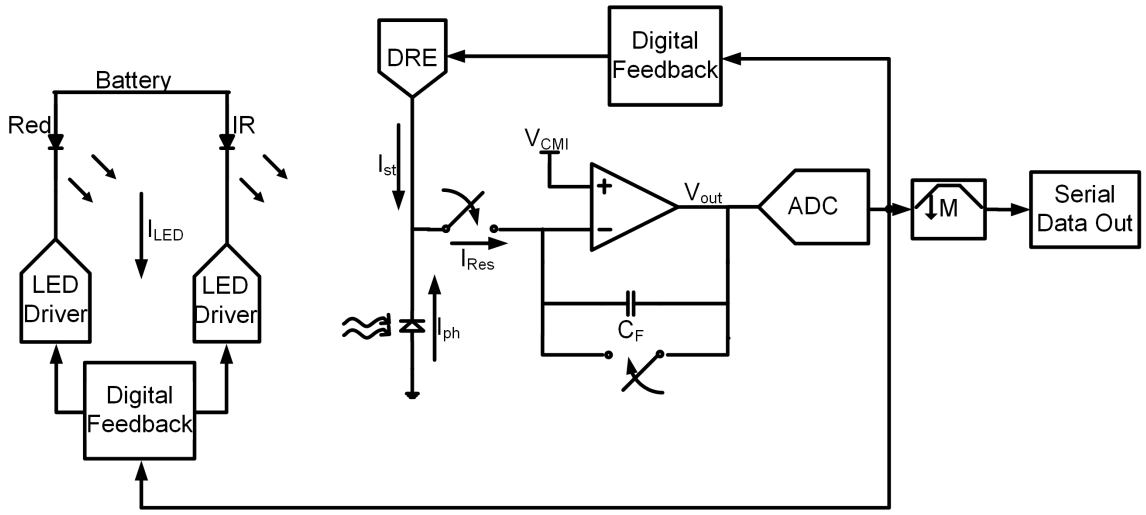

Figure 5-6: A System block diagram showing the components for the DRE architecture.

the residue (I_{Res}) of the current, LED drivers which sink (I_{LED}) from the LEDs, and a digital feedback component, as shown in Figure 5-6.

The DRE architecture operates in the following manner. I_{Res} is amplified and digitized. If the digitized output V_{out} is greater than a minimum threshold, and less than a maximum threshold, then the digital feedback will not change I_{LED} or I_{st}. If V_{out} is below a minimum threshold, the algorithm checks to see if I_{LED} can be increased. If it can, then it will increase I_{LED} and wait for the next sample. If I_{LED} is already at a maximum, then the algorithm decreases I_{st} and resets I_{LED} to zero.

Similarly, if V_{out} is greater than a maximum threshold, the algorithm checks to see if I_{LED} can be decreased. If it can, then it will decrease I_{LED} and wait for the next sample. If I_{LED} is already at a minimum threshold, then the algorithm increases I_{st} and resets I_{LED} to zero. Figure 5-7 is a flow diagram of the digital feedback algorithm and Figure 5-8 visually shows how I_{LED} and I_{st} change with respect to V_{out}.

This digitally-assisted analog technique has several advantages. First, compared to [60], which was limited to subtracting $3.24\mu A$, it can subtract large amounts of static current, as the DRE block can be implemented as a tunable current source. Implementing a tunable current source removes the dependence of supply voltage on

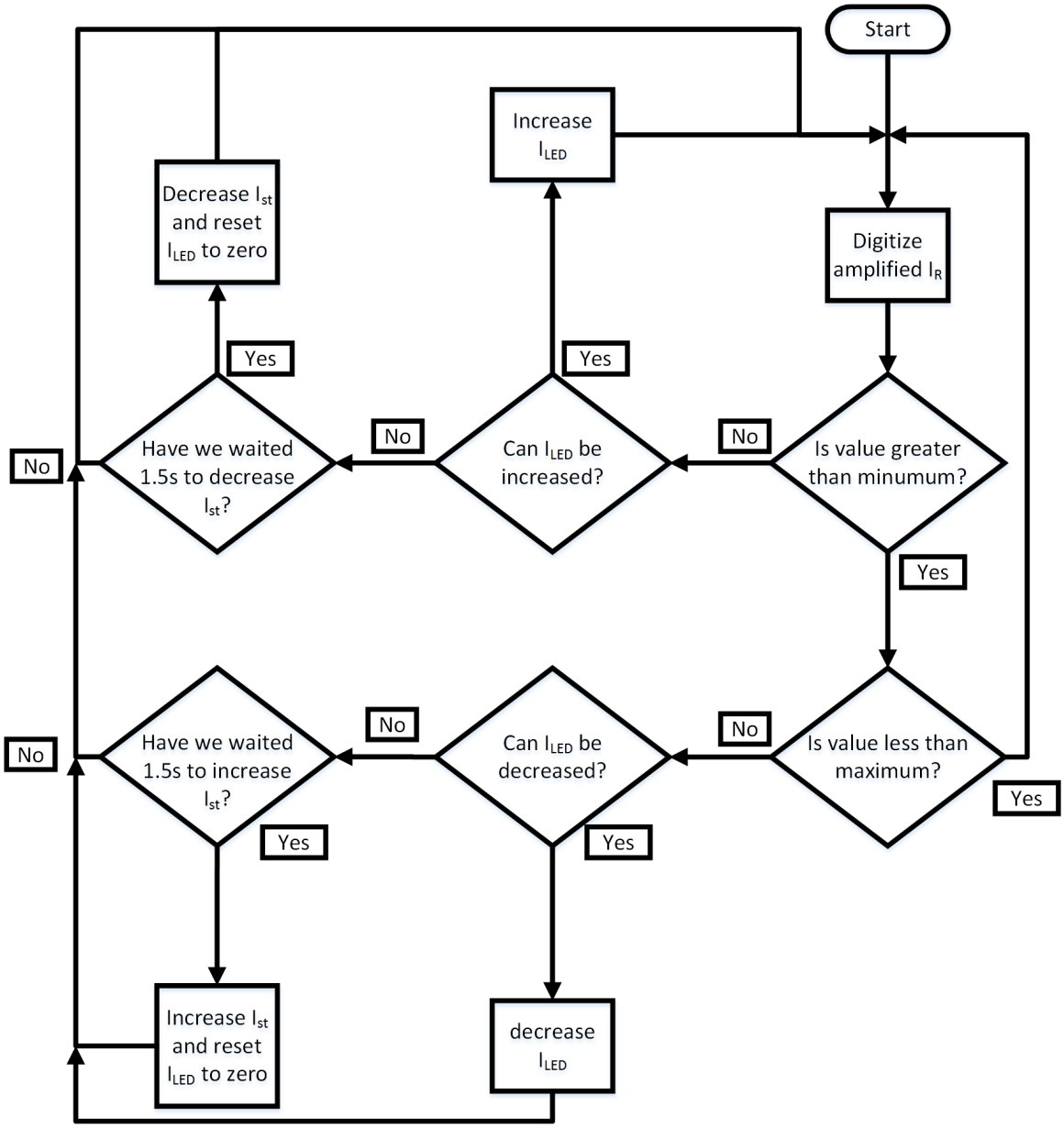

Figure 5-7: A flow diagram for the digital feedback algorithm of the DRE architecture.

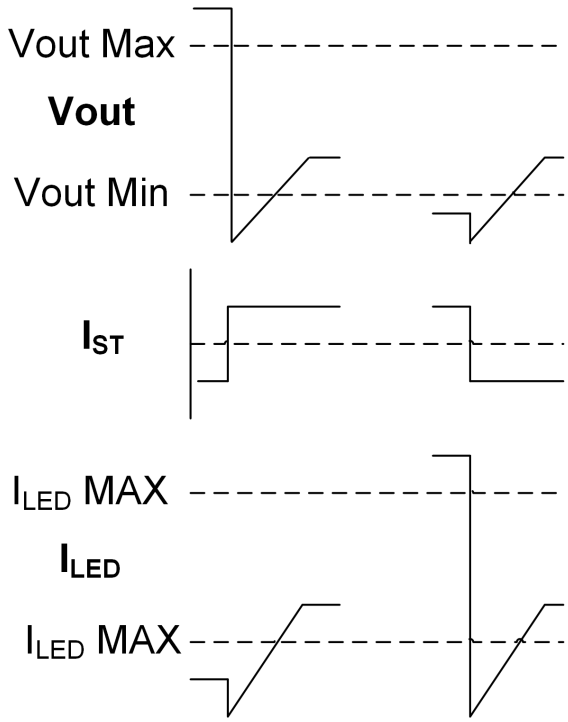

Figure 5-8: A signal diagram showing how I_{st} and I_{LED} change with respect to V_{out}.

the static subtraction current, allowing for low-voltage operation of the front end. Second, compared to [59], the pass-band of the proposed DRE does not infringe on the PPG band of interest because the output of the integrator (V_{out}) is not pinned to a specific voltage. This means a zero is not placed into the transfer function at DC, leaving the PPG bandwidth of interest in tact. Also compared to [59] where the amount of static current is unknown, the DRE output (I_{st}) is known a priori due to the digital code loaded into the DRE. This helps to further improve the accuracy of SpO_2 estimations compared to not knowing the amount static current, as shown by equation (2.8). Finally, the proposed DRE architecture is highly tunable due to its digital nature. Therefore, current steps and refresh rates can be adjusted as needed.

5.3 Techniques for Removing Time-varying Interferers in PPG Front Ends

5.3.1 Existing Techniques

Removal of time-varying interferers from the PPG signal is another difficult design challenge. Often times, PPG systems will reduce their sample rate to conserve power consumption. This reduction can cause frequencies from ambient lighting to alias into the PPG bandwidth of interest if they are not filtered properly. Additionally, higher order harmonics can be mixed directly into the bandwidth of interest. For example, a PPG system that samples at 100 Hz will modulate 120 Hz from fluorescent lights down to 20 Hz and 60 Hz from incandescent lights down to 40 Hz. The 5th harmonics of both 60 Hz and 120 Hz will also modulate directly into the baseband. Setting a low pass filter in the analog domain at 10 Hz for the PPG signal will negligibly attenuate these interferers. When accounting for both 50 / 60 Hz power frequencies, the spectrum becomes very crowded and sample frequencies must be chosen with care. The interfering frequencies include 50, 60, 75, 100, and 120 Hz along with up to 25 of their harmonics [61] [62].

Figure 5-9 shows an illustration of how a PPG signal is typically sampled, and its resulting spectrum. In this architecture, the PPGs are sampled and the LEDs are highly duty cycled. While the LEDs are off, the system does not sample the ambient interferers, resulting in a spectrum where a low frequency interferer is close to baseband, and it's harmonics are mixed down to frequencies between DC and the sample frequency. Images of the spectrum are repeated at sample frequency intervals.

The simplest technique to remove time varying ambient interferers is that of Correlated Double Sampling (CDS) [63]. This technique samples the ambient light onto a capacitor and then subtracts that value from a subsequent PPG sample in the analog domain. Similarly, this technique can also be applied in the digital domain by converting an ambient sample and subtracting it's value from a subsequent PPG

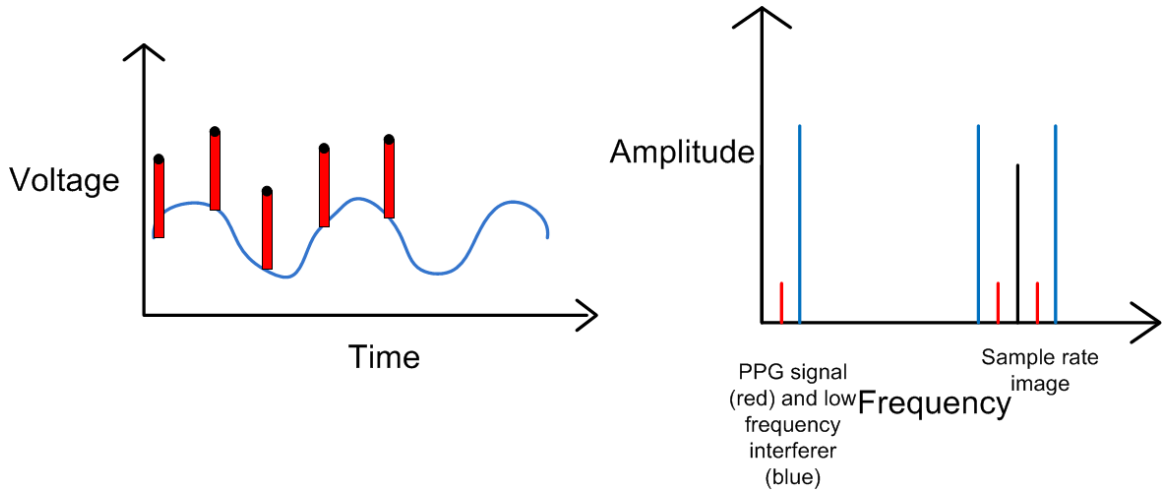

Figure 5-9: Typical method of sampling a PPG signal (left) where the red bars indicate the LED is on and the black dot indicates a sample is taken. The blue signal indicates a time-varying interferer incident on the photodiode. The spectrum of the typical method of sampling (right) shows low frequency interferers close to the PPG signal band of interest as well as the first image around the sample frequency.

sample. Although simple, this technique can be ineffective as it is dependent on the time in-between the ambient and PPG samples, as shown in Figure 5-10.

To obtain higher levels of attenuation, more intricate filtering schemes must be employed. Patterson [60] used a homodyne detection algorithm where the LED drive current was modulated with a sine wave. The frequency chosen was 250 Hz with a sample rate of 1 kHz. This placed his PPG signal directly on top of the 5th harmonic of the 50 Hz mains and in-between the second and third harmonics of 100 Hz florescent lights. Although effective at removing some interferers, it was a higher power implementation due to the high LED turn-on frequency of 1 kHz, and the fact that he used a multiplication of a sine wave to demodulate the PPG signal to baseband. His use of a lattice wave digital filter structure to conserve power also can be undesirable when phase distortion cannot be tolerated, such as for finding peak or edge timing information from a signal.

Grubb et al. modulated the LED's with a square wave instead of a sinusoid [64]. Figure 5-11 shows a block diagram of his system. Grubb once again used a very high LED turn on frequency of 575 Hz and a sampling frequency of 2300 Hz, which increased LED power significantly, followed by an I-Q demodulator to bring the signal

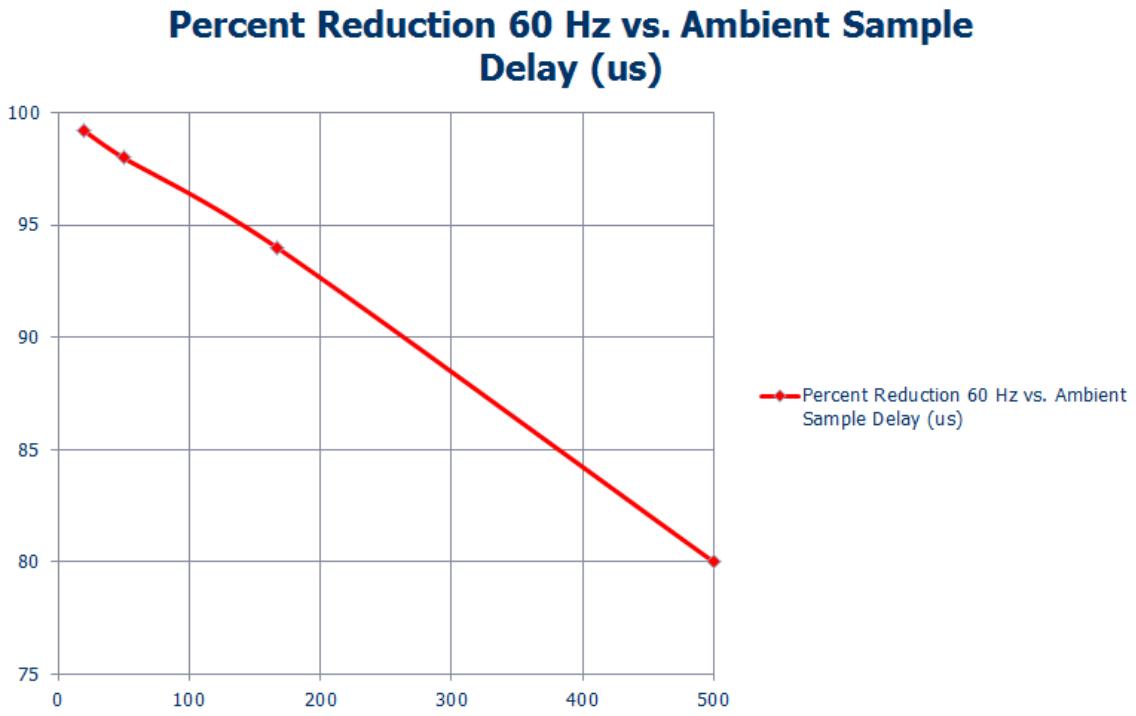

Figure 5-10: A graph of the percent reduction of a 60 Hz interferer from a PPG signal using the simple subtraction method. Interferer attenuation reduces linearly with increasing interferer frequency. Even at 60 Hz, greater than 26 dB of attenuation requires sample times on the order of 100 μs.

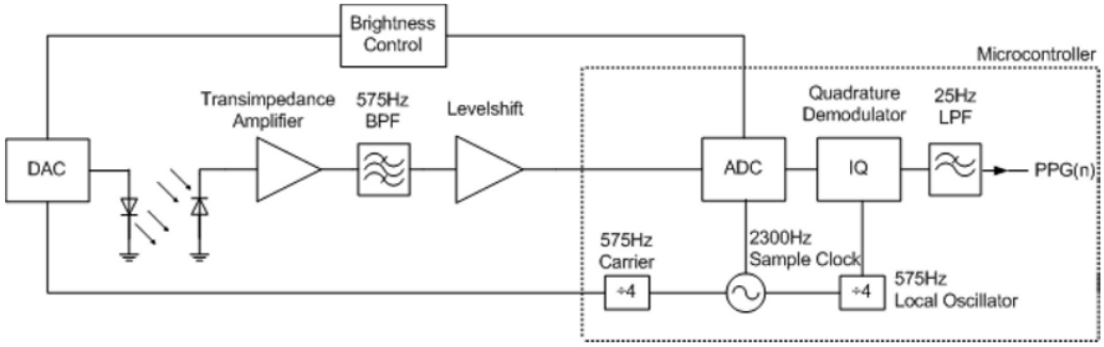

Figure 5-11: Block diagram of the lock-in amplifier used by Grubb et al. The lock-in frequency was 575 Hz with a system sample rate of 2300 Hz [64].

back to baseband.

5.3.2 A Modulating, Filtering and Decimation Technique for Time Varying Ambient Interferer Removal

To remove these interferers in a low-power manner, a modulating, filtering and decimation architecture is presented. This architecture first involves sampling the output of the photoreceptor when the LEDs are on, as well as when the LEDs are off. This technique and it's resulting spectrum are shown in Figure 5-12. As can be seen, the PPG signal is modulated at integer multiples of the LED turn on frequency, whereas the interferers stay at baseband. Next, filtering around one of the images in a clean portion of the spectrum can remove extra modulated images and unwanted interferers, while decimation is used to demodulate the signal back to baseband in a low-power manner.

Mathematically the technique can be explained in the following manner. We define the PPG signal when the LEDs are on as $p(t)$ and sample with an impulse train $s(t)$, which is defined by:

$$s(t) = \sum_{n=-\infty}^{\infty} \delta(t - nT) \tag{5.1}$$

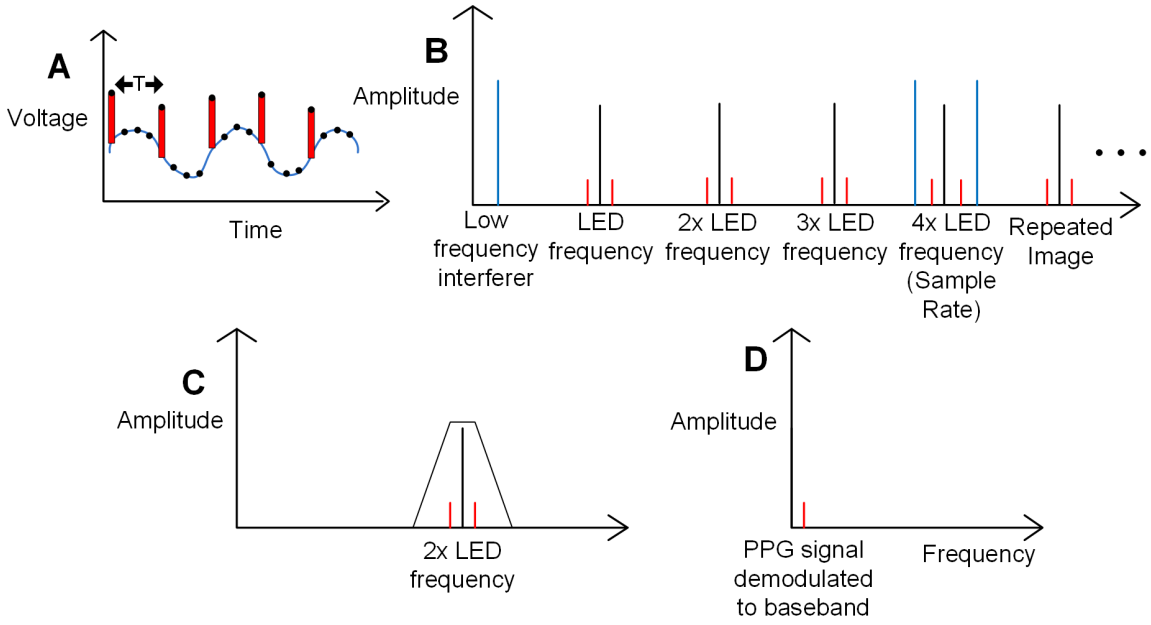

Figure 5-12: A: Sampling the PPG signal and ambient interferers results in B: a spectrum where the PPG signal is modulated to integer multiples (in this case, 4) of the LED turn-on frequency. C: Filtering around the second image and D: demodulating by decimation removes interferers while maintaining a clean, uncorrupted PPG signal in a low-power manner.

where T is the sample period of the pulse train, shown graphically as the time between the red bars in Figure 5-12A. The combined time domain signal for the sampled PPG $x_s(t)$is defined as:

$$x_s(t) = s(t) \cdot p(t) = \sum_{n=-\infty}^{\infty} P(nT)\delta(t - nT) \tag{5.2}$$

The frequency domain representation of $x_s(t)$ is shown in Figure 5-12B and represented by:

$$X_s(j\Omega) = \frac{1}{2\pi} S(j\Omega) * P(j\Omega) = \frac{1}{T} \sum_{k=-\infty}^{\infty} P(j(\Omega - k\Omega_s)) \tag{5.3}$$

where Ω_s is $\frac{(2\pi)}{T}$. This is a mathematical representation of the PPG signal $P(j\Omega)$ modulated at intervals of $k\Omega_s$ where k is an integer.

The ambient light $a(t)$ is sampled with a period of $\frac{1}{4T}$ and is represented in the

frequency domain by:

$$X_n(j\Omega) = \frac{1}{4T} \sum_{k=-\infty}^{\infty} A(j(\Omega - 4k\Omega_s)) \tag{5.4}$$

From equation (5.4), we see that the ambient light $A(j\Omega)$ has images around integer multiples of $4\Omega_s$ instead of Ω_s. The combined PPG signal and ambient light signal $X_{total}(j\Omega)$ is shown through superposition to be:

$$X_{total}(j\Omega) = X_s + X_n = \sum_{k=-\infty}^{\infty} (\frac{P(j(\Omega - k\Omega_s))}{T} + \frac{A(j(\Omega - 4k\Omega_s))}{4T}) \tag{5.5}$$

After filtering $X_{total}(j\Omega)$, the resultant signal $X_f(j\Omega)$ is:

$$X_f(j\Omega) = X_{total} \cdot H_f(j\Omega) = \sum_{k=-\infty}^{\infty} (\frac{P(j(\Omega - k\Omega_s))}{T} + \frac{A(j(\Omega - 4k\Omega_s))}{4T}) \cdot H_f(j\Omega) \tag{5.6}$$

where the filter $H_f(j\Omega)$ is defined as 1 inside BW and 0 elsewhere. Downsampling the signal by a factor of M results in:

$$X_d(j\Omega) = X_f(\frac{j\Omega}{M}) = \frac{1}{M} \sum_{i=0}^{M-1} [\frac{1}{4T} \sum_{k=-\infty}^{\infty} X_f(j(\frac{\Omega}{4MT} - \frac{2\pi k}{4T} - \frac{2\pi i}{4MT}))] \tag{5.7}$$

which is a set of M copies of X_f frequency scaled by M and shifted by integer multiples of $\frac{2\pi}{M}$, which places a copy of X_f back in the baseband, completing the demodulation [65].

Going back to the original problem of a crowded spectrum, choosing the LED turn-on frequency, and the overall sampling frequency is crucial to ensuring a clean area of the spectrum to modulate the PPG signal. The widest area of clean spectrum is from 300 - 360 Hz in the US and 300 - 350 Hz in Europe. Sampling at 660 Hz, with an LED turn-on frequency of 165 Hz modulates the second image of the PPG signal right at 330 Hz, while modulating higher order harmonics from 50/60 Hz into the stop band, leaving the clean spectrum intact. By defining the pass-band as 320 - 340 Hz, it can be shown that this sample scheme modulates every 60 and 120 Hz

harmonic into the stop-band. The first 75 Hz harmonic modulated into the pass-band is the 22nd harmonic, which is modulated down to 330 Hz from 1650 Hz. The first 50 Hz harmonic modulated into the pass-band is at 1000 Hz which is the 20th harmonic, and it is modulated down to 340 Hz. The first 100 Hz harmonic modulated into the pass-band is also at 1000 Hz, which is the 10th harmonic and it is modulated to 340 Hz. Sampling at 4x the LED turn-on frequency also reduces the white noise in the BW by a factor of 2. Filtering with this method also attenuates 1/f circuit noise below 320 Hz by the magnitude of the stop-band and transition-band of the filters.

The frequencies aliased into the pass-band f_{alias} are defined by:

$$f_{alias} = 2 \cdot f_{LED} + \sum_{n=1}^{N} n \cdot BW \cdot f_{sample} \tag{5.8}$$

where BW is the bandwidth of the bandpass filter, f_{LED} is the turn on frequency of the LEDs, f_{sample} is the sample frequency of the system, and N is defined by:

$$N = \frac{BW_{AFE}}{f_{sample}} \tag{5.9}$$

where BW_{AFE} is the bandwidth of the analog front end signal chain.

Turning on the LED's at 165 Hz and choosing the modulated image at 330 Hz also keeps the LED power low, as the LED turn-on frequency is close to the 100 Hz value noted for other low-power PPG systems. Finally, low-power digital filtering can achieve attenuation of 80dB or greater in the entire stop-band while negligibly increasing the power budget.

Compared to [60] and [64], the proposed architecture has several advantages. First, the technique is low power due to the reduced LED turn-on frequency. The turn-on frequency for [60] is 1kHz, while the turn-on frequency for [64] is 0.575kHz, whereas the proposed architecture has a turn-on frequency of 0.165kHz. The LED driver design is also simpler compared to [60] since the current is not being modulated by a sine wave. Demodulation through decimation is also lower power compared to a lock-in amplifier or IQ demodulator.

5.4 Summary

Dynamic range was introduced as an engineering challenge to low-voltage, low-power, reflectance-mode PPG systems. Previous methods to improve dynamic range were described and a new dynamic range enhancement (DRE) architecture was explained. The new DRE method compared favorably to previous works in terms of overall increase in dynamic range, it's effect on the PPG bandwidth of interest, it's ability to know how much current is being subtracted, and it's tunable nature.

A second challenge to reflectance-mode PPG systems was identified as time-varying interferer removal. Two existing methods were explained and a novel time-varying interferer removal architecture was introduced. The new architecture was described graphically, and mathematically shown to reject known interferers and their harmonics. Compared to previous methods, the new architecture is lower power and allows for a simpler design of the LED driver.

Chapter 6

A Low-power Dual Wave Reflectance Mode PPG SoC for Continuous, Wearable Measurement

This chapter presents the design and measurement results of a sub-milliwatt, dual-wave photoplethysmogram (PPG) System on Chip (SoC). The PPG SoC contains a digitally-assisted-analog Dynamic Range Enhancer (DRE) circuit, as well as a modulation, sampling and digital filtering scheme for time varying ambient interferer removal, both of which are specifically useful for reflectance-mode photoplethysmography. Based on the device physics of photodiodes (PDs), and the noise requirements for pulse oximeters, system level optimizations using mixed-signal design and novel circuit topologies are implemented to significantly reduce power consumption. The PPG SoC includes the LED drivers, analog receive chain, analog-to-digital converter (ADC) and digital core for filtering and control of the aforementioned analog blocks. Every circuit required to make the SoC work is contained on the silicon except for the LED's, photodiodes, and bypass capacitors. Each circuit block is discussed in detail and measured IC results from both electrical and human tests are presented.

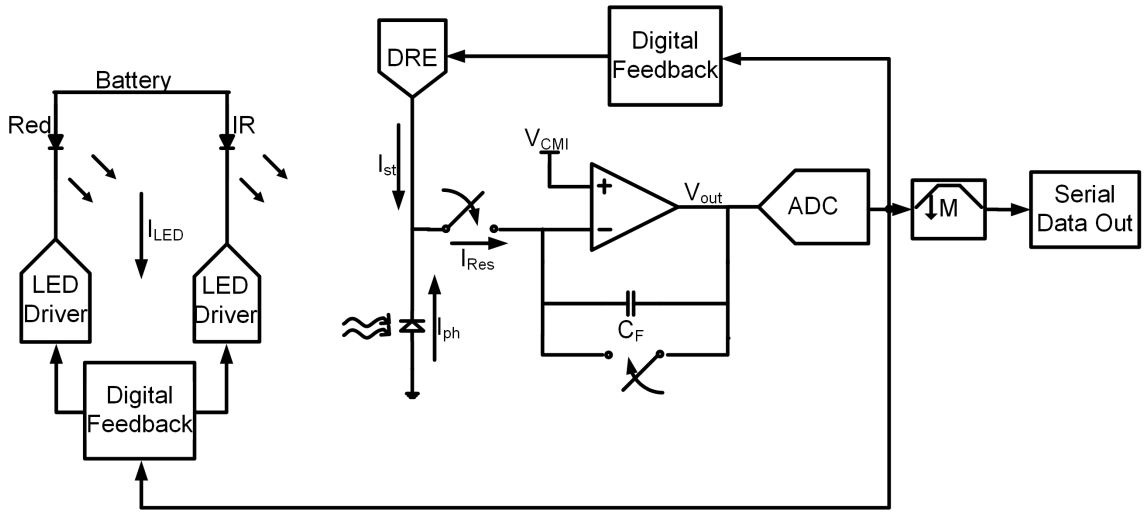

Figure 6-1: A simplified block diagram of the PPG SoC. The LEDs emit light into the body which is then reflected back to the photodiode, integrated and then converted to the digital domain. Digital feedback controls the DRE current (I_{st}) and LED driver current (I_{LED}) and FIR filters attenuate ambient interferers and decimate the PPG signal back to baseband. Everything is implemented on chip except for the LEDs and photodiode.

6.1 The PPG ASIC Circuit Design

6.1.1 The Analog Signal Chain

The PPG SoC block diagram is shown in Figure 6-1. The LED drivers sink current through the LEDs, which emit an optical signal that is amplitude modulated by the pulsatile blood in the body and reflected back to photodiodes. The residue (I_{Res}) of the photocurrent (I_{ph}) and estimated static current (I_{st}) is integrated onto capacitor C_F and inverted. The signal is then converted to the digital domain with the analog-to-digital converter (ADC). The following subsections describe the analog blocks individually.

6.1.2 The LED Drivers

The LED driver architecture is based on the wide swing cascode current DACs as mentioned in [66]. The transistors were sized with large area and long lengths to reduce the $\frac{1}{f}$ and thermal current noise. Therefore, the LSB for the DAC has a $\frac{W}{L}$ of

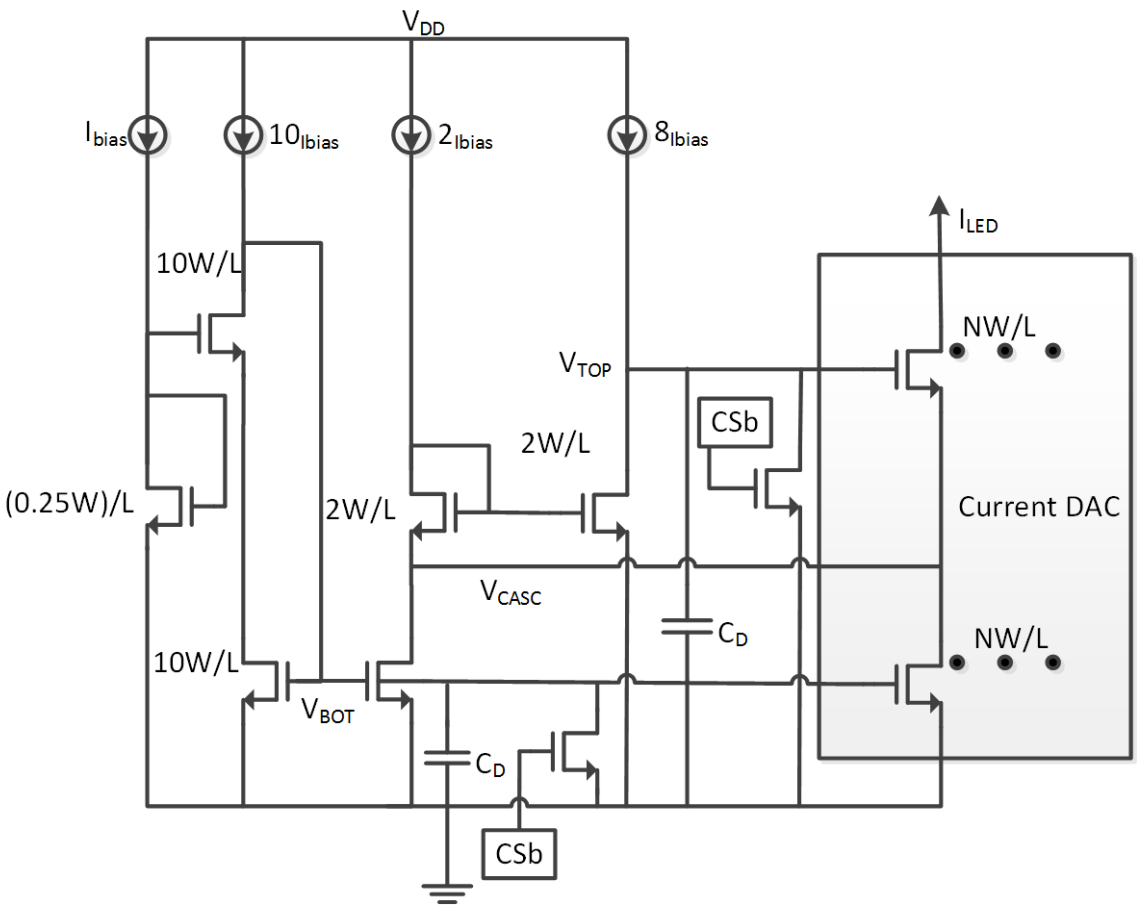

Figure 6-2: The circuit diagram of the wide swing cascode LED drivers [66]. W is 20μm and L is 2μm. I_{bias} is 10μA.

$\frac{20\mu m}{2\mu m}$ for both transistors in the cascode stack and an output current of $100\mu A$. The DAC has 8 bits of resolution for a maximum output current of 25.6 mA. Figure 6-2 shows biasing for the LED current DAC. The biasing is turned on and off quickly by toggling CSb.

The wide swing cascode design was chosen to minimize the voltage drop across the LED current source while maintaining a high output resistance. This gives high linearity of the current DAC over a wide range of drain voltages at the cascode transistor. The DAC was designed for LED battery voltage varying from $2.3V - 3V$ and LED on-voltages of $1.1V - 1.8V$. The bias network utilized high currents to reduce the transconductance of the bias devices and minimize thermal current noise. Section 6.2 discusses how this bias network is the dominant noise source in the LED

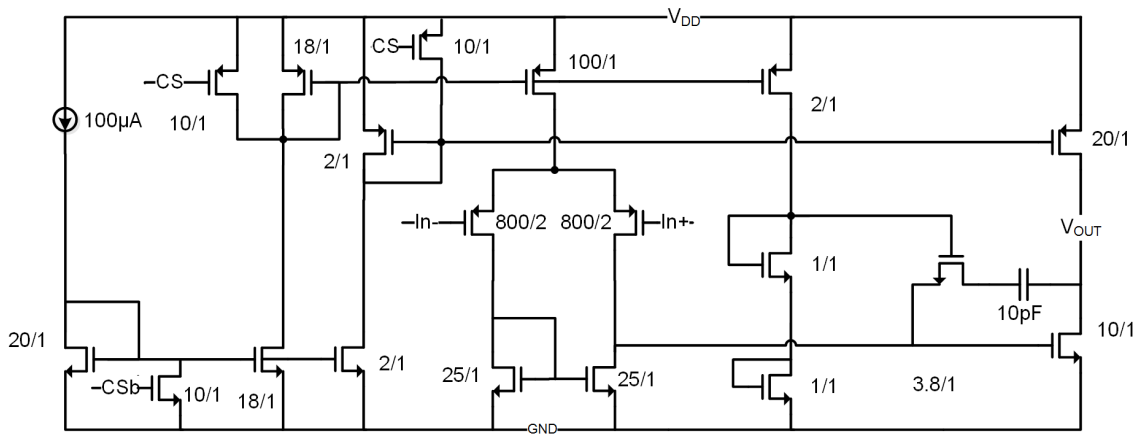

Figure 6-3: The integrating amplifier.

driver.

6.1.3 The Integrator

The integrator is comprised of a two stage operational amplifier (op-amp), an integrating capacitor C_F, and integration and reset switches. The differential pair of the op-amp is p-type with a size of $\frac{800\mu m}{2\mu m}$ to improve matching and lower $\frac{1}{f}$ noise. The bias network to the output has been decoupled from the bias of the differential pair to reduce switching feed-through from the DRE circuit. The differential pair tail current is 500μA and the compensation capacitor is 10pF, yielding a unity gain bandwidth of ∼20 MHz. The high bandwidth ensures greater than unity gain at the static current generator switching frequency of 6 MHz. The reference current is a fast-startup $100\mu A$ source for low duty cycles of the amplifier. Figure 6-3 shows the amplifier circuit with the device sizes.

Figure 6-4 shows the integrator circuit. The integrating capacitor C_F is nominally 40 pF, although it can be trimmed to 10, 20 or 30 pF. The reset switch S_R across C_F is $\frac{5\mu m}{1\mu m}$ and the integrating switch S_i is $\frac{50\mu m}{1\mu m}$. Switch S_{ph} grounds the photodiode while the amplifier is off to ensure that the voltage V_{ph} does not go below 0. This occurs when there is no current path through the photodiode while light is incident on the detector. Figure 6-5 is a timing digram of the integrator, which includes the *Amplifier Enable* signal, as well as the control signals for S_i, S_R and S_{ph}. The inte-

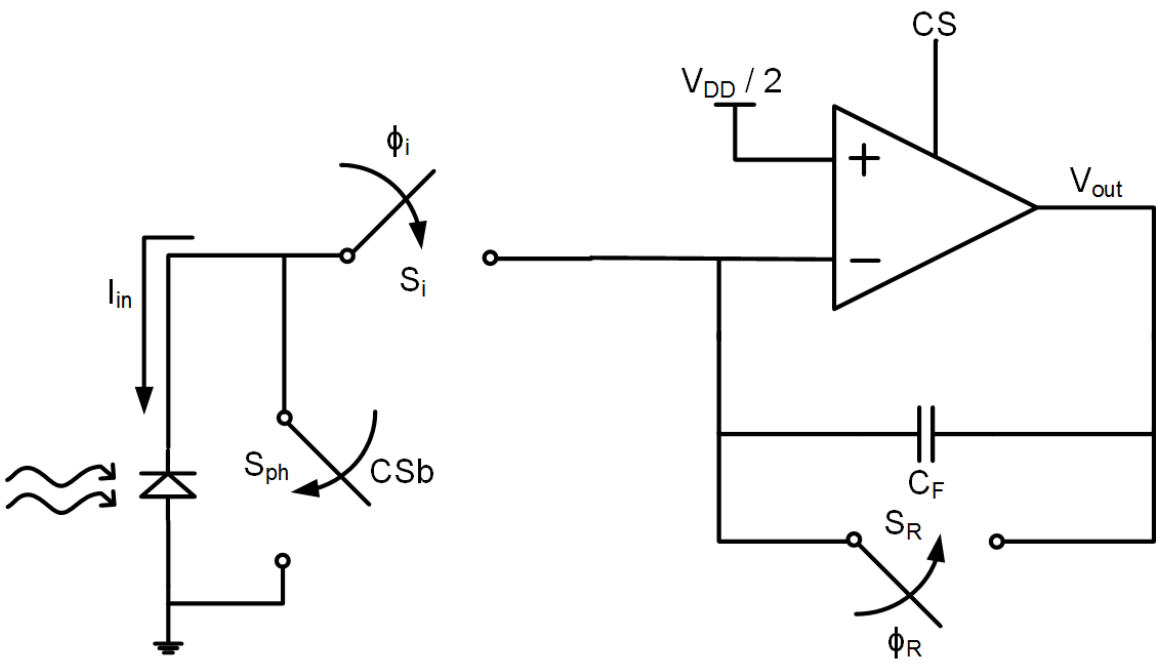

Figure 6-4: The circuit diagram of the integrator.

grating amplifier is duty cycled at a rate of 6% with control signal *Amplifier Enable*. Compared to always leaving the amplifier active, power consumption is on the order of $100\mu W$ instead of $> 1.5mW$.

6.1.4 The Dynamic Range Enhancer (DRE)

The dynamic range enhancer is an 8-bit switched capacitor current source designed to generate up to $100\mu A$ of static current. The number of bits was chosen to ensure stability. Stable operating points for the PPG SoC are defined as $120mV < V_{out} < 1.68V$. A 7-bit DAC would have current steps of $780nA$. Assuming a maximum pulsatile PPG signal of $1\mu A$, if the minimum V_{out} of the pulsatile PPG is $100mV$, adjusting the DRE current will bring the output of the maximum pulsatile PPG signal from $100mV < V_{out} < 1.1V$ to $880mV < V_{out} < 1.88V$, which is beyond the rail of the SoC, and therefore, no stable bias point can be found. Adding an eighth bit to the DRE brings the current steps down to $390nA$, which ensures stability. Figure 6-6 shows a simplified diagram of the DRE and how it fits into the PPG SoC and Figure

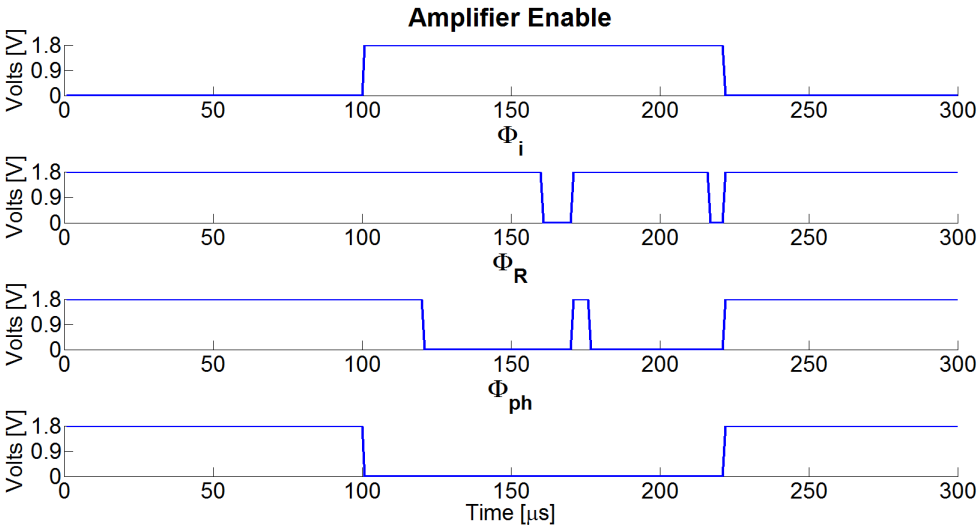

Figure 6-5: Timing diagram of the integrator.

6-7 is bit cell 'x' of the capacitor DAC (C_{DAC}).

$$I_{st} = fC\Delta V \tag{6.1}$$

where f is the clock frequency, C is the capacitance, and ΔV is the voltage drop from V_{DD} to the cathode of the photodiode.

The clock frequency is set to 6MHz and is described in section 6.1.5. The LSB capacitance for C_{DAC} is 73fF. V_{DD} is 1.8V and the voltage at the cathode of the photodiode is set by the integrating amplifier virtual ground to equal 0.9V. The *Charge* and *Dump* switches are both $\frac{25\mu m}{0.18\mu m}$ to reduce the RC time constant between the switch resistance and the capacitance of C_{DAC}. This ensures that the DAC completely charges and discharges for all values of C_{DAC}.

A switched capacitor topology is chosen compared to a current mirror because the charge noise would be divided by the square root of the number of clock cycles per integration period, which for this implementation is 240. Section 6.2 shows that the DRE current DAC is not a large contributing factor to the total system noise.

During integration, the *Reset* switch is off and the *Charge* and *Dump* switches are

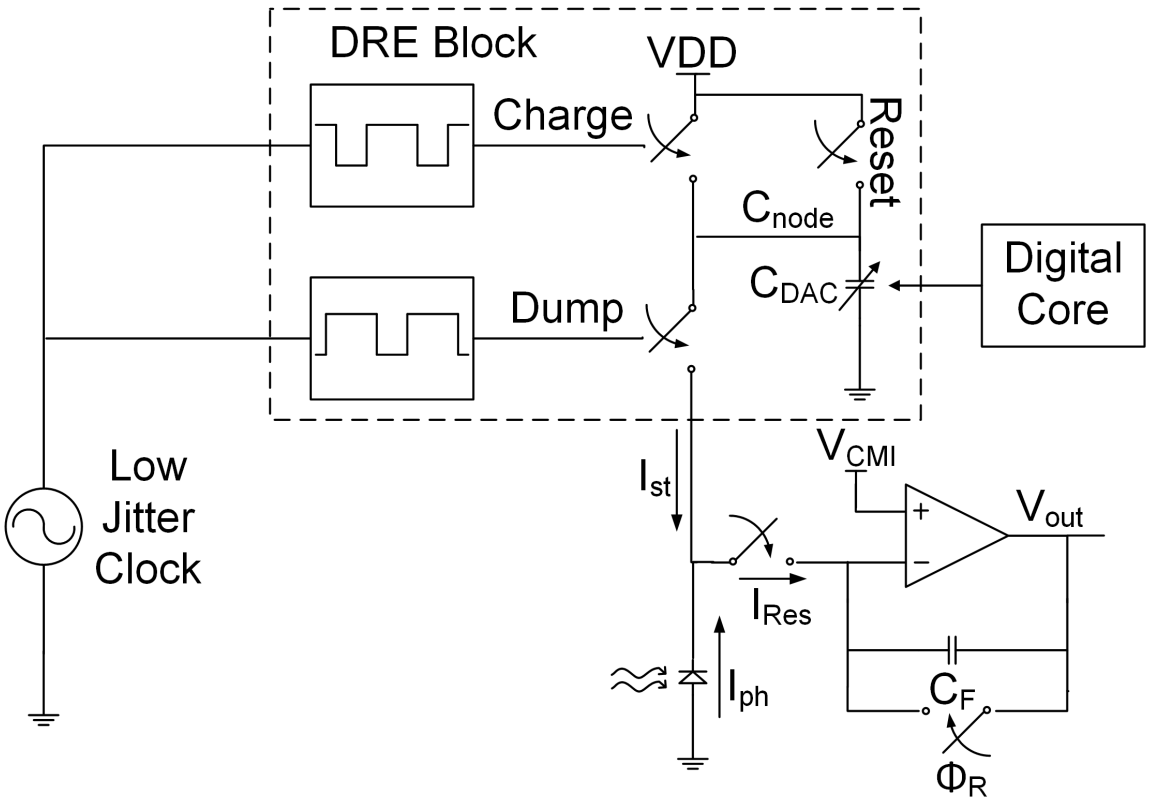

Figure 6-6: A simplified diagram of the DRE switched capacitor current DAC.

turned on with a frequency of 6MHz in a non-overlapping manner. Once integration is complete, the *Charge* and *Dump* switches are kept in the off position and the *Reset* switch is enabled to return C_{node} to 1.8V.

The switch $S_{sig,X}$ inside the bit cell is sized such that it's parasitic capacitance and switch resistance scales with C_X. The sizing of S_{sig} inside the bit cell for the MSB is $\frac{7.04\mu m}{0.18\mu m}$. Every bit cell reset switch S_{rst} is $\frac{0.22\mu m}{0.18\mu m}$.

6.1.5 The Low-Jitter Clock

The low-jitter clock is based on a design by [67]. Figure 6-8 shows the schematic of the clock. When ϕ is low, switches S_1 and S_4 are active. The current flowing through node V_2 induces a voltage drop across the resistor R. The current flowing through node V_1 charges capacitor C_1. Once the voltage at V_1 exceeds the voltage at node V_2, the comparator flips and ϕ goes high. At this point, the switches in gray are now active. The node attached to R is now V_1 and the node charging capacitor C_2 is now

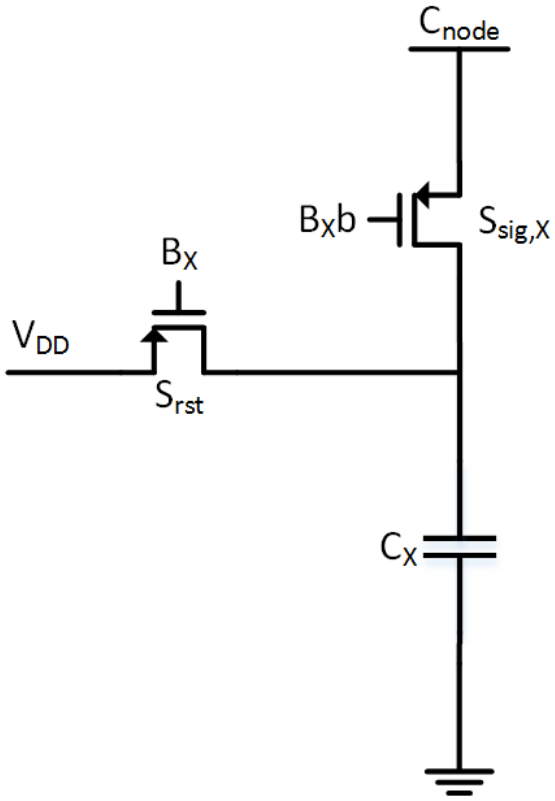

Figure 6-7: Bit cell 'x' of the capacitor DAC (C_{DAC}) in the DRE circuit.

V_2. This node switching chops the comparator offset to improve frequency stability. Charging a capacitor with a FET current source also reduces the output frequency variation due to changes in power voltage compared to a ring oscillator.

The current source I is $1\mu A$, the resistance R is nominally $169k\Omega$ and C_1 and C_2 are nominally $224fF$. Both C_1 and C_2 have 6 bits of trim, with values of $101fF$, $57fF$, $30fF$, $20fF$, $10fF$ and $5fF$, which allow for trimming the clock in steps of $30kHz$. Simulation results of the clock frequency variation with respect to several parameters are summarized in Table 6.1. The amount of tolerable jitter is 0.47%. The clock circuit is expected to consume approximately $40\mu W$.

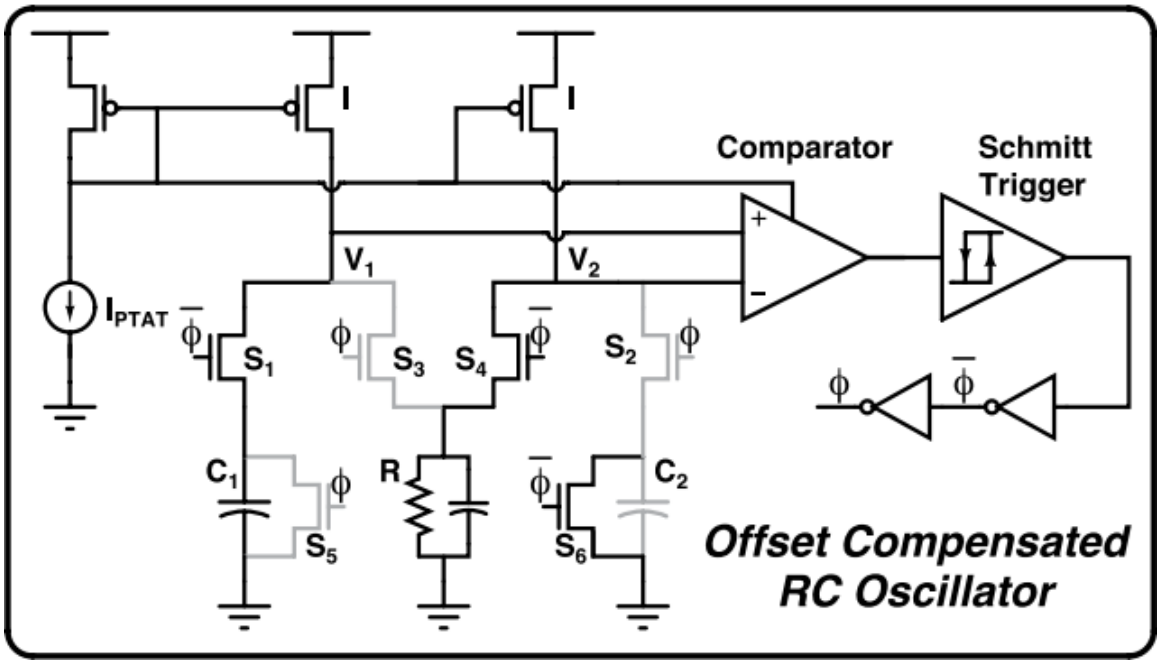

Figure 6-8: A schematic of the clock circuit. Figure from [67].

Parameter	Variation of frequency
Voltage	$0.7\%/100mV$
Temperature	$0.1\%/^oC$
Jitter	$\pm 0.2\%$

Table 6.1: Summary of Clock Simulations

6.1.6 The ADC

The ADC was designed by Marcus Yip and used with his approval [68]. It is a 9-bit successive approximation (SAR) ADC. In the PPG SoC, the ADC converts $1320\frac{samples}{sec}$ with a supply of 1.8V. Under these conditions, the ADC consumes less than $1\mu W$, which is well below the power budget of the system. The expected SNDR of the ADC is 53.6 dB and the expected effective number of bits (ENOB) of the ADC is 8.6, which is sufficient for proof-of-concept testing of the SoC.

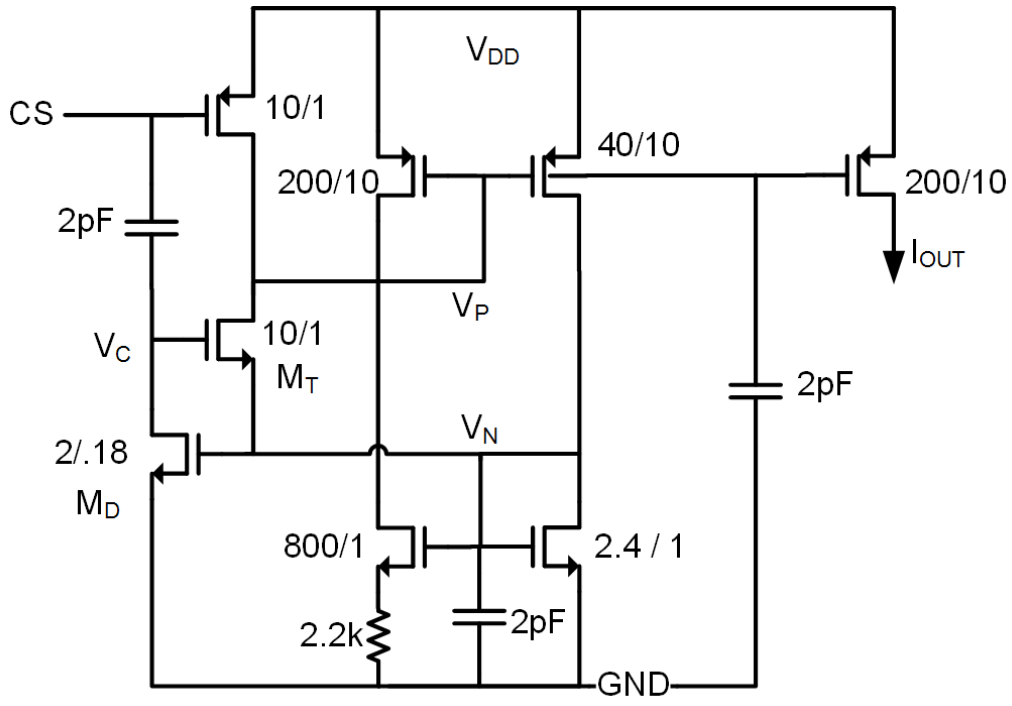

Figure 6-9: Circuit schematic of the fast startup current reference.

6.1.7 Peripheral Circuits

The Fast Startup Current Reference

The fast startup current reference is based on the work done in [69], however the circuit has been modified to allow for duty-cycling with a control signal from the digital core. Figure 6-9 shows the circuit schematic of the fast startup current reference.

The reference operates in the following manner. When CS is low, V_P is tied to V_{DD} and both V_C and V_N are tied to GND. This ensures that zero current flows through the 2.2k resistor. When CS goes from low to high, V_C is transiently pulled up, which turns on transistor M_T, simultaneously lowering the voltage on V_P and increasing it on V_N. As V_N increases, it causes transistor M_D to discharge node V_C, which turns off the startup circuit, allowing V_N and V_P to stabilize to their steady-state values. The reference is designed to supply $100\mu A$ of current and turn on in $2\mu s$, which allows for optimum duty cycling of the integrating amplifier and LED drivers.

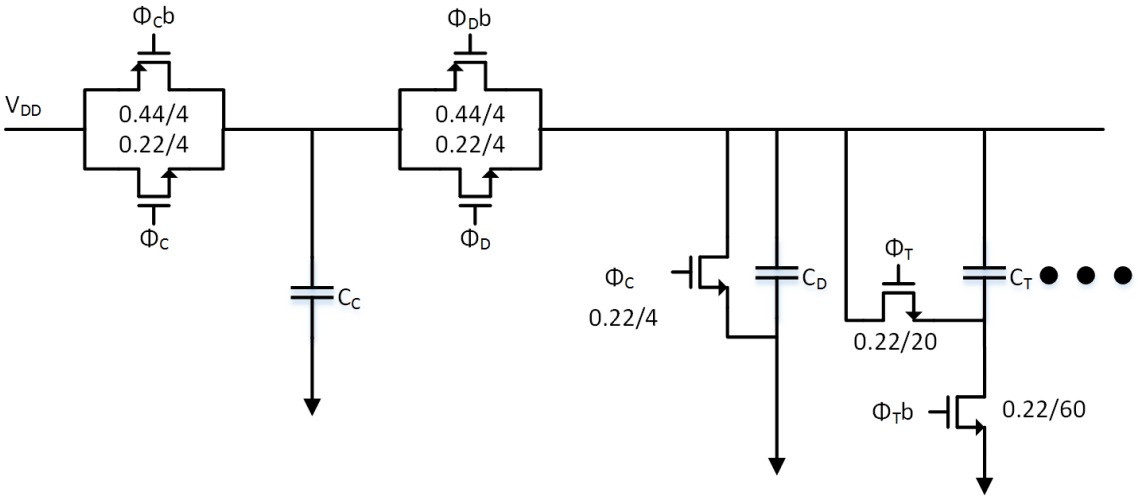

Figure 6-10: Circuit schematic of switched capacitor voltage reference.

The Switched Capacitor References

There are two types of voltage references on the PPG SoC. The first is a switched capacitor $\frac{V_{DD}}{2}$ reference, and the second is a low-dropout (LDO) regulator. The switched capacitor references are used at the positive terminals of the integrator, the inverter, and the amplifier for the LDO. This is a lower noise solution than using LDOs because the refresh rate of the capacitor voltage can be controlled, therefore switching noise from the references can be filtered out by the digital filters. The clock signal to refresh the references was a $10\mu s$ pulse which occurred every 6.06 ms (165Hz). The digital filters attenuate signals below 305Hz, which therefore removes noise due to refreshing the switched capacitor references.

Figure 6-10 shows a circuit schematic of the switched capacitor references. Seven trim bits (C_T) were used in parallel with C_D to obtain voltage steps of 4mV. C_C was 10pF for the integrating amplifier and 5pF for the inverting amplifier and LDO. Very long lengths ($60\mu m$) were used in the trim switches to reduce leakage in the references down to $2.1pA$ max, which ensured that the reference voltage at the integrator reduced by only $6mV$ over one charge cycle. Shorter lengths would require faster refresh rates for the capacitor voltage which would have been more difficult to filter out.

6.2 Noise Considerations

The analog front end was designed to meet the SNR requirements of a pulse oximeter, which is 28.5 dB for accuracy within 2% of the peripheral oxygen saturation (SpO_2) [70]. The shot noise current spectral density of a photodiode is defined as:

$$i_{n,PD}^2 = 2qI_{PD} \tag{6.2}$$

where q is the charge of an electron, (1.6×10^{-19}), and I_{PD} is the current flowing through the photodiode.

Shot noise is a Poisson process. The signal-to-noise ratio (SNR) of a Poisson process is generally defined as:

$$SNR = \frac{N}{\sqrt{N}} \tag{6.3}$$

where N in this case is the number of electrons flowing through the photodiode. Rounding 28.5 dB up to decimal 30, we can solve for the SNR of the front end in terms of N to be:

$$SNR = \frac{N}{\sqrt{N}} = 30 \tag{6.4}$$

The SNR value in equation 6.4 assumes that the static component of the PPG signal is not present. Unfortunately, the pulsatile component of the PPG signal is at minimum $\frac{1}{400}$ of the static component, so the SNR of the total PPG signal is:

$$SNR_{PPG} = \frac{N}{400 \cdot \sqrt{N}} = 30 \tag{6.5}$$

Finally, we solve for N:

$$N = (30 \cdot 400)^2 = 1.44 \times 10^8 \tag{6.6}$$

Using this number for N, we can now solve for the minimum integration time versus photodiode current:

$$T_{int} = \frac{q \cdot N}{I_{PD}} \tag{6.7}$$

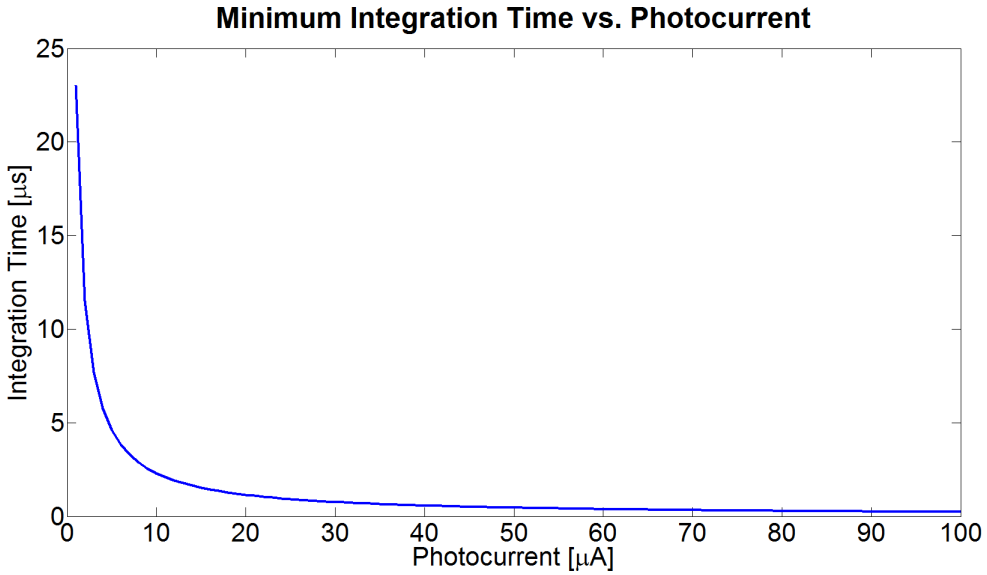

Figure 6-11: Minimum integration time of the front end versus photo-diode current, assuming that the front end noise is dominated by the photo-diode shot noise.

Figure 6-11 shows integration time versus I_{PD} from $1 - 100\mu A$.

The PPG SoC was designed to have lower noise than the photodiode shot noise across the bias points of $1\mu A - 100\mu A$. The following analysis calculates the theoretical noise from each circuit block as a noise current spectral density at the photodiode. The noise current spectral density for the LED driver is defined as:

$$i_{n,LD}^2 = [\frac{8}{3}k_B T(g_{m,bias}D^2 + g_{m,DAC}) + 2qI_{LED}]OCF^2 \tag{6.8}$$

where $g_{m,bias}$ is the summed transconductance of the devices in the current reference and bias circuits, D is the decimal value of the LED DAC, $g_{m,DAC}$ is the transconductance of the devices in the driver DAC, I_{LED} is the current through the LED, and OCF is the optical coupling factor from the LEDs to the photodiodes, estimated to be 0.004. As expected, the largest contributor to the LED driver noise is the current reference and bias circuits, as their noise contributions are multiplied by the decimal value of the DAC.

The noise current spectral density for the integrating amplifier $i_{n,Amp}^2$ is defined

as:

$$i_{n,Amp}^2 = \frac{\frac{\frac{16}{3}k_B T(g_{m,input}+g_{m,cm})}{g_{m,input}}^2}{(Z_{PD}||Z_F)^2} \tag{6.9}$$

where k_B is Boltzmann's constant, T is absolute temperature, $g_{m,input}$ is the transconductance of the input devices, and $g_{m,cm}$ is the transconductance of the current mirror devices. $(Z_{PD}||Z_F)$ is the parallel impedance of the feedback capacitance C_F, and the photodiodes, defined as:

$$(Z_{PD}||Z_F)^2 = \frac{R^2}{(C_F + C_{PD})^2 R^2 \omega^2 + 1} \tag{6.10}$$

where R is the photodiode shunt resistance and C_{PD} is the photodiode capacitance. The noise current spectral density for the switched capacitor static current generator is defined as:

$$i_{n,DRE}^2 = \frac{4k_B TC}{\Gamma} \tag{6.11}$$

where Γ is the number of clock cycles used to toggle the switched capacitor current source per integration period. Finally, the total noise current spectral density of the circuit and photodiode is:

$$i_{n,Total}^2 = i_{n,PD}^2 + i_{n,LD}^2 + i_{n,Amp}^2 + i_{n,DRE}^2 \tag{6.12}$$

Figure 6-12 shows theoretical noise contributions from each of the circuit blocks. As expected, the photodiode is the dominate noise source.

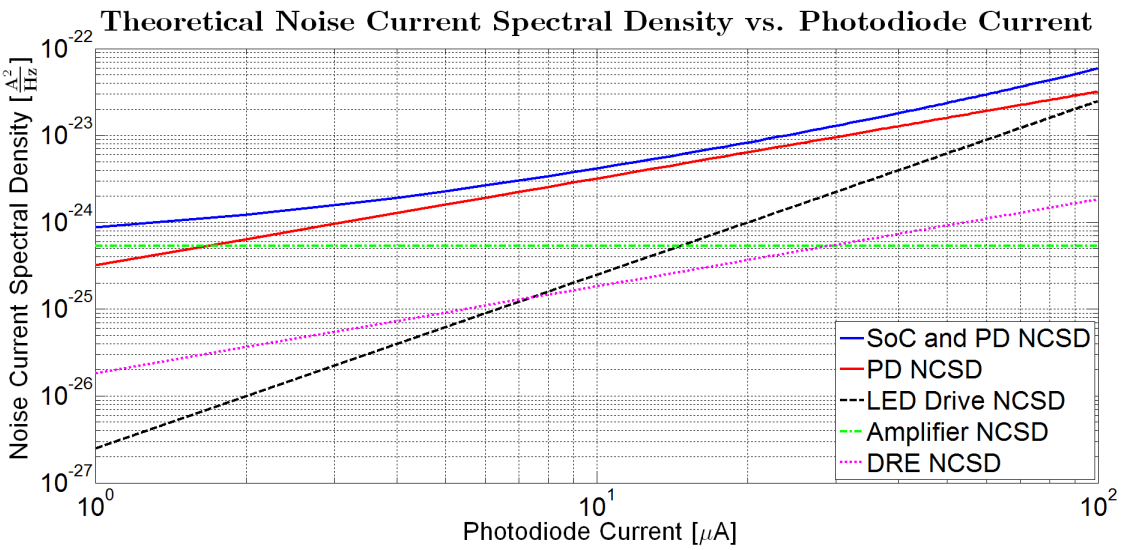

Figure 6-12: Theoretical Noise contributions from each of the circuit blocks. The photodiodes should be the dominate noise source.

6.3 The Digital Core

The digital core of the PPG AFE has three main functions. First is the digital filtering and decimation, which will be described in more detail in the next subsection. The second function of the digital core is to provide all of the control signals for the analog blocks. These controls signals duty cycle the amplifiers and current sources, as well as provide the digital codes for the dynamic range enhancement circuitry and the LED drivers. The final function of the digital core is to act as an interface to the micro-controller (MCU). The MCU communicates with the digital core via the SPI communication protocol. The digital core can send almost 100 different register values to the MCU, most notably the filtered PPG values, the raw ADC values, and different feedback values.

6.3.1 The Digital Filters

The FIR filters inside the digital core are highpass with a stopband from 0-305Hz, a transition band from 305-320Hz, and a passband from 320-330Hz. Since the sample rate is 660Hz, and the LED turn on frequency is 165Hz, the filters essentially form a passband from 320-340Hz around the second PPG image. The filters were designed

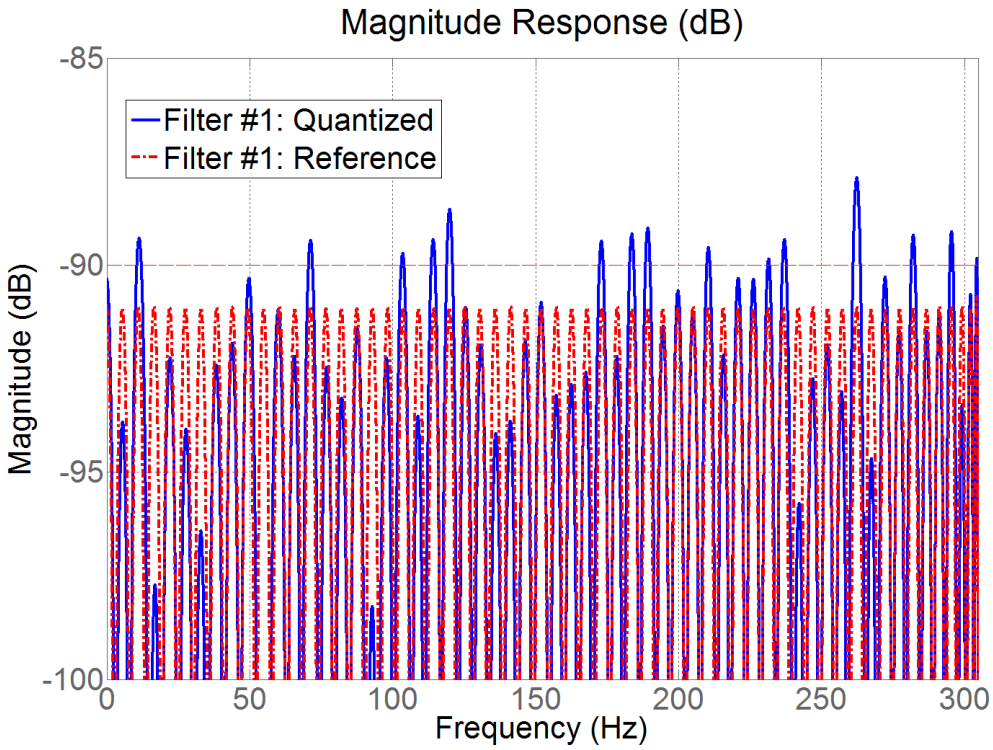

Figure 6-13: Stopband of the reference (red) and quantized (blue) filters.

using MATLAB's filter design tool, which also generated the FIR Verilog code for the digital core [71] [72]. Each filter has 125 taps, which was limited by the size of the transition band.

The stopband attenuation of the filters was designed for 90dB. After quantization of the accumulator and multiplier, the stopband attenuation reduced to 87dB, sufficient to attenuate full swing interferers below the noise floor. Figure 6-13 shows the stopband magnitude response of the reference and quantized filters. The passband response, shown in Figure 6-14 was defined as having 0.1dB ripple from 325-330Hz, and a -3dB point at 320Hz.

The filters are a decimation by 4 structure, with a signed input. The input is 10 bits, and the coefficient word lengths are 16 bits. The output word length is 16 signed bits. The multiplier is 24 bits and the accumulator is 28 bits. The coefficients were scaled to prevent overflows. The physical implementation of both filters is fully serial, with a single multiplier shared by all of the taps, which reduced chip area compared

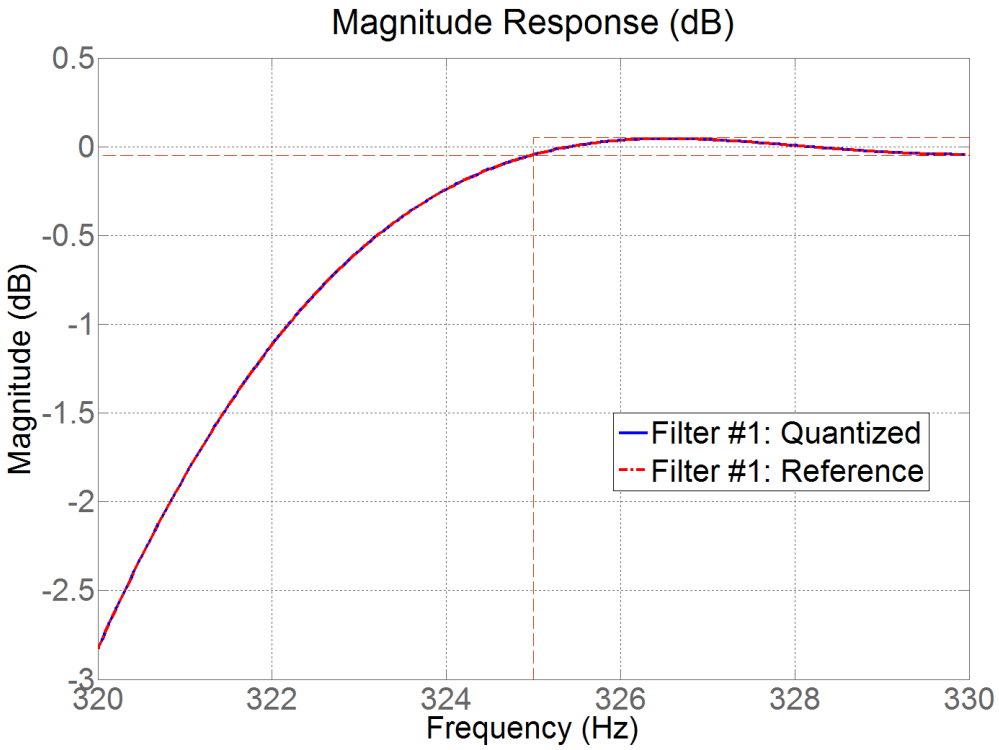

Figure 6-14: Passband of the reference (red) and quantized (blue) filters.

to a fully parallel structure. The expected power consumption is $4.8\mu W$ per filter. Figure 6-15 shows the complete response of the reference and quantized filters.

6.3.2 The Digital Feedback

The feedback algorithm for the LED drive currents and DRE current is described in Figure 6-16. The amplifier output is checked against a threshold and then the LED currents are incremented or decremented as needed. If the LED currents are above or below a set threshold and the DRE current has not been changed for at least 1.5s, then the DRE current is adjusted. Waiting 1.5s ensures stability in the feedback algorithm, as changing the DRE current before the LED drive current has settled can cause the bias point to never stabilize.

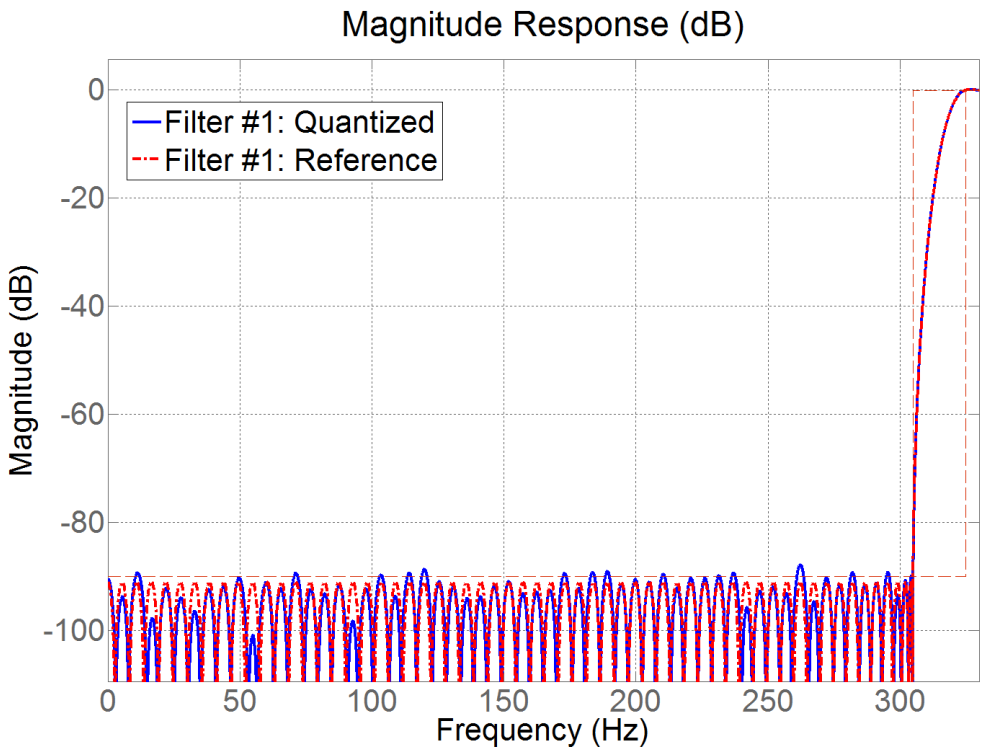

Figure 6-15: Complete response of the reference (red) and quantized (blue) filters.

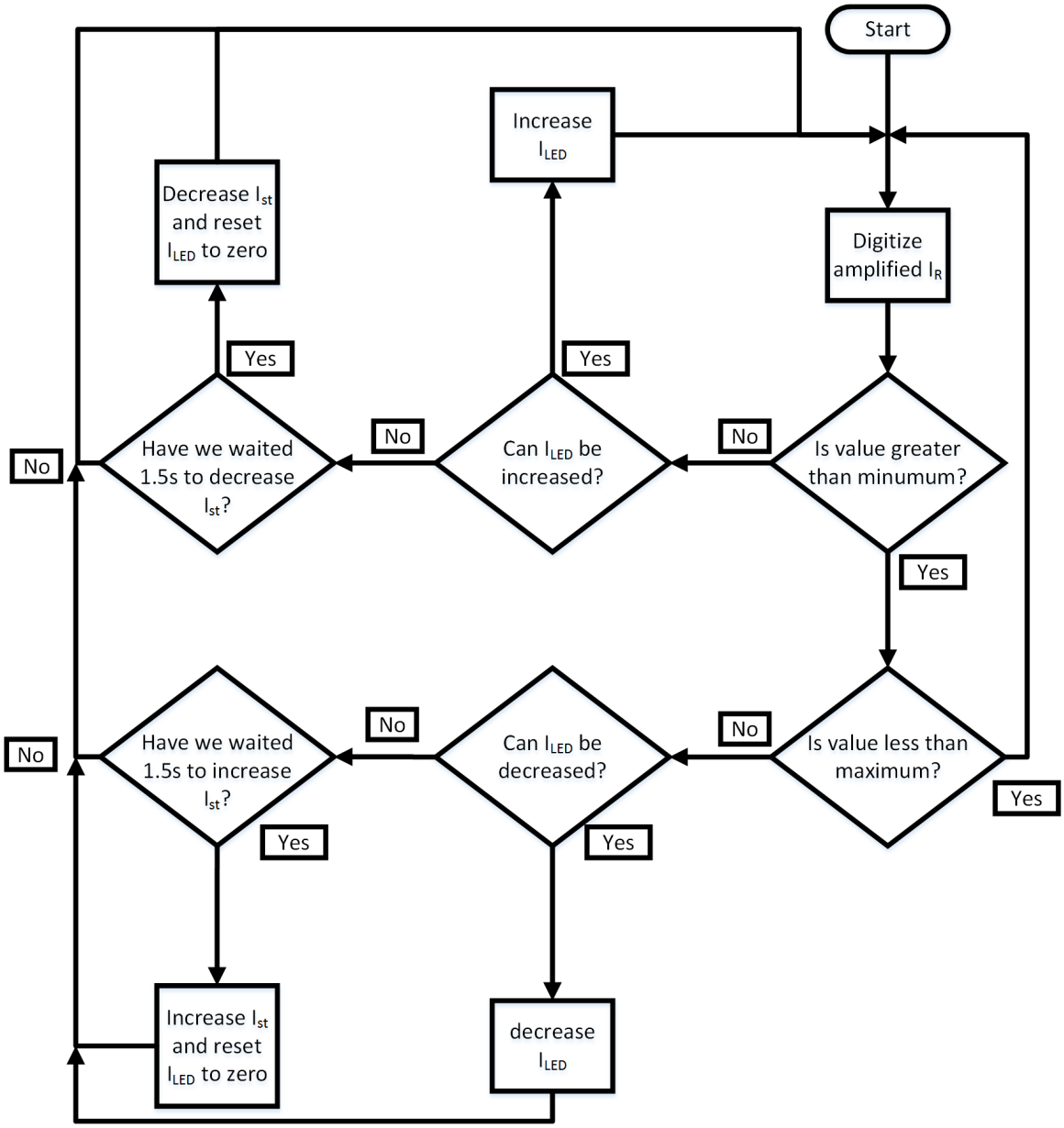

Figure 6-16: A flow diagram for the digital feedback algorithm of the PPG SoC.

6.4 Physical Layout Considerations

Physical layout considerations to improve transistor matching were taken into account. These include dummy transistors on the ends of transistor finger chains as well as common centroid topologies for the integrator differential pair and the LED drivers. Decoupling capacitors were also used wherever possible to filter noise from the supplies. In total, approximately 1nF of decoupling capacitance is implemented on chip, with about 60% used for the analog supplies, 30% for the digital supplies, and 10% for the ADC reference.

6.5 The PPG SoC Measurement Results

The following subsections summarize the measured results of the PPG SoC. Figure 6-17 is a photomicrograph of the PPG SoC.

6.5.1 $\frac{1}{f}$ Noise Removal

Modulating the PPG signal to a frequency higher than baseband allows for the removal of 1/f noise below the modulating frequency. Figure 6-18 shows clean red and IR PPG's at the output of the filters. Figure 6-19 shows spectra of the data with and without modulation and filtering. Using this technique reduces the amount of noise power in the IR PPG spectrum by $32dB$ and the red PPG spectrum by $48dB$ over the bandwidth of $0-10Hz$. The difference in the two PPGs is due to a slightly higher drive current in the red LED ($5.07mA$) compared to IR ($4.785mA$), which means that the optical coupling factor (OCF) was higher for the IR LED, increasing the noise floor.

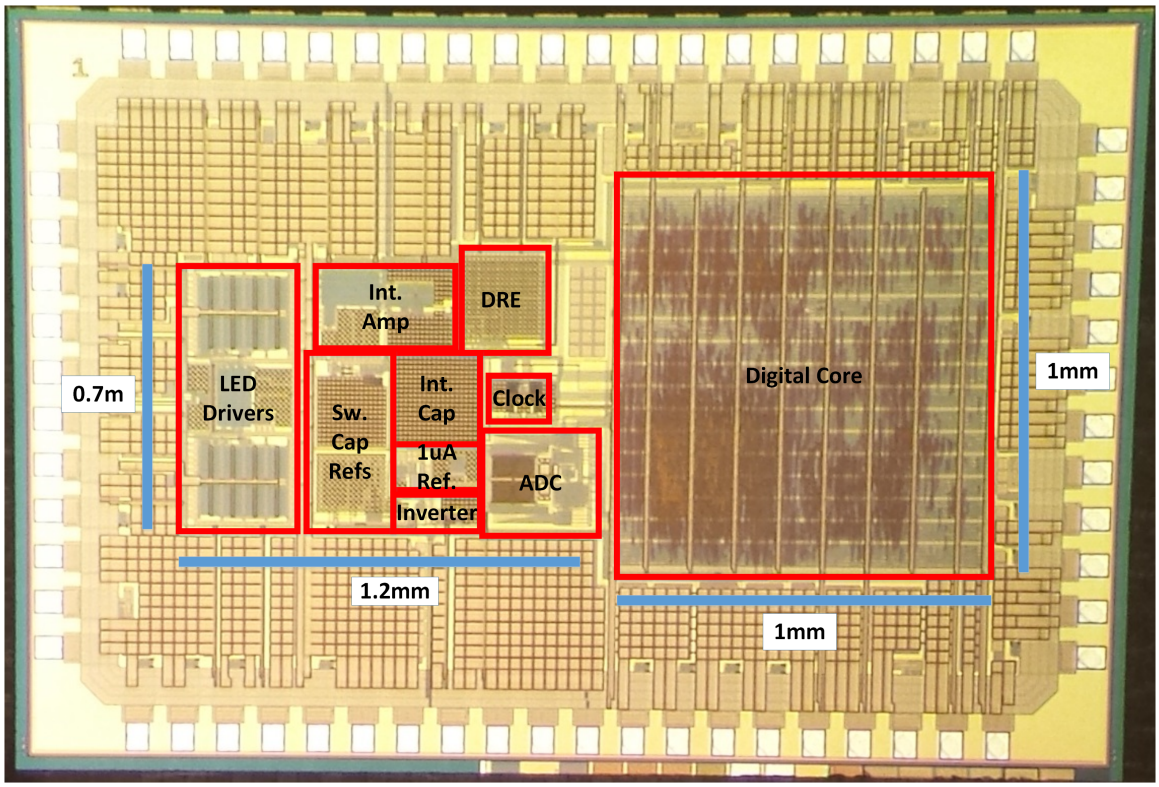

Figure 6-17: A Photomicrograph of the PPG SoC. The analog core is 1.2mm x 0.7mm and the digital core is 1mm x 1mm.

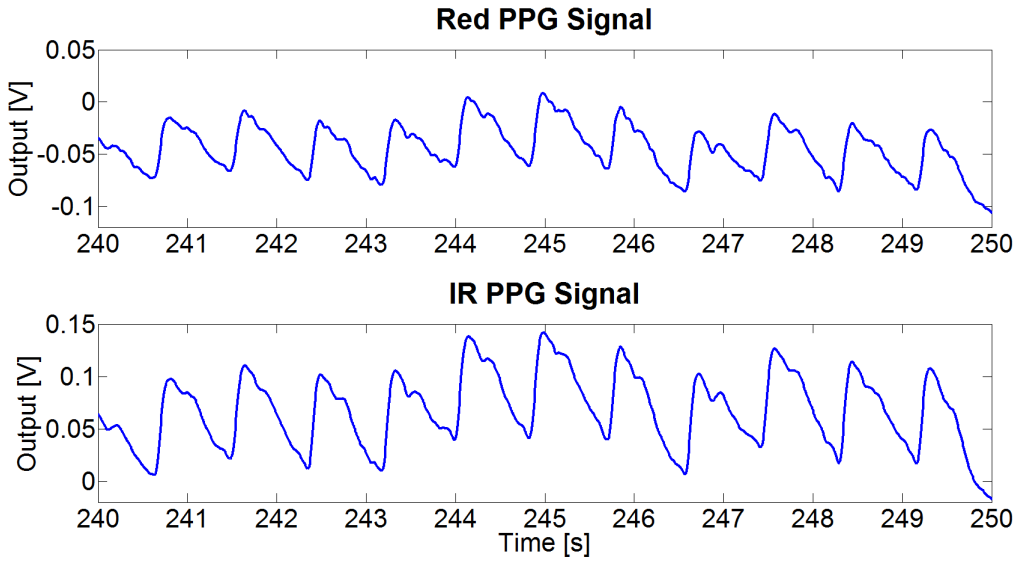

Figure 6-18: Clean PPG signals at the output of the PPG SoC without any extra post-processing.

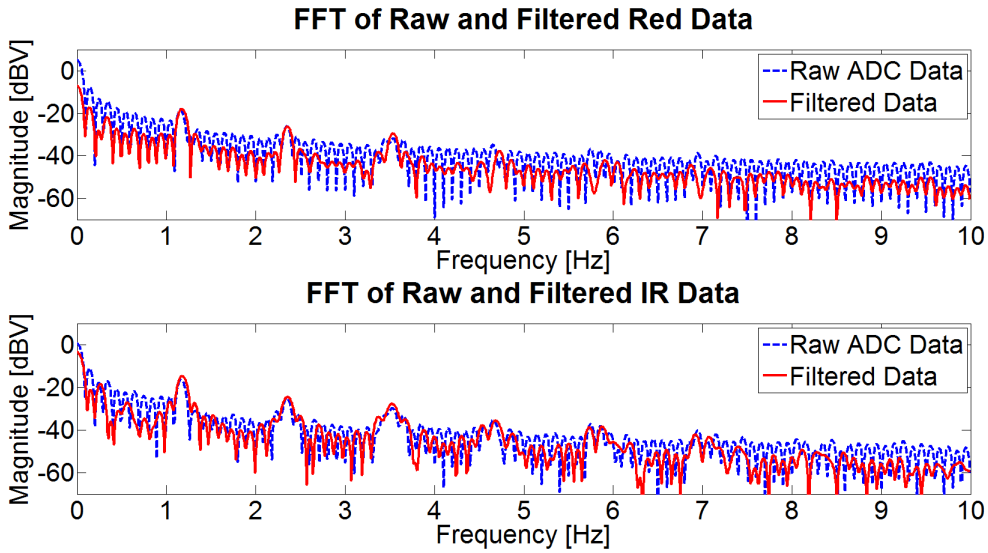

Figure 6-19: Top: The FFT of a red PPG with (red) and without (blue) modulation and filtering. Bottom: The FFT of an IR PPG with (red) and without (blue) modulation and filtering.

6.5.2 Time-varying Interference Removal

Using the modulation technique also allows for removal of time-varying interferers from the signal. The top and middle plots of Figure 6-20 show PPG and ambient sampling with a large fluorescent office light interferer incident on the sensor. The bottom graph shows the clean PPG after interferer removal and demodulation. Figure 6-21 shows spectra of the PPG and ambient interferers before filtering, and after interferer removal and demodulation.

The time varying interferer in this case was primarily a $120Hz$ fluorescent office light, however a $60Hz$ interferer is also present. Office lighting has significant power beyond the fundamental frequency. Many of the higher harmonics are visible in Figure 6-21. In this plot, the largest interferer occurs at $120Hz$ and is attenuated from $-3dB$ to below the noise floor of $-70dB$.

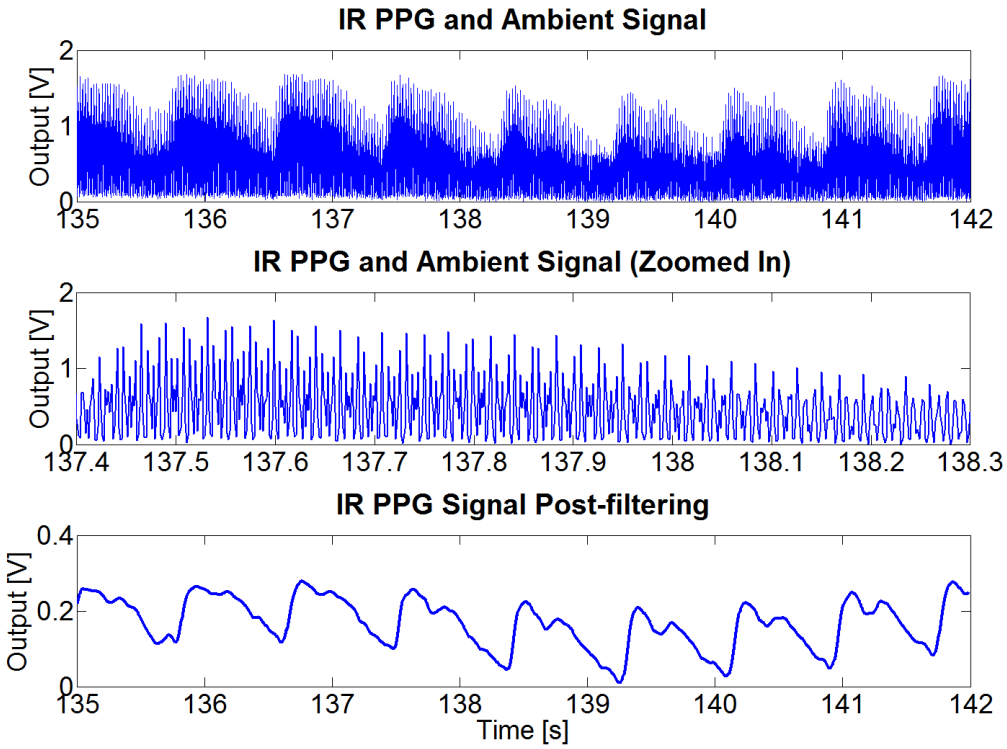

Figure 6-20: Top: PPG and ambient samples with a large $120Hz$ fluorescent office light interferer. Middle: A zoomed in plot of the top graph. Bottom: The clean PPG signal after interference removal and demodulation.

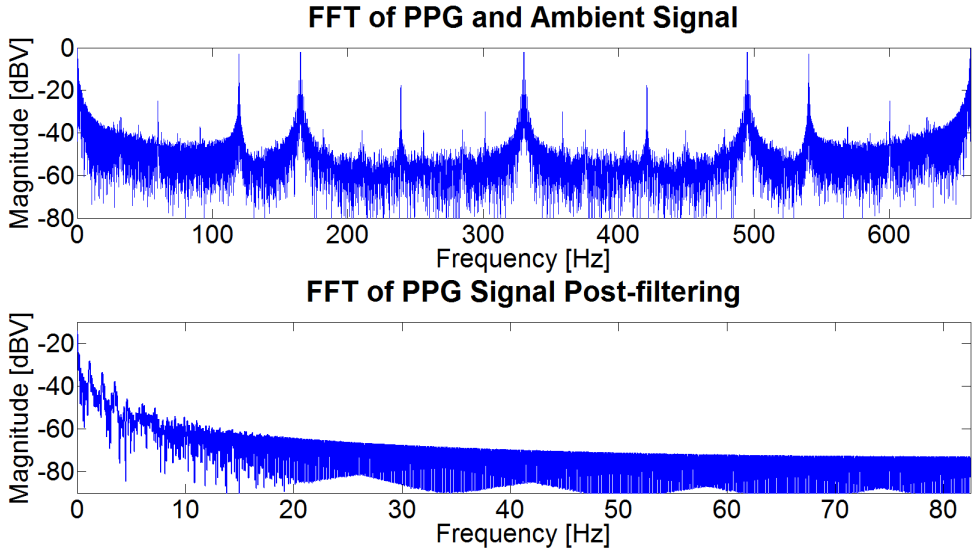

Figure 6-21: Top: The FFT of PPG and ambient samples with a large fluorescent light interferer with a fundamental frequency of $120Hz$. Bottom: The FFT of the PPG signal after interference removal and demodulation. The interferers have been attenuated by over $67dB$ to below the noise floor.

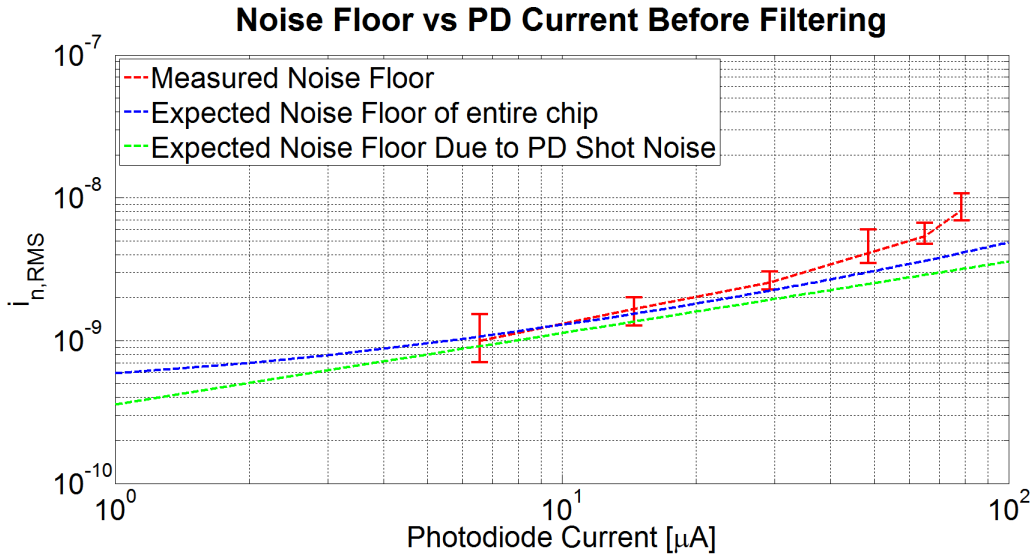

Figure 6-22: Measured circuit noise floor (red), expected circuit noise floor (blue) and theoretical photodiode shot noise (green) before filtering.

6.5.3 DRE Bias Points and Noise Measurements

Figure 6-22 shows the measured circuit noise floor (red), expected circuit noise floor (blue), and theoretical noise contribution from the photodiodes (green) across different DRE bias points before filtering. A lot of the increase in noise for higher photodiode bias currents is due to noise from the LED driver, which becomes a larger source of noise as the LED drive current increases, as shown in figure 6-12. This is due to the fact that the OCF of the system was approximately 75% higher than originally expected. Additionally, the bias current reference was sourcing $140\mu A$ instead of $100\mu A$, which increased the g_m of the bias devices and the noise current of the LED driver.

Figure 6-23 shows the measured circuit noise floor (red), expected circuit noise floor (blue), and theoretical noise contribution from the photodiodes (green) across different DRE bias points after filtering. Once again, the measured noise is approximately 3dB higher than the expected noise. The increase in noise floor at high bias currents is due to the LED driver.

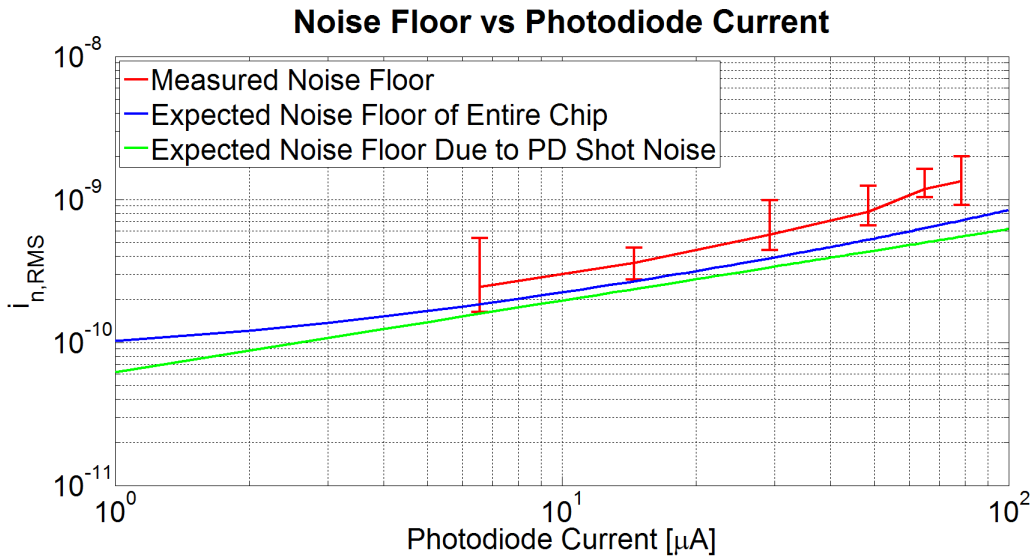

Figure 6-23: Measured circuit noise floor (red), expected circuit noise floor (blue) and theoretical photodiode shot noise (green) after filtering.

6.5.4 The Clock

Clock jitter directly effects the integration time, as τ_{int} is equal to 240 clock cycles. If the integration time was Gaussian distributed and varied by up to 0.47%, then the noise at the output of the integrator would be $2mV_{RMS}$ which is the approximate noise floor of the chip.

Figure 6-24 shows the clock signal averaged over 1000 spectra. The operating frequency was 6.024MHz, and a 20kHz BW has 40dB attenuation from the carrier frequency, indicating a jitter of 0.3%, which is acceptable for the chip. The operating frequency gives a sample rate of $165.68\frac{samples}{sec}$, which is 0.4% higher than expected ($165\frac{samples}{sec}$).

6.5.5 Power Measurements

Power dissipation for the different blocks of the chip are summarized in Table 6.2. Overall chip power consumption was $11\mu W$ higher than expected. This is mostly due to the $100\mu A$ fast startup current references, which measured $143\mu A$, and were used to power the LED driver bias and integrating amplifier. The cause of the current increase was due to the $2.2k\Omega$ resistors, which were not laid out with a standard

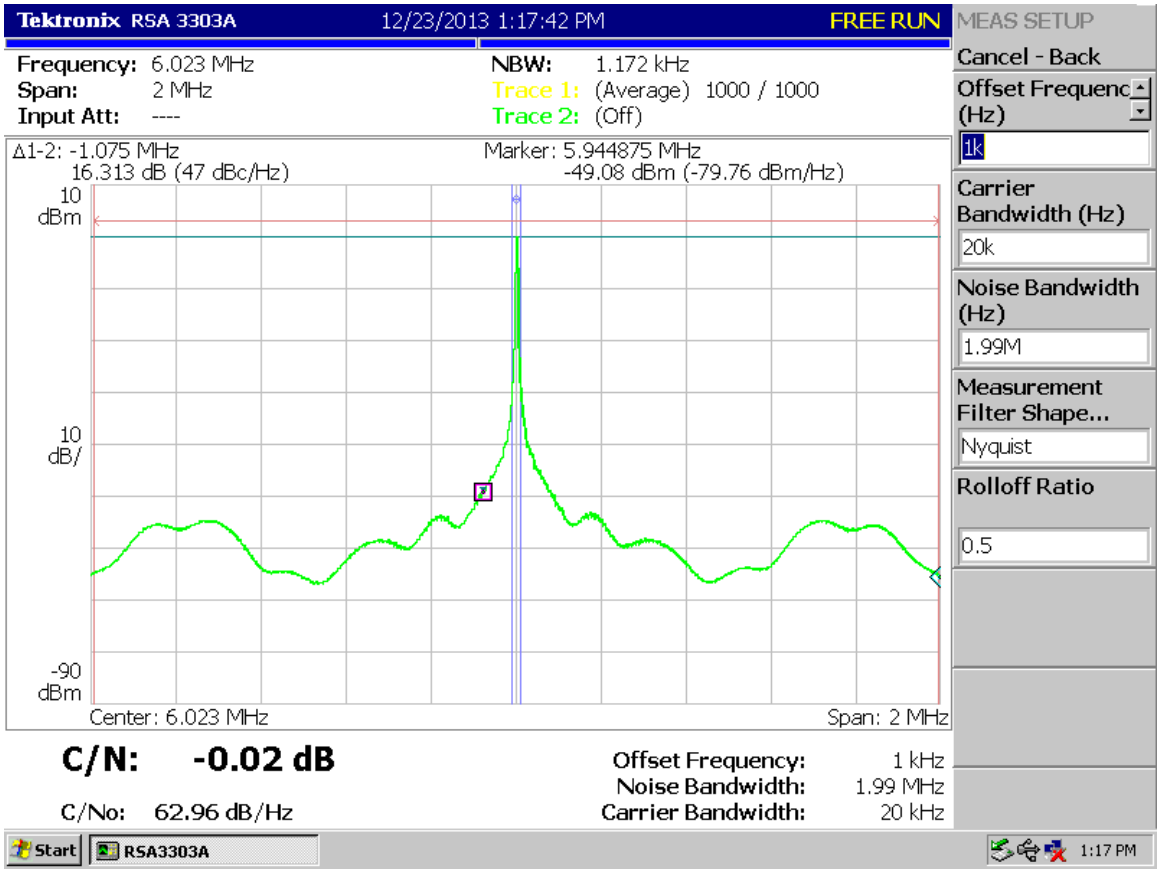

Figure 6-24: 1000 averaged spectra of the clock signal. In a 20kHz bandwidth, there is 40dB of attenuation from the carrier, implying that the jitter is approximately 0.3% of the clock frequency. The carrier frequency was 6.024MHz, which is 0.4% higher than expected (6MHz).

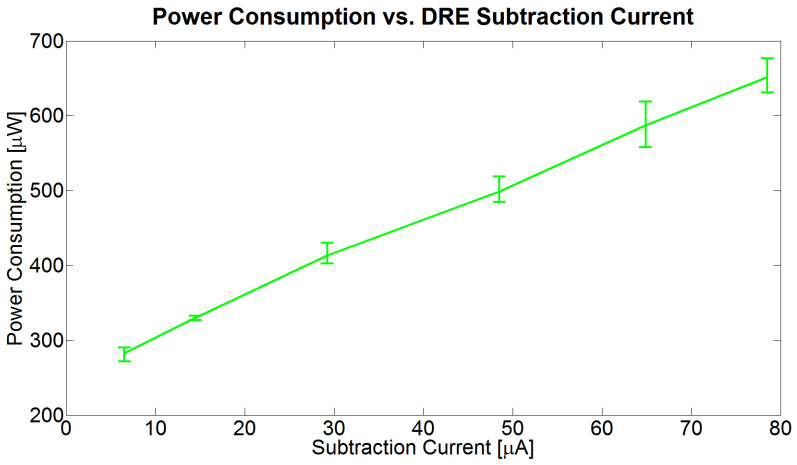

Figure 6-25: Chip power consumption over photodiode bias current.

width, and therefore most likely had a lower resistance than expected. The clock power consumption was lower due to a combination of the $1\mu A$ reference current source measuring $800nA$, and most likely the load capacitances being significantly lower than the worst case of 100fF from simulation.

Figure 6-25 shows chip power consumption for different photodiode bias currents.

Circuit Block	**Expected Power** $[\mu\mathbf{W}]$	**Measured Power** $[\mu\mathbf{W}]$
Integrating Amplifier	100	117
LED Driver Bias	9.2	21.6
Inverting Amplifier	9	9
6MHz Clock	40	20
Misc.	2	2
Digital Core	45	47
LED Drive Power	120-1,125	120-1,125
Circuits	205.2	216.6
Circuits + LED Drive	325.2-1330.2	336.6-1544.8

Table 6.2: Summary of PPG SoC Power Consumption

For this test, there were zero ambient interferers, and therefore the increased bias current was entirely due to increasing the LED drive currents. Assuming a constant optical coupling factor, the LED drivers and DRE subtraction current appear quite linear.

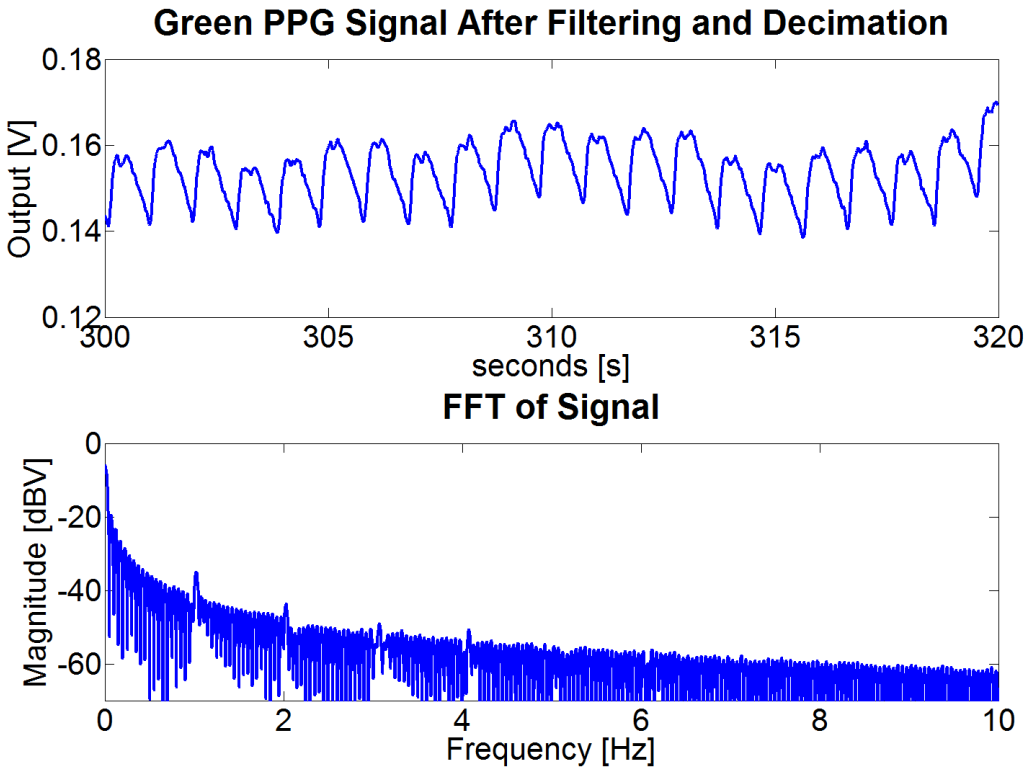

Figure 6-26: Top: A green PPG after filtering and decimation and Bottom: it's resulting spectrum.

6.5.6 Measurements with Other Optical Wavelengths

Figure 6-26 shows a PPG taken with a green LED and it's resulting spectrum. Although not as relevant at the finger, green PPGs typically have a very good SNR at nearly every place on the body, whereas red and IR need well perfused regions to be discernible [73]. The pulsatile portion of the PPG peaks with LED wavelengths between $520nm - 595nm$, and portions of the body with low perfusion, such as the lower leg can have green PPG SNR $\geq 20\times$ red PPG SNR [73].

6.6 Summary

A low-power, dual-wave, reflectance-mode PPG SoC with static and time-varying interferer removal was introduced. Critical analog and digital circuit blocks, as well as chip operation were described in detail. A theoretical noise analysis showed that

the SoC was limited by the shot noise of the photodiode. The chip was fabricated in a $0.18\mu m$ 1P6M TSMC process with an active area of $1.84mm^2$. Measurement results showed the ability of the chip to remove $\frac{1}{f}$ noise and ambient interferers through the use of FIR filters. The noise floor was measured to be $< 2nA_{RMS}$ over bias points for a 10Hz bandwidth, and clock jitter was measured to be 0.3% of the carrier frequency. Power consumption was measured to be $336 - 1544\mu W$ with a 1.8V circuit supply and 3V LED supply. Nominal power consumption was measured as $425\mu W$ while subtracting $30\mu A$ of static current in an office light setting.

Chapter 7

Conclusions

7.1 Summary of Contributions

In summary, this work presents several contributions:

- A discrete, wearable CHF monitor at the ear, which measures reflectance-mode photoplethysmogram (PPG), and ballistocardiogram (BCG) to obtain single-site, mean blood pressure estimations from $ln(\frac{1}{PTT})$.

- A clinical test on 15 subjects which demonstrated a direct relationship between $ln(\frac{1}{PTT})$ and $\overline{CBFV}$, which was theoretically shown to be dominated by changes of blood pressure in the carotid artery.

- A method for using the BCG and PPG to account for changes in vessel radius during mean arterial blood pressure estimation from $ln(\frac{1}{PTT})$.

- A low-power method for removing static interferers from a PPG signal and increasing the dynamic range of a PPG front end without reducing the PPG bandwidth of interest.

- A low-power method for removing time-varying interferers from a PPG signal through modulation, digital filtering, and decimation.

- A system on chip (SoC) for dual-wave, reflectance-mode PPG which nominally

consumes $425\mu W$, removes up to $100\mu A$ of static interferers, and attenuates time-varying interferers by $87dB$.

7.2 Future Work

Clinically, further validation of the relationship between pulse transit time (PTT) and blood pressure (BP) is needed. This is best performed in a controlled setting where a gold standard measurement of continuous blood pressure is available, such as in a hospital on patients with arterial lines. Long test durations are necessary to determine the frequency of calibration needed for accurate blood pressure estimates. Further validation of measurements in the carotid artery are also needed, and can be completed by estimating blood pressure through the use of a tonometer.

Additional validation of the proposed improvement of the PTT-to-BP algorithms utilizing cardiac output (CO) and previous values of BP to estimate the radius change of the vessels is also required. Further analysis to understand how the fitting parameter α may transiently affect the relationship between PTT and BP may also prove insightful.

For the microcontroller (MCU), further work on reducing the PTT, PEP and SV algorithms to run on an MCU instead of MATLAB is also required. Reducing these algorithms to running on an MCU allows for sending scaler values, instead of raw data over the radio. This will save over $10mW$ of power consumption in the system compared to the current discreet implementation. Now that the PPG SoC has been designed, the radio consumes over 80% of the power of the system.

Obtaining PPG signals during times of motion is still very difficult. Altering the feedback algorithm used in the SoC to update the DRE subtraction current several times per second compared to once every 1.5s may prove useful. Other techniques such as capacitive sensing to sense the motion and filter it out using adaptive filters is another possible method to explore.

7.3 A Wearable CHF Monitor Use Model

Assuming that further clinical validation is conducted on the work presented in this thesis and in [4], a use case for the monitor which can measure heart rate (HR), stroke volume (SV), cardiac output (CO), mean blood pressure (BP), pre-ejection period (PEP), and blood oxygenation (SpO_2) from a single-site will now be presented. Depending on the type of heart failure a patient has, they may experience symptoms pertaining to some, or all of these measurements.

A potential use model for this device is as follows. A patient wears the CHF monitor throughout the day. During periods of inactivity, which can be determined by the standard deviation of the accelerometer magnitude, data can be collected by the ECG, BCG, and PPG sensors. If heart rate estimations independently calculated from all three measurements are equal, it can be determined that the data is clean, and physiological parameters can be calculated. At this time, HR, SV, CO, BP, PEP and SpO_2 data can be saved to memory, or wirelessly transmitted to a base-station such as a cell-phone, for off-line analysis.

The base-station can plot the physiological information versus time, and perform basic analyses to determine if the patient's parameters have been trending negatively. If so, the information is sent to the patient's clinician to determine if an intervention is necessary. The fusion of all of these sensors in one device gives the clinician an overall window of the patient's health, compared to just measuring one parameter, once a day, such as body weight or a cuffed blood pressure measurement.

This use case makes calculations on the data only when the subject is relatively still. The data can be averaged over long time scales, such as a minute, to improve the accuracy of the measurements. Compared to the clinical test for proof-of-concept validation discussed in this thesis, where hemodynamic maneuvers through the use of motion were required, the data may be cleaner and easier to analyze. Obtaining measurements on a beat-to-beat basis, to estimate parameters during fast transients may not be required, and in general, are very difficult to achieve.

Bibliography

[1] Farlex, "Heart Failure," http://medical-dictionary.thefreedictionary.com/heart+failure, January 2014, accessed: 2013 - 1 - 15.

[2] American Heart Association, "Warning Signs of Heart Failure," http://www.heart.org/HEARTORG/Conditions/HeartFailure/WarningSignsforHeartFailure/Warning-Signs-for-Heart-Failure_UCM_002045_Article.jsp, January 2014, accessed: 2013 - 1 - 15.

[3] A. Go, D. Mozaffarian, V. Roger, E. Benjamin, J. Berry, M. Blaha, E. Ford, C. Fox, S. Franco, H. Fullerton, C. Gillespie, S. Hailpern, J. Heit, V. Howard, M. Huffman, S. Judd, B. Kissela, S. Kittner, D. Lackland, J. Lichtman, L. Lisabeth, R. Mackey, D. Magid, G. Marcus, A. Marelli, D. Matchar, D. McGuire, E. Mohler III, C. Moy, M. Mussolino, R. Neumar, G. Nichol, D. Pandey, N. Paynter, M. Reeves, P. Sorlie, J. Stein, A. Towfighi, T. Turan, S. Virani, N. Wong, D. Woo, and M. Turner, "Heart Disease and Stroke Statistics–2014 Update: A Report From the American Heart Association," *Circulation*, December 2013.

[4] D. He, "A Wearable Heart Monitor at the Ear using Ballistocardiogram (BCG) and Electrocardiogram (ECG) with a Nanowatt ECG Heartbeat Detection Circuit," Ph.D. dissertation, MIT, 2013.

[5] WebMD, "High Blood Pressure and Hypertensive Heart Disease," http://www.webmd.com/hypertension-high-blood-pressure/guide/hypertensive-heart-disease, January 2014, accessed: 2013 - 1 - 15.

[6] A. Weissler, W. Harris, and C. Schoenfeld, "Systolic Time Intervals in Heart Failure In Man," *Circulation*, vol. 37, no. 2, pp. 149–159, 1968.

[7] American Heart Association, "Heart Failure Medications," http://www.heart.org/HEARTORG/Conditions/HeartFailure/PreventionTreatmentofHeartFailure/Heart-Failure-Medications_UCM_306342_Article.jsp, January 2014, accessed: 2013 - 1 - 15.

[8] C. Yancy and W. Abraham, "Noninvasive Hemodynamic Monitoring in Heart Failure: Utilization of Impedance Cardiography," *Congest. Heart Fail.*, vol. 9, no. 5, pp. 241–250, 2003.

[9] W. Kannel, W. Castelli, P. McNamara, P. McKee, and M. Feinleib, "Role of Blood Pressure in the Development of Congestive Heart Failure - The Framingham Study," *The New England Journal of Medicine*, vol. 287, pp. 781–787, 1972.

[10] D. He, E. Winokur, T. Heldt, and C. Sodini, "The Ear as a Location for Wearable Vital Signs Monitoring," in *Engineering in Medicine and Biology Society (EMBC), 2010 Annual International Conference of the IEEE*, Aug 2010, pp. 6389–6392.

[11] D. Guo, F. Tay, L. Xu, L. Yu, M. Nyan, F. Chong, K. Yap, and B. Xu, "A Long-term Wearable Vital Signs Monitoring System using BSN," *Digital System Design Architectures, Methods and Tools, Conference on*, pp. 825–830, 2008.

[12] I. Starr, A. Rawson, H. Schroeder, and N. Joseph, "Studies on the Estimation of Cardiac Output in Man, and of Abnormalities in Cardiac Function, from the Heart's Recoil and the Blood's Impacts; the Ballistocardiogram," *The American Journal of Physiology*, vol. 127, no. 1, pp. 1–28, 1939.

[13] R. Gubner, M. Rodstein, and H. Ungerleider, "Ballistocardiography: An Appraisal of Technic, Physiologic Princibles, and Clinical Value," *Circulation*, vol. 7, no. 2, pp. 268–286, 1953.

[14] Texas Heart Institute, "Heart Anatomy," http://www.texasheartinstitute.org/HIC/Anatomy/anatomy2.cfm, October 2013, accessed: 2013 - 10 - 15.

[15] International Electrotechnical Commission, *Medical Electrical Equipment - Part 2-27: Particular Requirements for the Basic Safety and Essential Performance of Electrocardiographic Monitoring Equipment*, 3rd ed. ICS, 2011.

[16] L. Costanzo, *Physiology*, 4th ed. Saunders Elsevier, 2010.

[17] G. Fletcher, G. Balady, E. Amsterdam, B. Chaitman, R. Eckel, J. Fleg, V. Froelicher, A. Leon, I. Pina, R. Rodney, D. Simons-Morton, M. Williams, and T. Bazzare, "AHA Scientific Statement: Excercise Standards for Testing and Training," *Circulation*, vol. 104, pp. 1694–1740, 2001.

[18] 6.522, "Quantitative Physiology Lecture Notes."

[19] N. Holter and J. Generelli, "Remote Recording of Physiological Data by Radio," *Rocky Mountain Medical Journal*, vol. 46, no. 9, pp. 747–751, 1949.

[20] MindRay, "Netguard," pdf.medicalexpo.com/pdf/mindray/netguard-brochure/70856-81733-_4.html, October 2013, accessed: 2013 - 10 - 15.

[21] V-Patch Medical Systems, "V-Patch," www.vpatchmedical.com/pages/vpms-components.php, October 2013, accessed: 2013 - 10 - 15.

[22] E. Winokur, M. Delano, and C. Sodini, "A Wearable Cardiac Monitor for Long-Term Data Acquisition and Analysis," *Biomedical Engineering, IEEE Transactions on*, vol. 60, no. 1, pp. 189–192, 2013.

[23] D. He, E. Winokur, and C. Sodini, "A Continuous, Wearable, and Wireless Heart Monitor Using Head Ballistocardiogram (BCG) and Head Electrocardiogram (ECG)," in *Engineering in Medicine and Biology Society,EMBC, 2011 Annual International Conference of the IEEE*, 2011, pp. 4729–4732.

[24] UC Davis, "Spectroscopy ChemWiki," chemwiki.ucdavis.edu/Physical_Chemistry/Kinetics/Reaction_Rates/Experimental_Determination_of_Kinetics/Spectrophotometry, October 2013, accessed: 2013 - 10 - 15.

[25] J. Reuss, "Arterial Pulsatility and the Modeling of Reflectance Pulse Oximetry," in *Engineering in Medicine and Biology Society, 2003. Proceedings of the 25th Annual International Conference of the IEEE*, vol. 3, sept. 2003, pp. 2791 – 2794 Vol.3.

[26] H. Kawagucki, N. Okui, K. Sakaguchi, and E. Okada, "Theoretical Analysis of Crosstalk Between Oxygenated and Deoxygenated Haemoglobin in Focal Brain-activation Measurements by Near-infrared Topography," *Opto-Electronics Review*, vol. 16, no. 4, pp. 404–412, 2008.

[27] J. Webster, *Design of Pulse Oximeters*. Taylor and Francis Group, 1997.

[28] B. Celli and W. MacNee, "ATS/ERS Task Force. 2004. Standards for the Diagnosis and Treatment of Patients with COPD: A Summary of the ATS/ERS Position Paper," *European Respiratory Journal*, vol. 23, no. 6, pp. 932–946, 2004.

[29] Farlax, "Acute Pulmonary Edema," http://medical-dictionary.thefreedictionary.com/Acute+pulmonary+edema, January 2014, accessed: 2013 - 1 - 24.

[30] L. Afonso, J. Pradhan, V. Veeranna, A. Niraj, and S. Jacob, "Hypertension: Risk Stratification and Patient Management in Oral Healthcare Settings," http://www.ipej.org/0904/afonso.htm, December 2013, accessed: 2013 - 12 - 15.

[31] A. Weissler, W. Harrie, and C. Schoenfeld, "Systolic Time Intervals in Heart Failure in Man," *Circulation*, vol. 37, pp. 149–159, 1968.

[32] D. He, E. Winokur, and C. Sodini, "An Ear-Worn Continuous Ballistocardiogram (BCG) Sensor for Cardiovascular Monitoring," in *Engineering in Medicine and Biology Society (EMBC), 2012 Annual International Conference of the IEEE*, 2012, pp. 5030–5033.

[33] J. Lane, L. Greenstadt, D. Shapiro, and E. Rubinstein, "Pulse Transit Time and Blood Pressure: An Intensive Analysis," *Psychophysiology*, vol. 20, no. 1, pp. 45–49, 1983. [Online]. Available: http://dx.doi.org/10.1111/j.1469-8986.1983.tb00899.x

[34] D.-K. Jung, G.-R. Kim, K.-N. Kim, B.-C. Choi, D.-J. Suh, G.-R. Jeon, and S.-Y. Ye, "Changes of Pulse Wave Velocity in Arm According to Characteristic Points of Pulse Wave," in *Convergence Information Technology, 2007. International Conference on*, 2007, pp. 821–826.

[35] Y. Zheng, C. Poon, and Y.-T. Zhang, "Investigation of Temporal Relationship Between Cardiovascular Variables for Cuffless Blood Pressure Estimation," in *Biomedical and Health Informatics (BHI), 2012 IEEE-EMBS International Conference on*, 2012, pp. 644–646.

[36] Y. Chee, J. Lee, H. Park, and I. Kim, "Baroreflex Sensitivity with Pulse Arrival Time," in *Information Technology Applications in Biomedicine, 2007. ITAB 2007. 6th International Special Topic Conference on*, 2007, pp. 67–69.

[37] Y. Liu, C. Poon, and Y.-T. Zhang, "A Hydrostatic Calibration Method for the Design of Wearable PAT-Based Blood Pressure Monitoring Devices," in *Engineering in Medicine and Biology Society, 2008. EMBS 2008. 30th Annual International Conference of the IEEE*, 2008, pp. 1308–1310.

[38] J. Muehlsteff, A. Ritz, T. Drexel, C. Eickholt, P. Carvalho, R. Couceiro, M. Kelm, and C. Meyer, "Pulse Arrival Time as Surrogate for Systolic Blood Pressure Changes During Impending Neurally Mediated Syncope," in *Engineering in Medicine and Biology Society (EMBC), 2012 Annual International Conference of the IEEE*, 2012, pp. 4283–4286.

[39] F. Cattivelli and H. Garudadri, "Noninvasive Cuffless Estimation of Blood Pressure from Pulse Arrival Time and Heart Rate with Adaptive Calibration," in *Wearable and Implantable Body Sensor Networks, 2009. BSN 2009. Sixth International Workshop on*, 2009, pp. 114–119.

[40] The Free Dictionary by Farlex, "Arterial Blood Pressure (ABP)," http://medical-dictionary.thefreedictionary.com/arterial+blood+pressure, January 2014, accessed: 2013 - 1 - 15.

[41] Wikipedia, "Blood Pressure," http://en.wikipedia.org/wiki/Blood_pressure, October 2013, accessed: 2013 - 10 - 15.

[42] Mayo Clinic Staff, "Low Blood Pressure (Hypotension)," http://www.mayoclinic.org/diseases-conditions/low-blood-pressure/basics/definition/CON-20032298, January 2014, accessed: 2013 - 1 - 15.

[43] P. Heidenreich, J. Trogdon, O. Khavjou, J. Butler, K. Dracup, M. Ezekowitza, E. Finkelstein, Y. Hong, S. Johnston, A. Khera, D. Lloyd-Jones, S. Nelson, G. Nichol, and D. Orenstein, "Forecasting the Future of Cardiovascular Disease in the United States: A Policy Statement from the American Heart Association," *Circulation*, vol. 123, pp. 933–944, 2011.

[44] American Heart Association, "Understanding Blood Pressure Readings," http://www.heart.org/HEARTORG/Conditions/HighBloodPressure/AboutHighBloodPressure/Understanding-Blood-Pressure-Readings_UCM_301764_Article.jsp, January 2014, accessed: 2013 - 1 - 15.

[45] N. Korotkoff, "On Methods of Studying Blood Pressure [in Russian]," *Bull Imperial Mil. Med. Acad.*, vol. 11, pp. 365–367, 1905.

[46] G. Terezhalmy and M. Huber, "Hypertension: Risk Stratification and Patient Management in Oral Healthcare Settings," http://www.dentalcare.com/en-US/dental-education/continuing-education/ce407/ce407.aspx?ModuleName=coursecontent&PartID=2&SectionID=4, January 2014, accessed: 2013 - 1 - 15.

[47] M. Nelson, J. Stepanek, M. Cevette, M. Covalciuc, R. Hurst, and A. Tajik, "Noninvasive Measurement of Central Vascular Pressures With Arterial Tonometry: Clinical Revival of the Pulse Pressure Waveform?" *Mayo Clinic Proceedings*, vol. 85, no. 5, pp. 460–472, 2010.

[48] K. Wesseling, B. de Wit, G. van der Hoeven, J. van Goudoever, and J. Settels, "Physiocal, Calibrating Finger Vascular Physiology for Finapres," *Homeostasis*, vol. 36.2-3, pp. 67–82, 1995.

[49] Unitron Group, "Nexfin," http://www.unitron.nl/en/medical/Nexfin, January 2014, accessed: 2013 - 1 - 24.

[50] A. Moens, "On the Speed of Propogation of the Pulse (in Dutch)," Ph.D. dissertation, Leiden, The Netherlands, 1877.

[51] D. Korteweg, "Uber die Fortpflanzungsgeschwindigkeit des Schalles in Elastischen Rohren," *Annalen der Physik*, vol. 241, no. 12, pp. 525–542, 1878.

[52] D. Hughes, C. Babbs, L. Geddes, and J. Bourland, "Measurements of Young's Modulus of Elasticity of the Canine Aorta with Ultrasound," *Ultrasonic Imaging*, vol. 1, no. 4, pp. 356–367, 1979.

[53] L. Bogert and J. van Lieshout, "Non-invasive Pulsatile Arterial Pressure and Stroke Volume Changes from the Human Finger," *Exp. Physiol.*, pp. 437–446, 2005.

[54] J. Vanfraechem, "Stroke Volume and Systolic Time Interval Adjustments During Bicycle Exercise," *J. Appl. Physiol. Respir. Environ. Exerc. Physiol.*, vol. 46, no. 3, pp. 588–592, 1979.

[55] M. Olufsen, H. Tran, and J. Ottesen, "Modeling Cerebral Blood Flow Control During Posture Change From Sitting to Standing," *Cardiovascular Engineering: An International Journal*, vol. 4, no. 1, pp. 47–58, March 2004.

[56] G. Ossard, J. Clere, M. Kerguelen, F. Melchior, and J. Seylaz, "Cerebral Blood Flow Velocity Response Induced by a 70-hPa Valsavla Manoeuvre Associated with Normo-and Hypergravity in Humans," *Eur. J. Appl. Physiol.*, vol. 72, pp. 502–508, 1996.

[57] E. Winokur, D. He, and C. Sodini, "A Wearable Vital Signs Monitor at the Ear for Continuous Heart Rate and Pulse Transit Time Measurements," in *Engineering in Medicine and Biology Society (EMBC), 2012 Annual International Conference of the IEEE*, Aug 2012, pp. 2724–2727.

[58] M. Tavakoli, "An Analog VLSI Front End for Pulse Oximetry," Ph.D. dissertation, MIT, 2006.

[59] A. Wong, K. Leung, K.-P. Pun, and Y.-T. Zhang, "A 0.5-Hz High-Pass Cutoff Dual-Loop Transimpedance Amplifier for Wearable NIR Sensing Device," *Circuits and Systems II: Express Briefs, IEEE Transactions on*, vol. 57, no. 7, pp. 531 –535, july 2010.

[60] J. Patterson and G.-Z. Yang, "Dual-Mode Additive Noise Rejection in Wearable Photoplethysmography," in *Wearable and Implantable Body Sensor Networks (BSN), 2012 Ninth International Conference on*, 2012, pp. 97–102.

[61] L. Tolbert, H. Hollis, and P. Hale Jr., "Survey of Harmonics Measurements in Electrical Distribution Systems," *IEEE IAS*, pp. 2333–2339, 1996.

[62] A. Dolara and S. Leva, "Power Quality and Harmonic Analysis of End User Devices," *Energies*, vol. 5, pp. 5453–5466, 2012.

[63] M. White, D. Lampe, I. Mack, and F. Blaha, "Characterization of Charge-Coupled Device Line and Area-Array Imaging at Low Light Levels," in *Solid-State Circuits Conference. Digest of Technical Papers. 1973 IEEE International*, vol. XVI, 1973, pp. 134–135.

[64] M. Grubb, B. Hayes-Gill, J. Crowe, D. Sharkey, N. Marlow, and N. Miles, "Towards Forehead Reflectance Photoplethysmography to Aid Delivery Room Resuscitation in Newborns," in *4th European Conference of the International Federation for Medical and Biological Engineering*, ser. IFMBE Proceedings, J. Sloten, P. Verdonck, M. Nyssen, and J. Haueisen, Eds., vol. 22, 2009, pp. 1053–1056.

[65] A. Oppenheim, R. Schafer, and J. Buck, *Discrete-Time Signal Processing (2nd ed.)*. Upper Saddle River, NJ, USA: Prentice-Hall, Inc., 1999.

[66] D. Johns and K. Martin, *Analog Integrated Circuit Design*. John Wiley and Sons Inc., 1997.

[67] A. Paidimarri, D. Griffith, A. Wang, A. Chandrakasan, and G. Burra, "A 120nW 18.5kHz RC Oscillator with Comparator Offset Cancellation for ±0.25% Temperature Stability," in *Solid-State Circuits Conference Digest of Technical Papers (ISSCC), 2013 IEEE International*, Feb 2013, pp. 184–185.

[68] M. Yip, J. Bohorquez, and A. Chandrakasan, "A 0.6V 2.9uW Mixed-Signal Front-End for ECG Monitoring," in *VLSI Circuits (VLSIC), 2012 Symposium on*, 2012, pp. 66–67.

[69] S. Mandal, S. Arfin, and R. Sarpeshkar, "Fast Startup CMOS Current References," in *Circuits and Systems, 2006. ISCAS 2006. Proceedings. 2006 IEEE International Symposium on*, 2006, pp. 4 pp.–.

[70] K. Glaros and E. Drakakis, "A Sub-mW Fully-Integrated Pulse Oximeter Front-End," *Biomedical Circuits and Systems, IEEE Transactions on*, vol. 7, no. 3, pp. 363–375, 2013.

[71] Mathworks, *Filter Design HDL Coder ^{TM} User's Guide*. Mathworks, 2012.

[72] R. Losada, *Digital Filters with MATLAB*. Mathworks, May 2008.

[73] W. Cui, L. Ostrander, and B. Lee, "In Vivo Reflectance of Blood and Tissue as a Function of Light Wavelength," *IEEE TBME*, vol. 37, no. 6, pp. 632–639, 1990.